EnPress Publisher

Thermal Science and Engineering

2021
Volume 4
Issue 1
ISSN: 2578-1782

https://systems.enpress-publisher.com/index.php/TSE

Editorial Board

Editor-in-Chief

Associate Editor

Editorial Board Member

Volume 4 Issue 1 • 2021

Thermal Science and Engineering

Editor-in-Chief

Prof. Gang Zhang

A-Star, Institute of High Performance Computing (IHPC), Singapore

EnPress Publisher

2021 | Volume 4 | Issue 1

Thermal Science and Engineering

https://systems.enpress-publisher.com/index.php/TSE

Contents

1 **Review of the calculation of the boiling heat transfer coefficient in mini-channels and micro-channels**

César-Arnaldo Cisneros-Ramírez

8 **Combined operation mode of sub-critical W-flame boiler and coal mill optimized numerical simulation**

Lun Ma, Qingyan Fang, Dengfeng Tian, Cheng Zhang, Gang Chen

19 **Wolfram Mathematica, exact solutions for heat transfer methods applied to extrusion processes**

Antonio-Jiménez Ramos, Juan Francisco-Puertas Fernández, Margarita J.-Lapido Rodríguez, Julio Rafael-Gómez Sarduy, Yulier-Jiménez Santana, Fidel-Sosa Núñez

28 **Thermodynamic stability diagram of the copper/water/amylxanthate flotation system**

Beatriz Ramírez-Serrano, Alexis Otero-Calvis, Alfredo Coello-Velázquez

34 **Thermodynamic study on lead leaching from sodium citrate**

Lina Constanza Villa, Wilmer Saldarriaga Agudelo, Néstor Ricardo Rojas

42 **Determination of overall heat transfer coefficients comparing LMTD and ε-NTU methods**

Andres Adrian Sánchez Escalona, Ever Góngora Leyva

51 **Experiment and characterization of dynamic thermal storage characteristics of porous media thermal storage system**

Ke Yan, Leming Cheng, Weiguo Zhang, Zhengzhan Shi, Kunzan Qiu

60 **Influence of Na_2CO_3 on combustion performance of civil clean coke**

Bingning Wang, Shoujun Liu, Song Yang, Xudong Yan, Liangyu Chen, Jin Li

Thermal Science and Engineering (2021) Volume 4 Issue 1
doi:10.24294/tse.v4i1.1505

REVIEW ARTICLE

Review of the calculation of the boiling heat transfer coefficient in mini-channels and micro-channels

César-Arnaldo Cisneros-Ramírez*

Instituto Superior Politécnico José Antonio Echeverría, Centro de Estudios de Tecnologías Energéticas Renovables, CETER, La Habana, Cuba. E-mail: cesar@mecanica.cujae.edu.cu

ABSTRACT

The need to dissipate high heat flux densities has led researchers and designers to employ phase change as a mechanism to achieve this goal and thereby achieve more compact heat exchanger equipment. In the present work, a study of the literature on boiling in mini-channels and microchannels was carried out. For this purpose, bibliographies dating from the 1990s to the present were consulted, which revealed the main parameters or topics that characterize this process in mini-channels and microchannels. Thus, the terms mini-channels and microchannels, forced flow boiling and flow regimes (map) are addressed. In addition, a summary of the equations for the determination of the heat transfer coefficient in two-phase regime (h_{df}) is presented.

Keywords: Boiling; Microchannels; Mini-channels; Heat Transfer Coefficient

ARTICLE INFO

Received: 5 January 2021
Accepted: 31 January 2021
Available online: 5 February 2021

1. Introduction

The need to dissipate high heat flux densities by air flow has forced designers to consider liquid cooling without phase change as an option. The other option has been to employ phase change for this purpose, i.e., the use of boiling in small diameter channels. Heat pipes, fuel cells, compact evaporators of advanced designs, among others, are equipment or devices that use channels of hydraulic diameter of the order of 1 mm. It was Tuckerman and Pease[1] who demonstrated experimentally that a heat flux density (qp) of 1300 W/cm^2 can be dissipated while maintaining a temperature difference of less than 70 °C.

That is why boiling in mini-channels and microchannels has great expectations to obtain an effective heat dissipation, mainly in small equipment[2], hence this line of research has taken interest mainly when it is necessary to dissipate high heat flux densities in electronic equipment among other uses[3,4].

Shah[5] defined the compact exchanger as having an area to volume ratio equal to or greater than 700 m^2/m^3. Many of the electronic circuit fabrication techniques are used in the fabrication of compact exchangers. Mini-channels and microchannels constitute a new technology in the dissipation of large energy densities through small areas. They are an alternative for the replacement of conventional finned exchangers used mainly in the automotive, air conditioning and refrigeration industries, among others. A surface of mini-channels and microchannels is usually formed by several of these elements in parallel[6]. The cooling medium flows through these channels in order to extract the heat from the energy

source, having as a characteristic that the flow is laminar. In addition, in such a surface, high values of heat transfer coefficient, high area/volume ratio, small mass and volume are obtained and small amount of the cooling medium or cooling agent is needed.

In a heat exchanger consisting of mini-channels and microchannels, heat transfer is improved in two ways: first, the small dimensions of the ducts increase the heat transfer coefficient and second, the flat orientation of the ducts reduces the resistance on the air flow, which leads to a higher flow or a decrease in fan power. These attributes make minichannel and microchannel surfaces suitable media for cooling equipment[7].

Compared to a conventional exchanger, the main advantage of a mini-exchanger or a micro-exchanger is its high area/volume ratio, which results in a high overall heat transfer coefficient per unit volume that can be greater than 100 MW/m^{3}K; higher by 1 or 2 orders of magnitude than that of a conventional exchanger[8].

From the literature reviewed, it can be said that the theory for single-phase flow is applicable for conventional channels as well as for mini-channels and microchannels[9]. However, the theory for two-phase flow in conventional channels is not appropriate for mini-channels and microchannels[10].

The objective of this work is to review the literature on the characteristics of heat transfer during boiling in mini-channels and microchannels. For this purpose, the terms mini-channels and microchannels, forced flow boiling and flow regimes (map), among others, are discussed. In addition, a summary of the equations for the determination of the heat transfer coefficient in two-phase regime (h_{df}) that have been obtained and published by different authors is presented.

2. Methods and materials

2.1 Minichannel and microchannel

When are we in the presence of a mini-channel or microchannel? The terms mini-channel and micro-channel are used in the literature without any universal criteria, although many works have been carried out in an attempt to find a general criterion for these terms. Some researchers define the same transition criterion, between macrochannel and minichannel/microchannel, for both single-phase and two-phase flow in channels, while others define the criterion independently for single-phase and two-phase flow.

Mehendale[11] used the following classification to define channels:

1 μm ≤ D_h ≤ 100 μm: Microchannel

100 μm ≤ D_h ≤ 1 mm: Minichannel

1 mm ≤ D_h ≤ 6 mm: compact channel

6 mm < D_h: conventional channel

Kandlikar and Balasubramanian[12] use a classification based on the mean path of molecules in single-phase flow, surface tension effects and two-phase flow structure.

Conventional channel: $D_h \geq 3$ mm

Mini-trunking: 200 μm ≤ D_h < 3 mm

Microchannel:10 μm ≤ D_h < 200 μm

Nanochannel or molecular: $D_h \leq 0.1$ μm

Based on the observation that as the channel dimensions become smaller, the surface tension becomes important and on the other hand that the effect of gravity loses its effect, Kew and Cornwell[13] proposed as a criterion to define macrochannels, minichannels and microchannels, the confinement number (Co), given by:

$$Co = \frac{\left[\frac{\sigma}{g(\rho_l - \rho_g)}\right]^{0.5}}{D} \quad (1)$$

Where σ, ρ_l, ρ_v, g and D are liquid surface tension, liquid density, vapor density, gravity and channel diameter respectively.

This number is the ratio between the size of the bubble at the time of its detachment from the surface and the diameter of the duct. This same criterion has been used by Thome *et al.*[14] and Barber[15]. Under this criterion, a channel whose confinement number is greater than 0.5 can be classified as a mini/microchannel and the opposite would be a conventional channel.

Harirchian and Garimella[16] suggested the confining convective number as a criterion to define the macrochannel and the mini-channel or macrochannel,

which is given by the Bond number (Bo) and the Reynolds number (Re) whose expression is:

$$Bo^{0.5} \cdot \mathrm{Re} = 160 \tag{2}$$

The Bond number expresses the ratio between the buoyancy force and the force due to tension.

$$Bo = \frac{D_h}{\sqrt{\frac{\sigma}{g(\rho_l - \rho_v)}}} \tag{3}$$

The Reynolds number expresses the ratio between the dynamic force and the viscous force.

$$\mathrm{Re} = \frac{uD\rho}{\mu} \tag{4}$$

For a value less than 160 the channel is catalogued as a mini-channel or micro-channel and above this value it is a macro-channel. With this criterion the authors tried to take into account the effects of mass flux density and viscosity on the confinement of flow in mini-channels and microchannels together with surface tension, gravity and density.

Brauner [17] in his analysis proposed the Eötvös number (Eo) as a criterion to consider or not the influence of surface tension and gravity. The discriminant value is Eo < $(2\pi)^2$.

$$E\ddot{o} = \frac{D^2 g(\rho_l - \rho_v)}{\sigma} \tag{5}$$

On the other hand, Lee[18], considering the relationship between the drag force on the bubble and the force due to surface tension, proposes the following transition criterion:

$$D_{trans} = 17.8\left(\frac{\sigma\rho_l - 3\mu_l G}{G^2}\right) \tag{6}$$

From the above it can be said that there is no unity of criteria for the definition of mini-channel and micro-channel.

2.2 Ebullition in forced flow

In forced flow boiling it is common to consider that heat is transferred by two mechanisms: forced convection and nucleated boiling. In forced convection heat is transferred in the same way as in convection without phase change, where the heat transferred increases with increasing mass flux density (G). This mechanism is modeled with equations similar to those of convection without phase change including a fluid flow enhancement factor[13,19]. In nucleated boiling, heat is transferred by bubbles arising on the heating surface. These bubbles grow and eventually separate from the heating surface. This mechanism is similar to that of large volume boiling and is modeled with the equations of the latter. Here the heat transfer coefficient increases with increasing heat flux density and is independent of vapor quality and mass flow rate[20,21].

Heat transfer in the nucleated boiling regime is characterized by the formation of bubbles, which is influenced by the density of nucleation centers, the diameter of bubble detachment and the frequency of bubble formation.

The nucleation center density (Na) is the number of cavities or sites in which bubbles are generated per unit area of the channel and gives a measure of the energy transferred with the bubble. This nucleation center density depends on the heat flux density (q''_w)[22,23], vapor velocity[24], cavity size[25] and fluid type.

The expression obtained by Kuo[26] is based primarily on the heat flux density

$$Na = 0.29 q''^{1.4}_W \tag{7}$$

The boiling cycle is the process of liquid heating, bubble formation, bubble growth and bubble release. The number of bubbles formed per unit time or bubble formation frequency (f) and bubble detachment diameter (Ddb) are factors that have great influence on heat transfer[9]. During forced flow boiling the bubble formation frequency depends on the heat flux density, mass flux density, fluid type, size and nature of the nucleation center (cavity) and the bubble release diameter. In general, the bubble detachment frequency is evaluated by an expression of the form[26-28]:

$$f^n D_{db} = f(g, \rho_l, \rho_v, Ja) \tag{8}$$

$$f^n D_{db} = \mathrm{cte} \tag{9}$$

Where *Ja* is the Jakov criterion which expresses the ratio between the sensible heat required to heat a mass of liquid to its saturation temperature (T_{sat}) and

the latent heat h_{lv} to evaporate the same mass of liquid.

$$Ja = \frac{c_p(T - T_{sat})}{h_{lv}} \tag{10}$$

The value obtained by Kuo[26], for an average absolute error of 17%, was:

$$fD_{db} = 5.65 \times 10^{-3} \frac{m}{s} \tag{11}$$

In the literature[29], the authors proposed the dimensionless nucleation frequency as a function of the dimensionless temperature difference through the expression:

$$f^* = 0.0013 \exp\left(3 \cdot 10^{-5} \varphi\right) \tag{12}$$

Where frequency and dimensionless temperature were defined as:

$$f^* = \frac{fW^2 \rho_l}{\mu_l} \tag{13}$$

and

$$\varphi = \frac{(T_s - T_\infty) W k_l \rho_l}{\mu_l \sigma} \tag{14}$$

Where W, μ_l, k_l, T_s, T_∞ are the width of the channel, the dynamic viscosity and thermal conductivity of the liquid, the temperature of the surface where the liquid boils and the temperature of the liquid.

Applying a dimensional analysis, in the literature[29], they obtained a relationship between the size at which the bubble detaches and the Reynolds criterion, which expresses the exponential decrease in the size of the bubble at the time of detachment (V_{db}) as the Reynolds criterion (Re) increases, that is:

$$\frac{V_{db}}{H^3} = 2 \cdot 10^4 \exp\left(-5 \cdot \mathrm{Re}^{0.25}\right) \tag{15}$$

Where H is the characteristic dimension of the channel.

2.3 Map of flow regimes

The determination of the different flow regimes has been studied by several researchers[16,30,31], since, once the regime is known, the development of models for the calculation of both the heat transfer coefficient and the pressure drop is facilitated.

In mini-channels and microchannels the flow regime depends on the interaction between the forces due to surface tension and inertia. Surface tension is dominant in the bubble and bullet flow regimes; and inertia is dominant in the annular and eddy flow regimes. **Figure 1** shows a representation of each of these flow types.

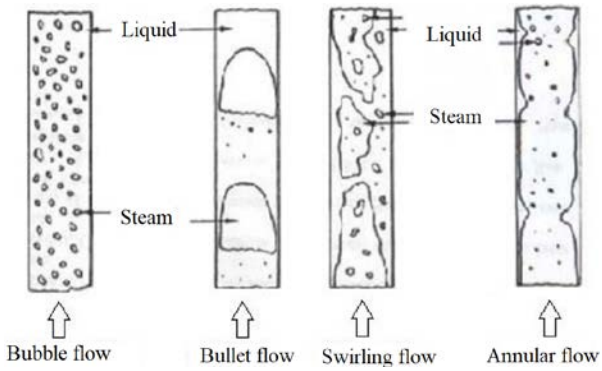

Figure 1. Flow regimes.

The flow regime map proposed by Harirchian and Garimella[16,31] proposes that for values of $Bo0.5\mathrm{Re} < 160$ vapor confinement is observed in both the bullet and swirl/annular flow regimes, while for $Bo0.5\mathrm{Re} > 160$ no confinement is observed. For low heat flux density with $Bl < 0.017$ ($Bo0.4\mathrm{Re}$-0.3) and $Bo0.5\mathrm{Re} < 160$ bullet flow is observed and with $Bo0.5\mathrm{Re} > 160$ bubble flow is observed. For high heat flux density i.e., for $Bl > 0.017$ ($Bo0.4\mathrm{Re}$-0.3) the bubbles coalesce and give rise to swirling/annular flow. Bl and Bo are the boiling and bond numbers respectively, defined as:

$$Bl = \frac{q_p}{G \cdot h_{lv}} \tag{16}$$

$$Bo = \frac{g(\rho_l - \rho_v) D^2}{\sigma} \tag{17}$$

In the literature[16], the authors propose the following as the length at which the transition from bubble to annular flow occurs:

$$L_t = 96.65 (Bo^{0.5} \mathrm{Re})^{-0.258} Bl^{-1} \frac{\rho_g}{\rho_l - \rho_g} \frac{A_{cs}}{P_H} \tag{18}$$

Where A_{cs} and P_H are the cross-sectional area of the channel and the wetted perimeter of the channel, respectively.

Revellin and Thome[32] proposed a map of flow

regimes from data obtained for boiling refrigerant R134a and R245fa in circular tubes. In their work they distinguished three types of regimes: isolated bubble, coalesced bubble and annular. The geometrical and flow conditions used were: 0.509 and 0.790 mm ducts, heating length from 20 to 70 mm, mass flux density from 210 to 2094 kg/m^{2}s, heat flux density from 3.1 to 597 kW/m^2, saturation temperature from 26, 30 and 35 °C and subcooling from 2 to 15 °C. The transition between the regime of isolated bubbles to coalesced bubbles is fulfilled when:

$$x_{ba/bc} = 0.763\left(\frac{\mathrm{Re}, Bo}{We_v}\right)^{0.41} \tag{19}$$

For the transition from the coalesced to the annular bubble regime, the criterion is taken:

$$x_{bc/a} = 14 \cdot 10^{-5}\left(\mathrm{Re}_l^{1.47} We_l^{-1.23}\right) \tag{20}$$

Where *We* is the Weber number:

$$We = \frac{G^2 D}{\sigma \rho} \tag{21}$$

From the flow regimes that appear in minichannels and microchannels, it can be concluded that they are similar to those that appear in conventional channels: bubble, bullet, swirl and annular.

2.4 Equations used for the determination of the heat transfer coefficient in mini and microchannels

For the calculation of heat transfer during forced flow boiling in ducts, the correlations used can be divided into two groups:

Correlations that give an average heat transfer coefficient for the entire boiling process.

Correlations giving a local heat transfer coefficient as a function of steam quality. The group of correlations for the local heat transfer coefficient can be divided into:

(i) Improved model
(ii) Superposition model
(iii) Asymptotic model

In the improved model the heat transfer coefficient for two-phase flow (h_{df}) is calculated in the same way as for single-phase flow, considering the whole fluid as a liquid (h_L) and is affected by a factor that takes into account the influence of the presence of the two phases (E).

$$h_{df} = E \cdot h_L \tag{22}$$

The heat transfer coefficient for a single phase h_L is calculated by the equations of Gnielinski, cited by Kandlikar[21].

The superposition model assumes that the two-phase heat transfer coefficient is the sum of the single-phase convective component (h_{sf}) and the nucleated boiling component (h_{en}), that is:

$$h_{df} = h_{sf} + h_{en} \tag{23}$$

The asymptotic model is similar to the superposition model but in potential form, that is:

$$h_{df}^n = h_{sf}^n + h_{en}^n \tag{24}$$

In general, these models can be summarized as[33,34]:

$$h_{df} = \left[(E \cdot h_{sf})^n + (S \cdot h_{en})^n\right]^{1/n} \tag{25}$$

Here, the contribution of both parts is intensified and/or inhibited by the intensifying factor E or by the inhibition factor S. The exponent n takes into account the transition from one mechanism to the other. Depending on the value of n the superposition model can be subdivided into: Linear (n = 1)[35,36] and nonlinear ($n \neq 1$). Example of model with n = 2 is that of Liu[37] and with n = 3 is that of Steiner[38].

Models based on the flow structure are based on the superposition method and take into account the characteristics of the flow structure:

$$h_{df} = \frac{\theta_{\mathrm{seco}} h_v + (2\pi - \theta_{\mathrm{seco}}) h_{\mathrm{hum}}}{2\pi} \tag{26}$$

Where θ_{seco} is the angle of the dry perimeter, h_v is the heat transfer coefficient of the vapor phase, h_{hum} is the heat transfer coefficient of the wet perimeter corresponding to a non-linear superposition of effects taking into account the equivalent thickness of the liquid.

2.5 Empirical correlations

The correlations for the determination of the heat transfer coefficient in two-phase flow, in general, are based on heat transfer coefficients for liquid phase h_L[33,39] and on dimensionless criteria, that is:

$$h_{df} = h_L \cdot f(Bo, Fr, Bl, We, Co, X_{tt}, \dots)$$

(27)

The mean absolute error (MAE) of the correlations is determined according to the expression[40,41]:

$$EAM = \frac{1}{Np}\sum_{1}^{Np}\frac{|Y_{cal} - Y_{\exp}|}{Y_{\exp}} \times 100\%$$

(28)

Where Np is the number of points (data) analyzed, Y_{cal} is the calculated value and $Y_{\exp}$ is the experimental value.

Of the expressions used, the one with the lowest mean absolute error is the equation proposed by Basu[42]:

$$h_{df} = 1.44 \times 10^5 (Bl^2 We_D)^{0.32} (\frac{\rho_l}{\rho_v})^{0.31}$$

(29)

3. Conclusions

(1) It is necessary to develop a general criterion based on the thermophysical properties of the fluids and on the operating conditions to know the boundaries between conventional channel, mini-channels and microchannels.

(2) The product of the frequency and diameter of bubble detachment is an order of magnitude smaller in mini-channels and microchannels than in conventional channels.

(3) The structure of boiling flow in mini-channels and micronals is similar to that of conventional channels: bubble flow, bullet flow and annular flow.

(4) For the determination of the two-phase heat transfer coefficient the Basu expression, equation (29), is the one with the lowest mean absolute error.

Conflict of interest

The author declared no conflict of interest.

References

1. Tuckerman DB, Pease RFW. High performance heat sinking for VLSI. IEEE Electron Device Letters 1982; 2(5): 126–129.
2. Kandlikar SG. Nucleation characteristics and stability considerations during flow boiling in microchannels. Experimental Thermal and Fluid Science 2006; 30(5): 441–447. DOI: 10.1016/j.expthermflusci.2005.10.001.
3. Mudawar I. Assessment of high-heat-flux thermal management schemes. IEEE Transactions on Components and Packaging Technologies 2001; 24(2): 122–141.
4. Thome JR. Boiling in microchannels: A review of experiment and theory. International Journal of Heat and Fluid Flow 2004; 25(2): 128–139. DOI: 10.1016/j.ijheatfluidflow.2003.11.005.
5. Shah RK, Sekulic DP. Fundamental of heat exchanger design. New Jersey, USA: John Wiley & Sons, INC.; 2003. p. 9.
6. Kaew-On J, Sakamatapan K, Wongwises S, *et al.* Flow boiling heat transfer of R134a in the multiport minichannel heat exchangers. Experimental Thermal and Fluid Science 2011; 35(2): 364–374.
7. Kandlikar SG. A roadmap for implementing minichannels in refrigeration and air-conditioning systems-current status and future directions. Heat Transfer Engineering 2007; 28(12): 973–985. DOI: 10.1080/01457630701483497.
8. Jiang P, Fan M, Si G, *et al.* Thermal-hydraulic performance of small-scale micro-channel and porous-media heat-exchangers. International Journal of Heat and Mass Transfer 2001; 44(5): 1039–1051.
9. Okawa T. Onset of nucleate boiling in mini and micochannels: A brief review. Frontiers in Heat and Mass Transfer 2012; 3: 013001. DOI: 10.5098/hmt.v3.1.3001.
10. Kandlikar SG. Similarities and differences between flow boiling in microchannels and pool boiling. Heat Transfer Engineering 2010; 31(3): 159–167. DOI: 10.1080/01457630903304335.
11. Mehendale SS, Jacobi AM, Shah RK, *et al.* Fluid flow and heat transfer at micro-and meso-scales with application to heat exchanger design. Applied Mechanics Reviews 2000; 53(7): 175–193.
12. Kandlikar SG, Balasubramanian P. An extension of the flow boiling correlation to transition, laminar, and deep laminar flows in minichannels and microchannels. Heat Transfer Engineering 2004; 25(3): 89–93. DOI: 10.1080/01457630490280425.
13. Kew PA, Cornwell K. Correlations for the prediction of boiling heat transfer in small-diameter channels. Applied Thermal Engineering 1997; 17(8–10): 705–715.
14. Thome JR, Dupont V, Jacobi AM, *et al.* Heat transfer model for evaporation in microchannels. Part I: Presentation of the model. International Journal of Heat and Mass Transfer 2004; 47(14–16): 3375–3385.
15. Barber J, Brutin D, Sefiane K, *et al*. Bubble confinement in flow boiling of FC-72 in a “rectangular” microchannel of high aspect ratio. Experimental Thermal and Fluid Science 2010; 34(8): 1375–1388.
16. Harirchian T, Garimella SV. Flow regime-based modeling of heat transfer and pressure drop in microchannel flow boiling. International Journal of Heat and Mass Transfer 2012; 55(4): 1246–1260. DOI: 10.1016/j.ijheatmasstransfer.2011.09.024.
17. Brauner N, Maron DM. Identification of the range

of small diameters, conduits, regarding two phase flow pattern transitions. International Communications in Heat and Mass Transfer 1992; 19(1): 29–39.
18. Lee J, Mudawar I. Critical heat flux for subcooled flow boiling in microchannel heat sinks. International Journal of Heat and Mass Transfer 2009; 52(13–14): 3341–3352.
19. Zhang W, Hibiki T, Mishima K, *et al.* Correlation for flow boiling heat transfer at low liquid reynolds number in small diameter channels. Journal Heat Transfer 2005; 127(11): 1214–1221.
20. Tibiriçá CB, Ribatski G. Flow boiling heat transfer of R134a and R245fa in a 2.3 mm tube. International Journal of Heat and Mass Transfer 2010; 53(11–12): 2459–2468.
21. Kandlikar SG. A scale analysis based theoretical force balance model for critical heat flux (CHF) during saturated flow boiling in microchannels and minichannels. Journal of Heat Transfer 2010; 132(8): 081501. DOI: 10.1115/1.4001124.
22. Cooke D, Kandlikar SG. Pool boiling heat transfer and bubble dynamics over plain and enhanced microchannels. Journal of Heat Transfer 2011; 133: 052902. DOI: 10.1115/1.4003046.
23. Liu G, Xu J, Yang Y, *et al.* Seed bubbles trigger boiling heat transfer in silicon microchannels. Microfluidics and Nanofluidics 2010; 8(3): 341–359.
24. Thome JR, Consolini L. Mechanisms of boiling in micro-channels: Critical assessment. Heat Transfer Engineering 2010; 31(4): 288–297.
25. Zhuan R, Wang W. Simulation on nucleate boiling in micro-channel. International Journal of Heat and Mass Transfer 2010; 53(1–3): 502–512.
26. Kuo CJ, Kosar A, Peles Y, *et al.* Bubble dynamics during boiling in enhanced surface microchannels. Journal of Microelectromechanical Systems 2006; 15(6): 1514–1527. DOI: 10.1109/JMEMS.2006.885975.
27. Fu X, Zhang P, Huang CJ, *et al.* Bubble growth, departure and the following flow pattern evolution during flow boiling in a mini-tube. International Journal of Heat and Mass Transfer 2010; 53(21–22): 4819–4831.
28. Karayiannis TG, Shiferaw D, Kenning DBR, *et al.* Flow patterns and heat transfer for flow boiling in small to micro diameter tubes. Heat Transfer Engineering 2010; 31(4): 257–275.
29. Lee M, Cheung LSL, Lee YK, *et al.* Height effect on nucleation-site activity and size-dependent bubble dynamics in microchannel convective boiling. Journal of Micromechanics and Microengineering 2005; 15(11): 2121–2129. DOI: 10.1088/0960-1317/15/11/018.
30. Cheng L, Ribatski G, Quibén JM, *et al.* New prediction methods for CO_2 evaporation inside tubes Part I—A two-phase flow pattern map and a flow pattern based phenomenological model for two-phase flow frictional pressure drops. International Journal of Heat and Mass Transfer 2008; 51(1–2): 111–124.
31. Harirchian T, Garimella SV. A comprehensive flow regime map for microchannel flow boiling with quantitative transition criteria. International Journal of Heat and Mass Transfer 2010; 53(13–14): 2694–2702. DOI: 10.1016/j.ijheatmasstransfer.2010.02.039.
32. Revellin R, Thome JR. A new type of diabatic flow pattern map for boiling heat transfer in microchannels. Journal of Micromechanics and Microengineering 2007; 17(4): 788–796.
33. Gnielinski V. New equations for heat and mass transfer in turbulent pipe and channel flow. International Chemical Engineering 1976; 16(2): 359–368.
34. Bertsch SS, Groll EA, Garimella SV, *et al.* A composite heat transfer correlation for saturated flow boiling in small channels. International Journal of Heat and Mass Transfer 2009; 52(7–8): 2110–2118.
35. Gungor KE, Winterton RHS. A general correlation for flow boiling in tubes and annuli. International Journal of Heat and Mass Transfer 1986; 29(3): 351–358.
36. Jung D, Radermacher R. Prediction of evaporation heat transfer coefficient and pressure drop of refrigerant mixtures. International Journal of Refrigeration 1993; 16(5): 330–338.
37. Liu Z, Winterton RHS. A general correlation for saturated and subcooled flow boiling in tubes and annuli, based on a nucleate pool boiling equation. International Journal of Heat and Mass Transfer 1991; 34(11): 2759–2766.
38. Steiner D, Taborek J. Flow boiling heat transfer in vertical tubes correlated by an asymptotic model. Heat Transfer Engineering 1992; 13(2): 43–69.
39. Shiferaw D, Karayiannis TG, Kenning DBR, *et al.* Flow boiling in a 1.1 mm tube with R134a experimental results and comparison with model. International Journal of Thermal Sciences 2009; 48(2): 331–341.
40. Basu S, Ndao S, Gregory J, *et al.* Flow boiling of R134a in circular microtubes-Part II study of critical heat flux condition. Journal of Heat Transfer 2011; 133(5): 051503. DOI: 10.1115/1.4003160.
41. Fang X, Shi R, Zhou Z, *et al.* Correlations of flow boiling heat transfer of R-134a in minichannels: Comparative study. Energy Science and Technology 2011; 1(1): 1–15.
42. Basu S, Ndao S, Michna GJ, *et al.* Flow boiling of R134a in circular microtubes-Part I study of heat transfer characteristics. Journal of Heat Transfer 2011; 133(5): 051502. DOI: 10.1115/1.4003159.

Thermal Science and Engineering (2021) Volume 4 Issue 1
doi:10.24294/tse.v4i1.1506

CASE REPORT

Combined operation mode of sub-critical W-flame boiler and coal mill optimized numerical simulation

Lun Ma*, Qingyan Fang, Dengfeng Tian, Cheng Zhang, Gang Chen

State Key Laboratory of Coal combustion, Huazhong University of Science and Technology, Wuhan 430074, China. E-mail: malun3g@126.com

ABSTRACT

The flow, combustion, heat transfer and NO_x emission characteristics of a 600 MW subcritical W-flame boiler were numerically simulated under different combined operation modes of coal mills, and compared with the measured results. The results show that the combustion, average residence time, burnout rate, NO_x emission characteristics and temperature distribution near the side wall of pulverized coal particles in the furnace have different effects on the combined operation mode of pulverized coal. In the combustion efficiency of give attention to two or more things, screen superheater section of fly ash carbon content and flue gas temperature of entrance at the same time, compared with six coal mill run at the same time, 5 coal mill run, shut down near the side wall of the coal mill is beneficial to reduce NO_x emission concentration, to achieve the emission reduction, at the same time under the wing wall and side wall area chamber of a stove or furnace slagging significantly reduce.

Keywords: Subcritical W-Flame Boiler; Combustion Optimization; Combined Operation Mode of Coal Mill; NO_x Emission Characteristics; Numerical Simulation

ARTICLE INFO

Received: 17 January 2021
Accepted: 9 March 2021
Available online: 14 March 2021

1. Introduction

Low volatile coal resources in China have large reserves and wide distribution, but the low volatile content of coal powder makes it difficult to ignite and has poor stable combustion characteristics. W-flame boiler has good adaptability to the combustion of low-volatile coal and other inferior coals, so it has been widely used in China in recent decades. However, most W-flame boilers have such disadvantages as ignition delay, poor stability, low burnout rate (the carbon content of fly ash is 8%–15%) and high NO_x emission (the emission mass concentration of NO_x under $\varphi(O_2)$ = 6% is 1100–2000 mg/m^3)[1]. In order to ensure the fire stability of pulverized coal, the combustion belt is generally laid around the lower furnace and the furnace arch area, resulting in a higher temperature in the furnace, which is an important reason for the higher NO_x emissions from the outlet of the furnace. Gb13223-2012 Emission Standard of Heavy Gas Pollutants for Thermal Power Plants puts forward stricter requirements for NO_x emission control of W-flame coal burning boiler, and limits the emission mass concentration of NO_x (NO_2 as measurement standard) of W-flame coal burning boiler to within 200 mg/m^3. In this regard, in recent years, a series of combustion control technologies and methods to reduce NO_x emissions have been developed, and have been widely used in coal-fired power plant boilers, such as reburning technology,

exhaust air technology, shade deviation technology and flue gas recycling technology, etc. Among them, the exhaust air technology has been widely used in domestic coal burning power plants because of less investment and more obvious NO_x emission reduction effect.

There are more and more literatures on the combustion, slagging and NO_x emission of pulverized coal boilers by means of numerical simulation. Many scholars have carried out a great deal of research on the low-NO_x combustion technology of tangential combustion boilers[2-4]. Fang *et al.*[5] conducted numerical simulation on the NO_x emission characteristics of an ultra-supercritical offset combustion boiler under different combined operation modes of coal mills. The results show that the combustion characteristics and NO_x emission characteristics of boilers are affected by different combined operation modes of coal mills. Scholars at home and abroad have also carried out some studies on W-flame boiler by using numerical simulation methods[6-9], but there are few numerical simulations on the combined operation modes of different coal mills. Fang *et al.*[10] conducted numerical simulation on slagging characteristics of a DG1025/18.2-II4W boiler when it was fired with different types of coal, and the results showed that the slagging locations were mainly the wing wall of lower furnace, the area of furnace arch burner and local areas of front and rear walls. Stopping the coal mill near the wing wall could effectively reduce the slagging tendency of the wing wall. Kuang *et al.*[11,12] studied the influence of burnout air position and burnout air Angle of furnace arch on combustion characteristics and NOx emission characteristics of a 350 MWe pulverized coal boiler through numerical simulation and experiment. The results showed that burnout air was sent from the furnace arch to the lower furnace at 40°, which could effectively reduce NO_x emission. According to Li[13], such as high efficiency low NO_x combustion was put forward with the combination of number value simulation principle and technology, including dual channel vane shade separation technology, reasonable decorate shade pulverized coal and air flow and secondary air downdip technology, burning wind technology and alleviate the wing wall slagging technology, part or all of these techniques was applied to some boiler, good results are obtained. Gao *et al.*[14] studied the influence of boiler structure on W-flame by means of numerical simulation.

Numerical study on the flow, combustion, heat transfer and NO_x emission characteristics of a 600 MW subcritical W-flame boiler under rated full load condition and different combined operation mode of coal mills is carried out, which provides reference for the optimization of combustion and pollutant emission characteristics of the same type of boiler.

2. Overview of boiler

The boiler is a type π drum boiler of 1,778 T/h subcritical natural circulation, primary intermediate reheating, single furnace, open air arrangement, full steel suspension structure, balanced ventilation, solid state slag discharge, and is manufactured by Dongfang Boiler (Group) Co. The furnace is divided into upper and lower parts, total. The height is 50.150 m, the size of the upper furnace is 34.481 m × 9.906 m, and the size of the lower furnace is 34.481 m × 16.012 m. The lower furnace bore is double arched, and a burning belt is laid on the water cooling wall and near the furnace arch. Using W flame combustion mode, the whole boiler is equipped with 6 double inlet and double outlet coal mills (A coal mill ~ F coal mill), each mill with 6 burners, A total of 36 burners, symmetrically arranged on the furnace arch before and after the furnace. The corresponding arrangement of coal grinder and burner nozzle is shown in **Figure 1**.

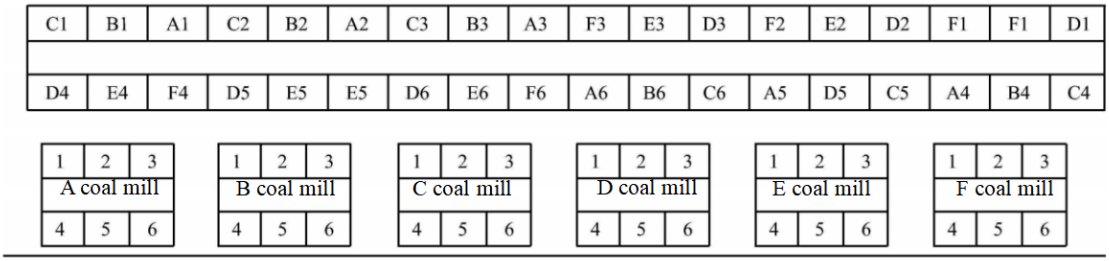

Figure 1. Schematic diagram of coal mill layout.

3. Mathematical model and calculation conditions

3.1 Mathematical model

Pulverized coal combustion includes a series of complex physical and chemical processes such as pulverized coal pyrolysis, combustion, turbulent flow and heat and mass transfer. The standard K-ε bidirectional turbulence model is used to simulate the turbulent gas flow. The probability density function (PDF) model is used for turbulent gas combustion. A parallel reaction model is used for coal pyrolysis. Coke combustion adopts dynamic/diffusion control reaction rate model. The motion of pulverized coal particles is modeled by particle random orbit. PI model is adopted for radiation heat transfer calculation. The detailed description of the model is referred to the reference[15].

For NO_x modeling, the main consideration is NO, and the "post-treatment" method is used to calculate the NO production. The generation of NO in pulverized coal furnace mainly involves two kinds of mechanism: thermal type NO and fuel type NO. Due to the small proportion of fast type NO and its main presence in the flame of hydrocarbon rich fuel, it will not be considered here. Thermal NO is mainly generated by the oxidation of N_2 in the air. Affected by temperature and O_2 concentration, it can be described by the extended Zeldovich machine[16]. For the [O] and [OH] groups, the partial equilibrium method is used. Fuel type NO is mainly generated by the pyrolysis and oxidation reaction of nitrogen in fuel, which is the main source of NO in pulverized coal combustion. The generation and reduction process of fuel type NO is not only related to the characteristics of coal, the form and distribution of nitrogen functional groups in fuel, but also closely related to combustion conditions (such as temperature and O_2 concentration, etc.). Fuel type NO is described by de Soete model[17]. Nitrogen in fuel is mainly distributed in volatile matter and coke, and nitrogen in volatile matter is released in the form of HCN and NH_3, while nitrogen in coke is directly oxidized to NO.

3.2 Calculation conditions

According to the actual physical structure size of the boiler, the geometric model is established, and the furnace is divided into cold ash bucket region, burner region, burnout region, screen superheater region and high temperature reheater region. The grid is divided into hexahedral grids with high quality. Grid encryption of the burner area to reduce the numerical calculation error. After the grid independence test, the total number of the model grid is 3.85 million. The boiler furnace geometric model and mesh division are shown in **Figure 2**.

3.3 Calculation conditions

Based on the rated load condition, the numerical simulation is carried out under ABCDEF (working condition 1), ABCDF (working condition 2), ABCDE (working condition 3) and ABCEF (working condition 4) combined operation mode. Under the rated load condition of the boiler, the excess air coefficient is 1.12, the volume fraction of operating O_2 is 2.25%, the primary air volume and the exhausted air volume (71.99 kg/s) account for 11.11% of the total air volume, and the total secondary air volume is 471.62 kg/s, of which the exhausted air volume is 129.6 kg/s. The regional excess air coefficient of the main burning is 0.8.

The primary air temperature is 423 K, and the secondary air temperature is 607 K. A, B, C, D, E, F coal mill combined operation mode the mass flow rate of pulverized coal in the next wind is 1.087 kg/s, and the mass flow rate of pulverized coal in the poor air is 0.242 kg/s. ABCDF, ABCDE and ABCEF coal mills combined operation formula for the next air pulverized coal mass flow is 1.304 kg/s, poor air pulverized coal mass flow is 0.290 kg/s; Each burner distributes air evenly, and coal quality analysis is shown in **Table 1**.

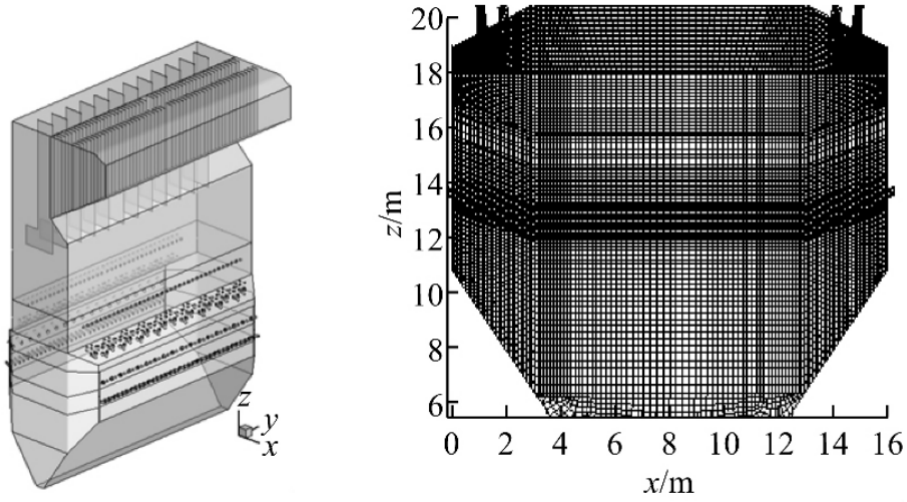

Figure 2. Model and grid division.

Table 1. Quality analysis of coal

Parame-ter	Industrial analysis/%				Elementary analysis					$Q_{net,ar}$ /(kj·kg^{-1})
	w (V_{ad})	*w* (M_{ad})	*w* (A_{ad})	*w* (FC_{ad})	*w* (C_{ad})	*w* (H_{ad})	*w* (O_{ad})	*w* (N_{ad})	*w* (S_{ad})	
Value	8.27	2.00	39.80	49.94	51.56	2.26	2.46	0.68	1.24	17,370

Burners and exhaust air adopt mass inlet boundary conditions, and inlet flow and temperature are set according to operating parameters. The outlet boundary condition adopts pressure outlet, and the pressure setting value is -60 Pa. The wall surface of the boiler adopts non-slip and temperature boundary strip, different temperatures are set in different sections, and the radiant emissivity of the wall surface is set as 0.6. The diameter of pulverized coal particles is set according to Rosin-Rammler equation, the minimum diameter of pulverized coal particles is 5 μm, the maximum diameter is 250 μm, the average diameter is 54 μm, and the distribution index is 1.5. The prefactor and activation energy of coke combustion kinetic parameters are 0.0016 kg·s·Pa/m^2 and 8.37 × 107 kJ/kmol.

The Simple algorithm is used to solve the pressure and velocity coupling of the discrete equations. In order to ensure the precision of calculation, the discrete scheme of quadratic upwind interpolation is used to solve the governing equation. The convergence conditions of the calculated results are as follows: (1) the residual of the energy equation is less than 10^{-6}, and the residual of other equations is less than 10^{-5}; (2) the furnace outlet velocity and temperature do not change with the iteration.

4. Results and discussion

4.1 Verification of simulation results

According to the method in “power station boiler performance test specification”, the boiler is tested under the load of 600 MW without burnout air, 600 MW with burnout air and 450 MW with burnout air. **Table 2** shows the comparison between simulated and measured results. As can be seen from **Table 2**, under 600 MW load without burnout air, the relative error of flue gas oxygen integral number obtained by simulation and measurement is 2.56%, the relative

error of NO_x emission mass concentration is 11.06%, and the relative error of carbon content of fly ash is 0.03%. Under the loading of 600 MW exhaust air, the relative error of simulated and measured flue gas oxygen volume fraction is 3.74%, The phase error of NO_x emission mass concentration is 3.99%, and the relative error of carbon content in fly ash is 0.43%. Under the load of 450 MW exhaust air, the relative error of oxygen volume fraction of flue gas, NO_x emission mass concentration and carbon content of fly ash are 2.65%, 2.63% and 0.19% respectively. The simulated values of flue gas oxygen volume fraction and NO_x emission mass concentration under 600 MW and 450 MW loads are consistent with the measured values, indicating that the model and grid used can reasonably predict the flow, combustion, heat transfer and NO_x emission characteristics in the boiler.

Table 2. Comparison between the simulation and the actual results

Name	Load/MW	The flue gas oxygen body	NO_x emission mass concentration/（$mg \cdot m^{-3}$）	Fly ash contains carbon/%
Simulation results	600	2.28	1,335	1.98
Measured results	No burnout air	2.34	1,501	2.01
Simulation results	600	2.44	759	2.03
Measured results	Burnout air	2.52	751	2.46
Simulation results	450	2.57	631	2.52
Measured results	Burnout air	2.64	648	2.71

4.2 Distribution of each parameter along the furnace height

Figure 3 shows the distribution of temperature along the axis of the primary air nozzle. It can be seen from **Figure 3** that the trend of pulverized coal ignition curve is basically the same under different working conditions. According to literature[18] and literature[19], the point with a temperature of 1000 K is defined as the ignition point of pulverized coal, and the distance from the ignition point to the nozzle exit is the ignition distance. The results show that the ignition distance of pulverized coal airflow changes little when the pulverized coal mill is close to the side wall pulverized coal mill (working condition 4) when the pulverized coal mill is close to the side wall pulverized coal mill combined with the 5 pulverized coal mills, compared with the 6 pulverized coal mills, indicating that the shutdown of pulverized coal mill close to the side wall pulverized coal mill has little influence on the stable combustion characteristics.

Figure 4 shows the distribution of average temperature of flue gas along the height of furnace under different working conditions. It can be seen from **Figure 4** that in the cold ash hopper area, the average temperature of flue gas in the cross-section of the furnace increases rapidly with the increase of the height of the furnace. Area in the main combustion chamber of a stove or furnace section flue gas temperature fluctuation, this is because the z = 12 m and z = 16 m near the secondary air and exhaust air mixed with furnace cross-section flue gas temperature is reduced, the region near the upper exhaust wind area chamber of a stove or furnace section reached the highest average temperature of flue gas furnace under the condition of 1 section is close to 1,500 ℃, the average temperature of flue gas However, the temperature difference between 2 and 4 conditions decreased significantly, and the peak mean temperature difference reached about 50 K in this region. Since the exhaust air volume is large, accounting for 20% of the total secondary air volume, the average temperature of flue gas in the furnace section decreases significantly when the exhaust air is mixed near the section z = 23 m. However, the unburned coke in the later period continues to burn and release heat after the exhaust air is mixed, and the average temperature of flue gas in the furnace section increases. In the upper furnace area, the average temperature of flue gas in the furnace section decreases gradually with the increase of the height of the furnace, because the water wall absorbs a lot of heat. It can also be seen from **Figure 4** that in the main combustion region, working conditions 2 ~ 4 are equivalent to postponing pulverized coal combustion on the basis of

working condition 1, and the average temperature of flue gas in the cross-section of the furnace will decrease. In the upper burnout zone, the coal char is further burned in the later stage, and the average temperature distribution of flue gas in the cross-section of the furnace is basically the same, but they are all lower than the working condition 1.

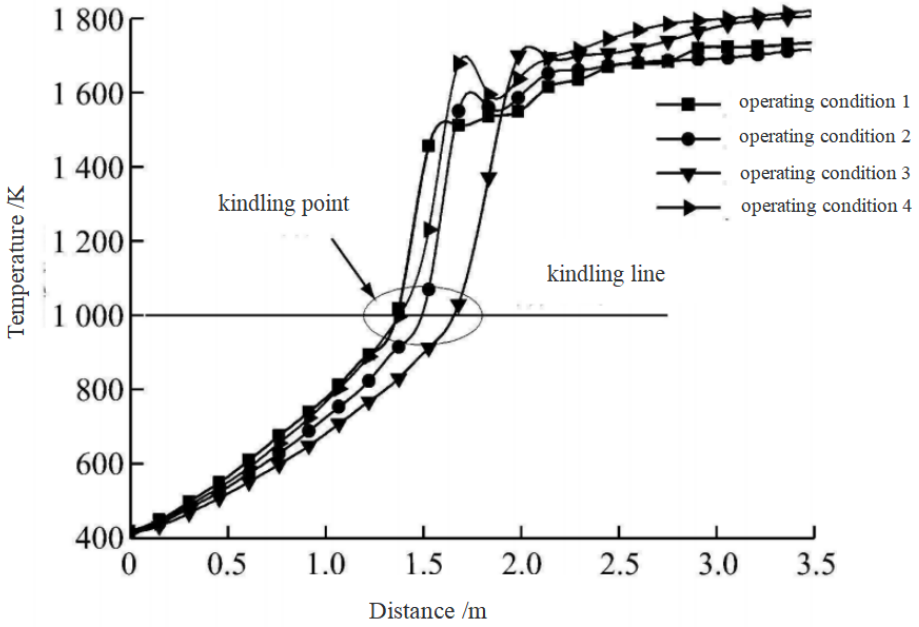

Figure 3. Temperature distribution along the primary air nozzle axis (A3 nozzle).

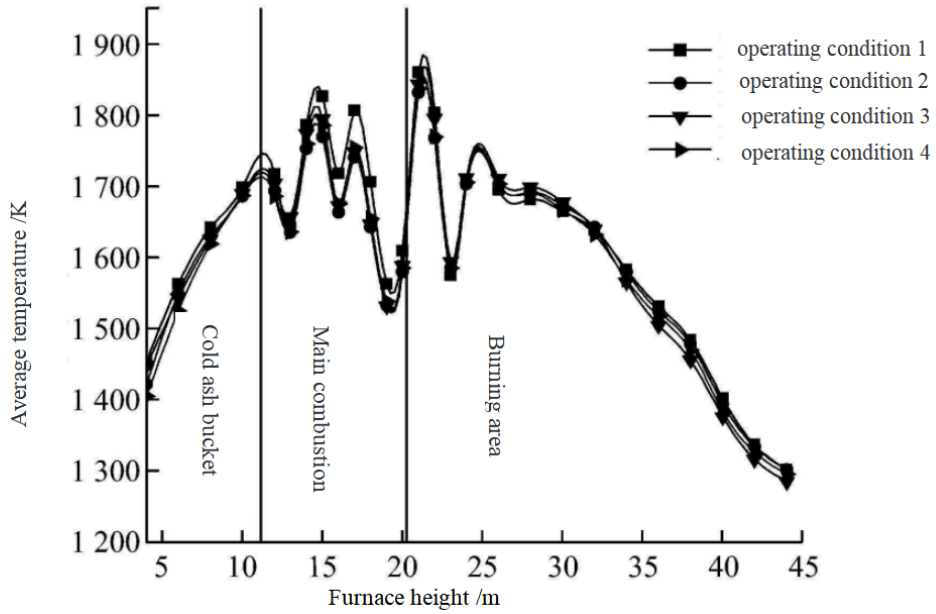

Figure 4. Average flue gas temperature distribution along the height of furnace.

Figure 5 shows the distribution of CO volume fraction φCO along the furnace height. As can be seen from **Figure 5**, the distribution trend of φCO along the furnace height is consistent under different working conditions. In the burner area, the excess air coefficient is 0.8, in the low oxygen rich fuel atmosphere, coal powder into the furnace after the high temperature flue gas reflux coil effect of rapid ignition combustion, due to the excess of fuel to generate a large number of CO, resulting in the area φCO rapidly rising. High φCO is beneficial to reduce NO generation. This is because the amount of volatiles precipitated from low volatile coal during pyrolysis is very small, and the amount of ni-

trogen gas is even less. Moreover, the expansibility of coke generated from pyrolysis is very small, which may be due to the low amount of gas produced by low volatile coal pyrolysis, low internal pressure and very small pores. Therefore, coke has very few reactive points, and the reducibility of available coke to NO is very small[20], so the reduction performance of CO can be fully utilized to effectively inhibit the generation of NO. It can also be seen from **Figure 5** that in the main combustion area, φCO under working conditions 2 ~ 4 is higher than that under working conditions 1, which is conducive to enhancing the reducing atmosphere in the main combustion area, inhibiting NO generation, and achieving the purpose of reducing NO_x emissions.

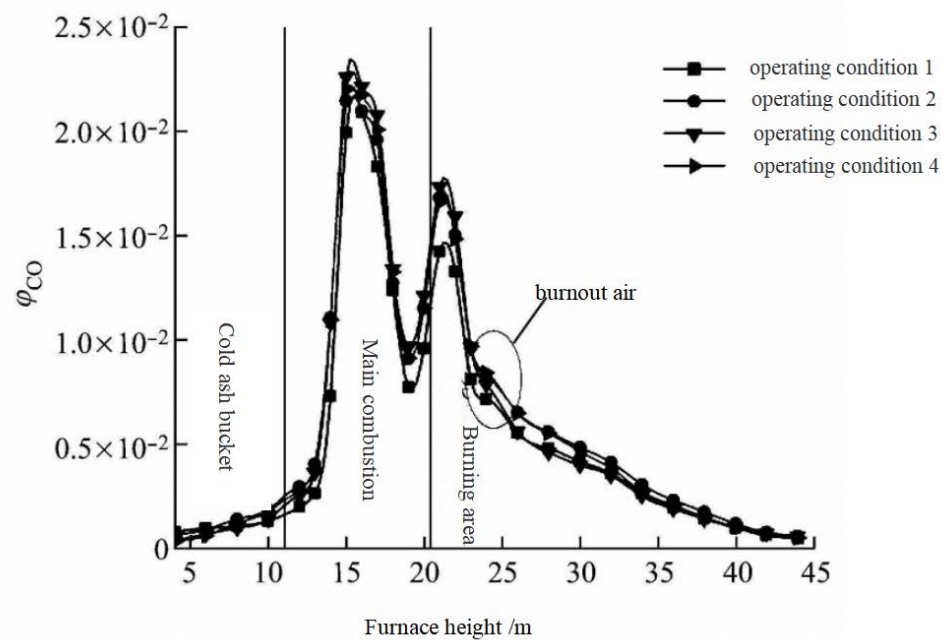

Figure 5. CO volume fraction distribution along the height of furnace.

Figure 6 shows the distribution of NO volume fraction φNO along the furnace height. As can be seen from **Figure 6**, the distribution trend of φNO along the furnace height is basically the same under different working conditions. In the main combustion area, pulverized coal rapidly ignites and burns after entering the furnace, and nitrogen is constantly precipitated in the coal, which can be roughly divided into two stages: volatile analysis stage and coke combustion precipitation stage[21]. Therefore, the formation of NO from nitrogen in fuel can be divided into two stages: uniform phase formation of volatile matter and heterogeneous phase formation of coke. HCN and NH_3 released in the volatilization process react with O_2 to produce a large amount of NO. In the process of coke combustion, nitrogen in coke is oxidized to NO; at the same time, N_2 in the air also reacts with O_2 to produce a large amount of NO. φNO presents two wave peaks along the high square direction. The formation of the first steep wave peak is mainly due to the rapid volatilization and combustion, and the formation of NO is relatively concentrated. Coke combustion is a relatively slow process, and the formation of the second wave peak is mainly due to the mixture of exhaust air, nitrogen in coke is oxidized to NO. The excess air coefficient in the main combustion region is 0.8, and low oxygen and rich fuel lead to incomplete combustion of pulverized coal to generate a large amount of CO, which is in the reducing atmosphere condition. At the same time, NO reacts with HCN, NH_3 and coal coke, and NO is reduced, so φNO decreases after the two wave peaks.

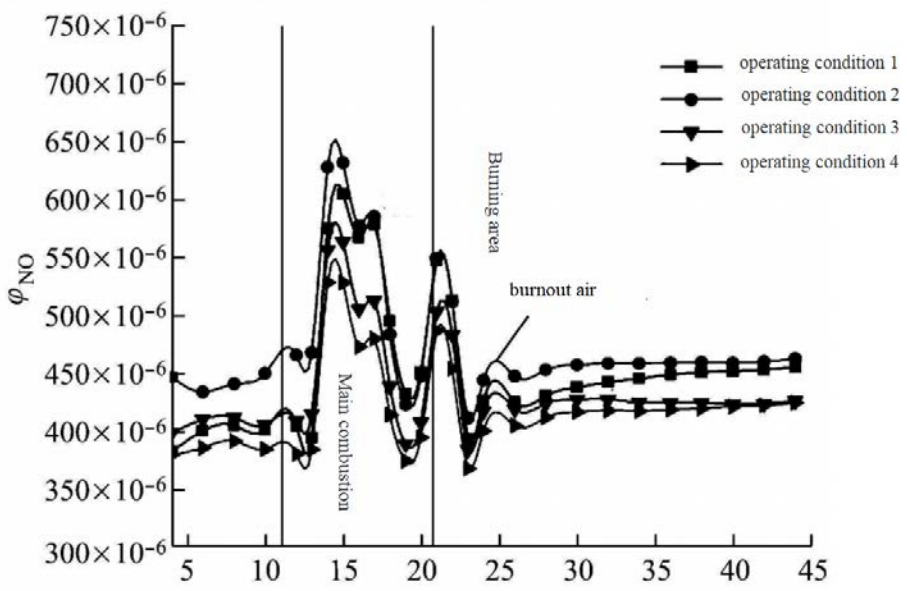

Figure 6. NO volume fraction distribution along the height of furnace.

The combined running mode of different coal mills has certain influence on NO generation. When the shutdown is close to the side wall coal mill (working condition 4), the average temperature of the main combustion area is obviously lower than that of working condition 1 (i.e. basic working condition), which can effectively inhibit the generation of thermal NO, and at the same time φCO is higher, reducing gas. Strong atmosphere, can effectively reduce the generated NO.

4.3 Furnace exit parameters

The simulation results from working conditions 1 to 4 show that the average temperature of smoke gas level at the cross-section of the break flame Angle inlet is 1,484 K, 1,479 K, 1,456 K and 1,470 K, which indicates that the average temperature of smoke gas at the entrance section of the large-screen superheater changes little when the E mill is in operation or out of operation. When F mill is shut down, the average temperature of flue gas at the entrance section of large screen superheater decreases most significantly. When the mill D is shut down, the average temperature of the inlet section of the large-screen superheater decreases less than that of the working condition 1, which is helpful to avoid the overtemperature of the large-screen superheater and avoid a large temperature decrease.

Figure 7 shows the average residence time of pulverized coal particles in the furnace and the carbon content of fly ash at the outlet of the furnace under different working conditions. As can be seen from **Figure 7**, the average residence time of pulverized coal particles in the furnace under working conditions 1 to 4 is 8.922 s, 8.424 s, 8.611s and 8.622 s respectively, and the carbon content of simulated fly ash is 1.81%, 2.51%, 2.59% and 2.24%. Compared with operating condition 1, the carbon content of fly ash from operating condition 2 to operating condition 4 increases by 0.70%, 0.78% and 0.43%, respectively, and the burnout rate decreases, but the carbon content of fly ash from operating condition 4 increases by the least.

Figure 8 shows the NO_x emission mass concentration at the outlet of the furnace under different working conditions. As can be seen from **Figure 8**, the NO_x emission mass concentrations under working conditions 1 to 4 are 759 mg/m^3, 770 mg/m^3, 715 mg/m^3 and 702 mg/m^3, respectively. This shows that the combined operation mode of different mills has a certain impact on the NO_x emission mass concentration of W-flame boiler, which is mainly caused by the difference in the temperature and reducing atmosphere of the main combustion area when the combined operation of different mills. Compared with working condition 1, the NO_x emission mass concentration of working condition 2 is increased, and the NO_x emission mass concentration of working condition 3 and 4 is

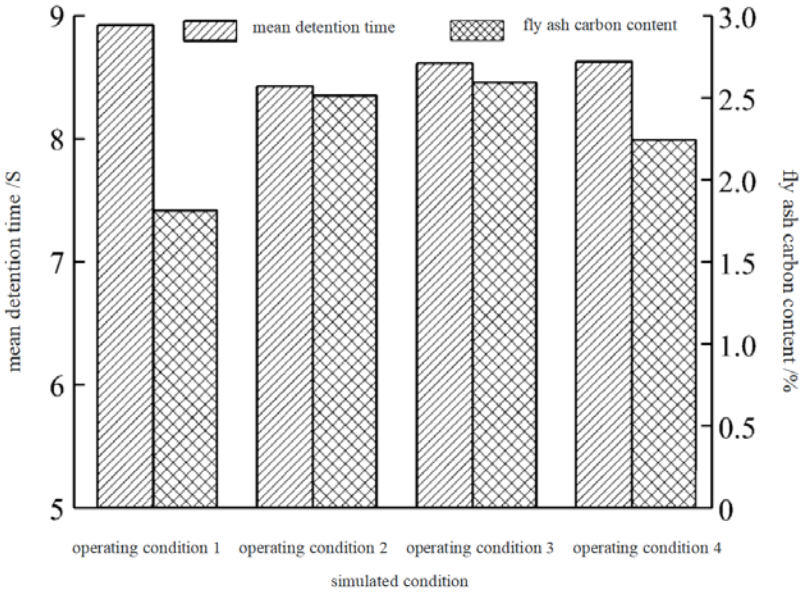

Figure 7. Average residence time of coal particles in the furnace and the carbon content in fly ash at the furnace outlet.

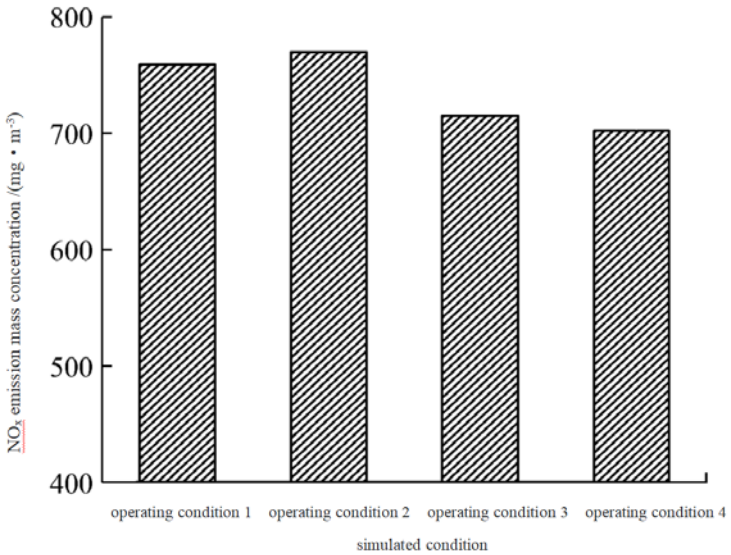

Figure 8. NO_x emission at the furnace outlet.

significantly reduced, and the NO_x emission mass concentration of working condition 4 is the most obvious when the shutdown is close to the side wall coal mill. The above analysis shows that the combined operation of 5 coal mills and the shutdown close to the side wall coal mill are conducive to reducing the NO_x emission mass concentration at the furnace outlet while taking into account the combustion efficiency. The actual operation test shows that the mass concentration of NO_x emission from the furnace outlet is 835 mg/m^3 when the coal mill close to the side wall is shut down, and 891 mg/m^3 when the coal mill is kept running.

Figure 9 shows the temperature distribution near the side wall surface (about 0.2 m away from the left wall) in the main burning area of W-flame boiler under different working conditions. It can be seen from **Figure 9** that the high temperature area of the lower wall surface is the largest in working condition 3, which may increase the tendency of high temperature slagging on the side wall surface. Under the condition of 4 side near the wall surface temperature decrease, think in terms of temperature, which is beneficial to reduce the possibility of side wall surface temperature and slagging, this is because the shutdown D grinding, low near the side wall surface temperature of the wind mixed with in time, reduces the side near the wall

surface temperature, at the same time can be formed near the side wall surface oxidizing atmosphere, and effectively reduce settlement slag. It can be seen that changing the combined operation mode of coal mills has a significant impact on the temperature distribution near the side wall surface in the main combustion area of the boiler. When 5 coal mills are in operation and out of operation close to the side wall coal mill, the possibility of high temperature slagging on the side wall surface in the main combustion area is smaller than that of other combined operation modes of coal mills. In the actual operation, the burner near the side wall was shut down. After a period of operation, it was found that the slagging degree of the wing wall and side wall area was significantly reduced in the middle minor repair.

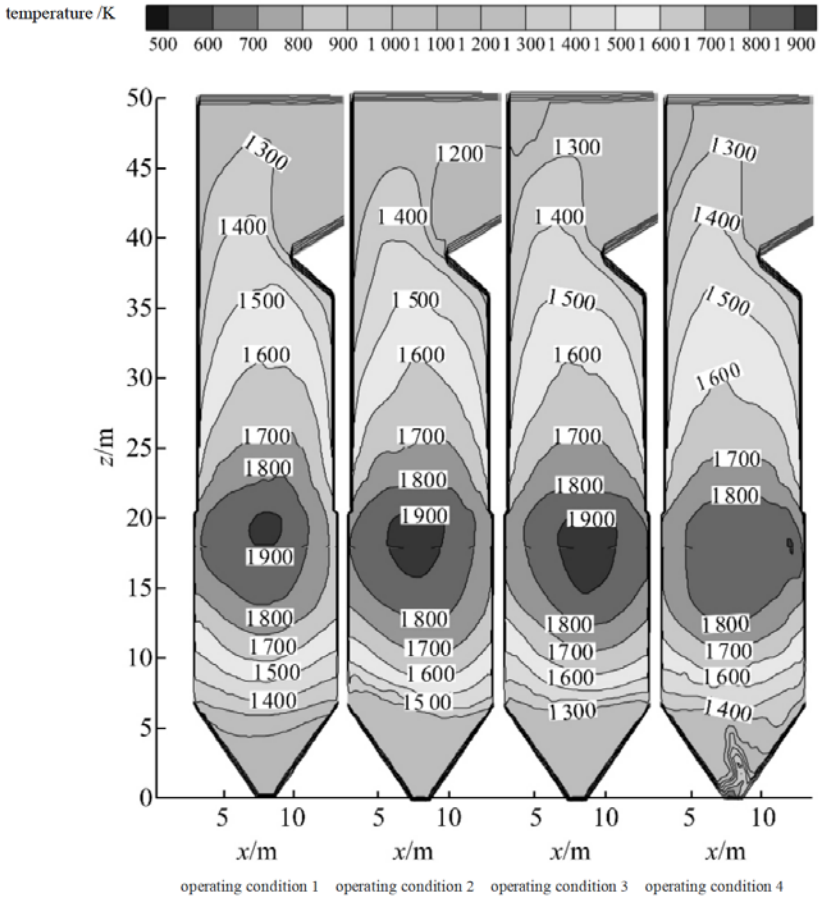

Figure 9. Temperature distribution near the side walls under different conditions.

5. Conclusion

The combustion, average residence time, burnout rate, NO_x emission characteristics and temperature distribution near the side wall surface of pulverized coal particles in the furnace have different effects on the combined operation mode of pulverized coal. While taking into account combustion efficiency, flue gas temperature at the entrance section of large screen superheater and carbon content of fly ash, compared with 6 mills running at the same time, the formula of 5 mills running in combination and stopping operation close to the side wall coal mill has the advantage of reducing NO_x emission concentration, reaching the reduction of emission. At the same time, the slagging degree of the wing wall and side wall area of the lower furnace is obviously reduced.

Conflict of interest

The authors declared no conflict of interest.

References

1. Kuang M, Li Z, Zhang Y, *et al*. Asymmetric combustion characteristics and NO_x emissions of a down-fired 300 MWe utility boiler at different boiler

loads. Energy 2012; 37(1): 580–590.
2. Guo Y. Numerical simulation and experimental study of low NO_x combustion technology for ultrafine powder recombustion. Beijing: North China Electric Power University; 2006.
3. Zeng H. Study on large capacity boiler high efficiency low NO_x combustion technology. Boiler Manufacturing 2001; (1): 1–11.
4. Li Z, Liu G, Zhu Q, *et al*. Combustion and NO_x emission characteristics of a retrofitted down-fired 660 MWe utility boiler at different loads. Applied Energy 2011; 88(7): 2400–2406.
5. Fang Q, Wang H, Chen G, *et al*. Optimal simulation on the combination mode of mills for an ultra-supercritical utility boiler. Proceedings of the CSEE 2011; 31(5): 1–6.
6. Kuang M, Li Z, Zhu Q, *et al*. Arch-and wall-air distribution optimization for a down-fired 350 MWe utility boiler: A cold-modeling experimental study accompanied by real-furnace measurements. Applied Thermal Engineering 2013; 54(1): 226–236.
7. Miao C, Wang J. Analysis of asymmetric burning problem in a W-shaped flame boiler of 600 MW unit. Thermal Power Generation 2005; (12): 48–51.
8. Liu R, Hui S, Yu Z, *et al*. Effect of air distribution on aerodynamic field and coal combustion in an arch-fired furnace. Energy & Fuels 2010; 24(10): 5514–5523.
9. Kuang M, Li Z, Xu S, *et al*. Improving combustion characteristics and NO_x emissions of a down-fired 350 MWe utility boiler with multiple injection and multiple staging. Environmental Science & Technology 2011; 45(8): 3803–3811.
10. Fang Q, Wang H, Wei Y, *et al*. Numerical simulations of the slagging characteristics in a down-fired pulverized-coal boiler furnace. Fuel Processing Technology 2010; 91(1): 88–96.
11. Kuang M, Li Z, Ling Z, *et al*. Impact of the over fire air location on combustion improvement and NO_x abatement of a down-fired 350 MWe utility boiler with multiple injection and multiple staging. Energy & Fuels 2011; 25(10): 4322–4332.
12. Kuang M, Li Z, Ling Z, *et al*. Effect of over fire air angle on flow characteristics within a small-scale model for a deep-air-staging down-fired Furnace. Energy Conversion and Management 2014; 79(3): 367–376.
13. Li Z, Ren F, Liu G, *et al*. Combustion technologies of down-fired boilers with high efficiency and low-NO_x emissions. Journal of Power Engineering 2010; 30(9): 645–651, 662.
14. Gao Z, Sun X, Song W, *et al*. Numerical simulation on the effect of structure on flame for W flame boiler. Proceedings of the CSEE 2009; 29(29): 13–18.
15. Smoot LD, Smith PJ. Coal combustion and gasification. New York, USA: Plenum Press; 1989.
16. Hill SC, Smoot LD. Modeling of nitrogen oxides formation and destruction in combustion systems. Progress in Energy and Combustion Science 2000; 26(4/5/6): 417–458.
17. De Soete GG. Overall reaction rates of NO and N_2 formation from fuel nitrogen. 15th Symposium (International) on the Combustion. Pittsburgh, USA 1975; 15(1): 1093–1102.
18. Heng C, Moght Aderi B, Gupta R, *et al*. A computational fluid dynamics based study of the combustion characteristics of coal blends in pulverized coal-fired furnace. Fuel 2004; 83(11): 1543–1552.
19. Gera D, Mathur M, Freman M. Parametric sensitivity study of a CFD-based coal devolatilization model. Energy & Fuels 2003; 17(3): 794–795.
20. Li J, Wang Q, Li H, *et al*. The formation mechanism and control of NO_x in low volatile matter pulverized coal combustion. Journal of Power Engineering 2005; 25(Sup): 12–17.
21. Cen K, Yao Q, Luo Z. High order combustion. Hangzhou: Zhejiang University Press; 2002.

Thermal Science and Engineering (2021) Volume 4 Issue 1
doi:10.24294/tse.v4i1.1508

ORIGINAL RESEARCH ARTICLE

Wolfram Mathematica, exact solutions for heat transfer methods applied to extrusion processes

Antonio-Jiménez Ramos[1*], Juan Francisco-Puertas Fernández[2], Margarita J.-Lapido Rodríguez[3], Julio Rafael-Gómez Sarduy[3], Yulier-Jiménez Santana[4], Fidel-Sosa Núñez[4]

[1] *Empresa de Producciones Plásticas Vasil Levski, Cuba. E-mail: antonio@petrocasa.minem.cu*

[2] *Departamento Mecánica, Facultad de Ingeniería, Universidad de Cienfuegos, Cuba.*

[3] *Centro de Estudio de Energía y Medio Ambiente (CEEMA), Facultad de Ingeniería, Universidad de Cienfuegos, Cuba.*

[4] *Universidad de Guanajuato, México.*

ABSTRACT

Computer programs for the solution of everyday problems are very common because of the speed with which results can be obtained, which by traditional methods would be very laborious and especially those in which the solutions take repeated calculations. The work intends to demonstrate how, through programming, applying the exact solution method, fast and precise results can be obtained on similarities and differences between different geometries in heat transfer, which demonstrate the behavior, according to parameters, under equal conditions (geometric properties, diameters, lengths, thicknesses, volumes) and physical properties (thermal conductivity, specific heat and density), appreciating how they influence results such as cooling times, production according to the physical properties and design of the equipment, consumption rates, core and surface temperatures and others, according to the plastic pipe extrusion method, necessary in production processes that require constant monitoring.

Keywords: Extrusion Processes; Simple Geometries; Modeling; Physical Properties; Heat Transfer; Wolfram Mathematica Software

ARTICLE INFO

Received: 8 February 2021
Accepted: 12 March 2021
Available online: 29 March 2021

1. Introduction

Wolfram Mathematica, by its very nature, is used in the scientific areas of engineering in its various mathematical and computational specialties. Commonly considered a computer algebra system, Mathematica is also a powerful tool for general-purpose programming. Hence, it can be used for multiple solutions to engineering problems[1-3], being a language that is constantly updated, always with greater application possibilities.

Generally, the solution to heat transfer problems in pipes and plates in the extrusion technology are performed by the first term approximation method, taking into account the ease of calculation, especially for problems where a high accuracy is not required, being able to reach with it up to 96%–98%, approximately, making it very complex to reach higher accuracies without using the exact solution method.

The exact solution method requires numerical analysis for its solution due to the complexity of its equations, hence the use of different software. In this case, the solution with Wolfram Mathematica 8.0 always starts from the conformation of the equations that represent

each of these geometries, for the case of plates, Cartesian coordinates, and for pipes, cylindrical coordinates, which must be meticulously developed to obtain the desired results, since the solution for each of them have similarities[4-6].

The work aims to demonstrate, the feasibility of using this software, to achieve fast results and with the pressures that are required, for each of the particularities that are presented, being able to be a way of comparison of parameters, such as the energy behavior of different geometries. In this case, plates and pipes, in volumes, taking into account similar parameters and raw materials, in terms of production, consumption rates, cooling times, external and internal temperatures and others[7-9].

2. Materials and methods

In heat transfer, there are many ways to solve problems used in engineering, in this first case, the solution for programming in Wolfram Mathematica 8.0, corresponds to a plate, surrounded by a convecting fluid, at the final temperature T_f, which is instantly introduced into the fluid under conditions where the resistance to heat transfer is very small, see in **Figure 1**. By the concept of plate and that the fluid is the same and is on both sides, there is symmetry and it turns out that the convective coefficient h_c, will be the same between both half-plates, so that, considering this infinite plate of thickness (esp. = 2 L) for which at time (t = 0), there is a known temperature distribution and in which there are no edge effects, the differential equation[1,10,11], equation (1), applies.

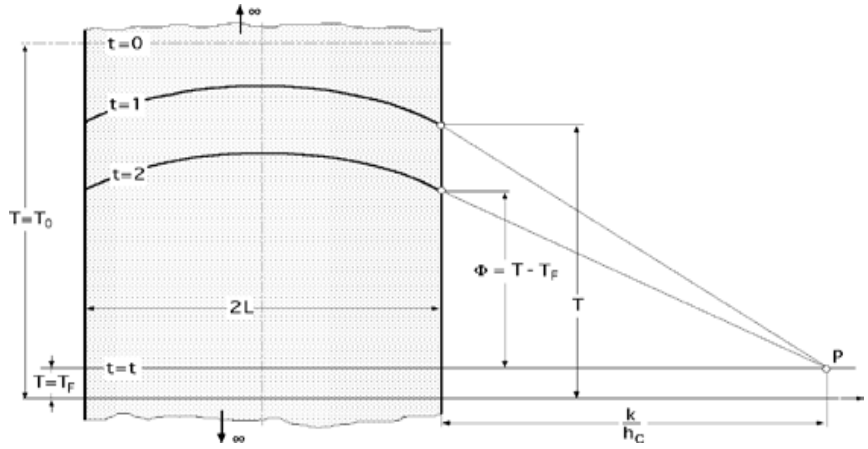

Figure 1. Interpretation of the convection boundary condition on an infinite plate.

$$\alpha \frac{\partial^2 T}{\partial x^2} = \frac{\partial T}{\partial t}, \text{ with T} = (x,t) \tag{1}$$

By changing the variable $\Phi = T - T_f$ with $T_f \neq 0$; equation (2):

$$\alpha \frac{\partial^2 \Phi}{\partial x^2} = \frac{\partial \Phi}{\partial t} \tag{2}$$

Whose general solution is equation (3):

$$\Phi = \lambda e^{-\lambda^2 \alpha \cdot t}[B_1 Sen(\lambda x) - B_2 Cos(\lambda x)] \tag{3}$$

For $T = 0$, $-L \leq X \geq L$; $\Phi = f(x)$ or To 2 for $T > 0$ it will be satisfied; equation (4):

$$x = 0: \left(\frac{\partial \emptyset}{\partial x}\right)_{x=0} = 0, \qquad x = \pm L$$

$$-k\left(\frac{\partial \emptyset}{\partial x}\right)_{x=\pm L} = h_c \emptyset$$

$$\left(\frac{\partial \emptyset}{\partial x}\right)_{x=\pm L} = -\frac{h_c}{k}\emptyset = a_1 \emptyset \tag{4}$$

As the fluid on both sides of the plate is the same, then $\Phi_{-x} = \Phi_{+x}$, $h_c/k = Cte = -a_1$ and the equality is satisfied for any value of Φ.

Taking into account the boundary condition $x = 0$; equation (5):

$$(\frac{\partial \phi}{\partial x})_{x=0} = 0 = \lambda e^{-\lambda^2 \alpha \cdot t}[B_1 Cos(\lambda x) - B_2 Sen(\lambda x)]_{x=0} \Rightarrow B_1 = 0 \tag{5}$$

The solution reduces to equation (6):

$$\phi = Be^{-\lambda^2 \alpha \cdot t} Cos(\lambda x) \tag{6}$$

The boundary condition at ($x = \pm L$) allows to obtain the values of λ; equation (7):

$$\left(\frac{\partial \emptyset}{\partial x}\right)_{x=\pm L} = -\frac{hc}{k}\emptyset \Rightarrow B\lambda e^{-\lambda^2 \alpha \cdot t}[-Sen(\lambda x)]_{x=L} = -\frac{hc}{k}[Be^{-\lambda^2 \alpha \cdot t} Cos(\lambda x)]_{x=L}$$

$$Sen(\lambda L) = \frac{hc}{k\lambda} Cos(\lambda L); Cotg(\lambda L) = \frac{\lambda L}{Bi} \tag{7}$$

This equation is satisfied for an infinite number of values of the parameter (λL), so that for a given value of L, its solutions are found for various values of λ, intersecting at the curves: equation (8),

$$y = Cotg(\lambda L); y = \frac{\lambda L}{Bi} \tag{8}$$

Note the dependence of the equation on B_i.

Therefore, the temperature distribution is a series of the form; equation (9):

$$\frac{\phi}{\phi_0} = \frac{T_c - T_f}{T_0 - T_f} = 2\sum_{n=1}^{\infty} \lambda_n e^{-\lambda^2_n \alpha \cdot t} \frac{Sen(\lambda_n L)Cos(\lambda_n x)}{\lambda_n L + Sen(\lambda_n L)Cos(\lambda_n L)} \tag{9}$$

In which λ_n is the nth root of the equation; equation (10):

$$Cotg(\lambda_n L) = \frac{\lambda_n L}{Bi} \tag{10}$$

The initial condition $\Phi = f(x) = \Phi_0 = Cte$, for (t = 0); equation (11):

$$f(x) = \sum_{n=1}^{\infty} B_n Cos(\lambda_n L) \tag{11}$$

From which B_n is obtained, taking into account the theory of orthogonal functions.

The expression of the temperature distribution, on the infinite plate, as a function of position and time; equation (12):

$$\phi = 2\sum_{n=1}^{\infty} \lambda_n e^{-\lambda_n^2 \alpha \cdot t} \frac{Cos(\lambda_n x)}{\lambda_n L + Sen(\lambda_n L)Cos(\lambda_n x)} \int_0^L f(x)Cos(\lambda_n x)d_x \tag{12}$$

For the particular case, in which the first boundary condition would be of the form.

$\Phi = f(x) = \Phi_0 =$ Cte the above equation becomes; equation (13):

$$\frac{\phi}{\phi_0} = \frac{T_s - T_f}{T_0 - T_f} = 2\sum_{n=1}^{\infty} \lambda_n e^{-\lambda^2_n \alpha \cdot t} \frac{Sen(\lambda_n L)Cos(\lambda_n x)}{\lambda_n L + Sen(\lambda_n L)Cos(\lambda_n L)} \tag{13}$$

The temperature $\Phi_c = T_c - T_f$ on the axis of the plate $(x = 0)$ of thickness (2 L) is equation (14):

$$\frac{\phi_c}{\phi_0} = \frac{T_c - T_f}{T_0 - T_f} = 2\sum_{n=1}^{\infty} \lambda_n {}_n e^{-\lambda^2_n \alpha \cdot t} \frac{Sen(\lambda_n {}_n L)}{\lambda_n L + Sen(\lambda_n L)Cos(\lambda_n L)} \tag{14}$$

For the second case, programming in Wolfram Mathematica 8.0, for the pipe, the procedure is similar to the previous one, but the characteristic length of the plate (L), which varies from the surface to the center, is replaced by the (r), which is the radius, which varies from the surface of the pipe to its inner radius, another difference, in this case, is that it is solved with the equation in cylindrical coordinates and the Bessel and Newman equations are used, due to the temperature distribution that exists in this type of geometry, in addition, in the plate, there is dependence of the Biot number and in the pipe there is not equation (15):

$$\frac{\partial^2 \phi}{\partial r^2} + \frac{1}{r}\frac{\partial \phi}{\partial r} = \frac{1}{\alpha}\frac{\partial \phi}{\partial t}, with\ \phi = T - T_f \tag{15}$$

Where Φ, is the dimensionless temperature, which is a function of radius and time, T is the temperature in degrees Celsius, T_f is the final temperature. Applying the method of separation of variables, the resulting ordinary differential equations and their solutions are equation (16):

$$\frac{d^2 R}{dr^2} + \frac{1}{r}\frac{dR}{dr} = -\lambda^2 R$$

General solutions:

$$R = B_1 J_o(\lambda r) + B_2 Y_o(\lambda r) \tag{16}$$

Where R is a function, which depends only on the radius, J_0 is the zero-order first-species Bessel function, Y_0 is the zero-order second-species Bessel function (Newman function), B_1 and B_2 are constants; equation (17):

$$\frac{d\theta}{\theta} = -\lambda^2\alpha \cdot dt, general\ solution: \theta = B_{3e}{}^{-\lambda^2\alpha \cdot t}$$

(17)

Where θ is a function that depends only on time and B is a constant.

If it were a solid cylinder, then, as it cannot admit in its axis ($r = 0$), an infinite solution, because $Y_0 = -\infty$ results that B_2 has to be (0) and we obtain an equation of the form; equation (18):

$$R = B_1 J_o(\lambda r)$$

(18)

The general solution that provides the temperature distribution; equation (19):

$$\phi = B_3 e^{-\lambda^2\alpha t} B_1 J_0(\lambda r) = B e^{-\lambda^2\alpha t} J_0(\lambda r)$$

(19)

In which B and λ are constants that are determined by the boundary conditions.

The initial condition is:

$$t = 0;\ 0 cor = R;\ \Phi = f(r) o' \Phi_0$$

The condition for an abrupt change of temperature on the lateral surface of the infinite cylinder; equation (20):

$$\phi = T - T_f$$

$$\phi_{r=R} = 0 = B e^{-\lambda^2\alpha t} J_0(\lambda r)\ ;\ J_0(\lambda R) = 0 \Rightarrow\ J_0(\lambda_n R) = 0$$

(20)

Therefore, equation (21):

$$\phi = B e^{-\lambda^2\alpha t} J_0(\lambda r)$$

(21)

Which has to be fulfilled for any value of t with the conditions:

1) To, $t = 0$; $0 \le r \le R$; $\Phi = f(r) o' \Phi_0 = T_0$

2) To, $t > 0$; $\partial\Phi / \partial\, r_{r=R} = -(-h_c/k)T$

Taking into account the second boundary condition and that $(\partial/\partial r)J_0(\lambda r) = -\lambda J_1(\lambda_1)$; equation (22):

$$B e^{-\lambda^2\alpha t}[-\lambda J_1(\lambda r)]_{r=R} = -\frac{h_c}{k}[B e^{-\lambda^2\alpha t} J_0(\lambda r)]_{r=R} \Rightarrow \lambda R = \frac{J_0(\lambda R)}{J_1(\lambda R)} Bi; \frac{J_0(\lambda R)}{J_1(\lambda R)} = \frac{\lambda R}{Bi} = y$$

(22)

Which is satisfied for infinite values of λ with the intersection of the curves.

Being the values of λ_n roots of the equation; equation (23):

$$\frac{J_0(\lambda_n R)}{J_1(\lambda_n R)} = \frac{\lambda_n R}{Bi}$$

(23)

For the case of a pipe, with initial conditions: $t = 0$; $ri \le r \le re$; $\Phi = f(r)$ or Φ_0, the second constant does not become zero, as in the cylinder[1], this is also sought, with the boundary conditions according to **Figure 2**. Its obtaining is more complex, because the constant B_2, cannot be zero, because the center (r = 0), does not enter the domain and in order to obtain a solution to the problem, a constant is written as a function of the other, from the boundary conditions and thus, applying the theory of orthogonal functions, an expression for this constant is obtained. Boundary conditions for $t > 0$; equation (24):

$$r = re:\ \left(\frac{\partial\phi}{\partial r}\right)_{r=re} = a1 \cdot \phi = -\frac{h_c}{k}\phi\ \ r = ri:\ \left(\frac{\partial\phi}{\partial r}\right)_{r=ri} = 0$$

(24)

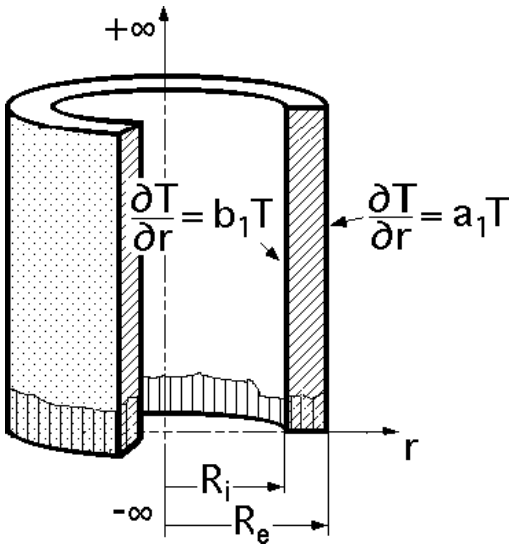

Figure 2. Interpretation of the convection boundary condition in an infinite pipe volume element.

From the boundary conditions, the transcendent equation is obtained, whose roots are the λ_n of the solution equation; equation (25):

$$\lambda_n[J_1(\lambda_n re)Y_1(\lambda_n ri) - J_1(\lambda_n ri)Y_1(\lambda_n re)] - a_1[J_0(\lambda_n re)Y_1(\lambda_n ri) - J_1(\lambda_n ri)Y_o(\lambda_n re)] = 0$$

(25)

Where J_1 is the first-species, first-order Bessel function and Y_1 is the second-species, first-order

Bessel function.

It turns out that the general solution of the problem is a linear combination of infinite solutions, for infinite self values of λ; equation (26):

$$\phi(r,t) = \sum_{n=1}^{\infty} e^{-\lambda^2 \alpha \cdot t} \frac{\int_{ri}^{re} r\phi_o[J_0(\lambda_n r)Y_1(\lambda_n ri) - J_1(\lambda_n ri)Y_o(\lambda_n r)]dr}{\int_{ri}^{re} r[J_0(\lambda_n r)Y_1(\lambda_n ri) - |J_1(\lambda_n ri)Y_o(\lambda_n r)^2 dr} \cdot [J_0(\lambda_n r)Y_1(\lambda_n ri) - J_1(\lambda_n ri)Y_o(\lambda_n r)$$

(26)

The dimensional temperature is a function of time and radius, (r_i, r_e).

$$\text{Tempi} = \Phi\,(ri,\, t)$$

where: tempi is the a-dimensional temperature at the inner radius of the pipe.

tempe = Φ (re, t): A-dimensional temperature at the outer radius of the pipe.

Finally, the temperature is calculated for any time and thickness[14]. For the temperature at the surface or outer radius (T_s); equation (27):

$$\phi(r_e, t) = \frac{T_s - T_\infty}{T_i - T_\infty}$$

(27)

And for the intermediate temperature or inner radius (T_0); equation (28):

$$\phi(ri, t) = \frac{T_o - T_\infty}{T_i - T_\infty}$$

(28)

Assume that convection is forced because water is driven by a pump.

To give a solution to all these cases, it is necessary to know or make some calculations such as. Width: l1 = Height: l2 Length: Therefore, the area of the bathtub will be: Ab = l1 × l2.

Water flow: Q,

Calculation of water velocity: Area of water flow, *Aa* = Area of bath - Area of (pipe, cylinder, or plate).

Pipe area = π. (D/2)2. If the water flow is known then, $Q = A_a^V$ and $V = Q/A_a$.

The heat transfer coefficient (h) is calculated by calculating the Reynolds number to determine whether the regime is laminar or turbulent and using the corresponding Nusselt correlations; equation (29):

$$\text{Reynolds: } R_{eD} = \frac{\rho V D}{\mu}$$

(29)

Where ρ = Water density (kg/m^3), V = Velocity of water (m/s), D = Diameter or thickness (m); μ = Dynamic viscosity of water (N·s/m^2). With red and the Prandt number (P_r), the Nusselt Number (N_{us}) is calculated. P_r is calculated by equation (30):

$$P_r = \frac{\nu}{\alpha} = \frac{\mu Cp}{k}$$

(30)

Where:

ν = rate of momentum diffusion and α = rate of heat diffusion.

μ = Dynamic viscosity of water; Cp = Specific heat of water, k = Thermal conductivity of water W/m.K.

This value is easily found in tables. Calculation of the Nusselt number; equation (31):

$$\overline{Nu} = C Re_D^m Pr$$

(31)

Applicable regime for: $0.4 < R_e < 44 \times 10^5$; $P_r \geq 0.7$; where: C and m are constants taken by table according to Reynolds value. Other correlations; equation (32) and (33):

$$N_{US} = 0.3 + \frac{0.62 \cdot Re_D^{0.5} \cdot P_r^{\frac{1}{3}}}{\left(1 + \left(\frac{0.4}{P_r}\right)^{\frac{2}{3}}\right)^{0.25}} \cdot \left(\left(1 + \frac{Re_D}{282000}\right)^{\frac{5}{8}}\right)^{0.8}; \quad (Re_D \cdot P_r > 0.02)$$

(32)

$$N_{US} = \mathrm{P_r}^{0.3} \cdot (0.35 + 0.47 \cdot \mathrm{Re}^{0.52})$$

(33)

Applicable regime for: $R_e > 200$ and $P_r > 0.7$.

Convective coefficient; equation (34):

$$h = Nus \frac{k}{D}$$

(34)

The physical properties of the material used were:

K = 0.22 W/m. ^{0}K thermal conductivity. P = 1,400 kg/m^3 density.

Cp = 1,273 J/kg^{0}k specific heat.

In addition, the properties of the solid, which is cooled or heated, such as density, specific heat and thermal conductivity, must be known or calculated,

and with these elements we proceed to the programming. The flow rate of the machine used was 270 kg/h, with 143 kW of general power, 85% of this power was considered, equal to 122 kW.

The program starts, with the input of the data: Pipe diameter or width of the plate (mm), thickness for both (mm), initial material temperature (°C), cooling water temperature (°C), desired temperature (°C) for the surface, inner radius or center, machine flow rate (kg/h), heat exchanger dimensions, material and water properties, 0 type of exchange surface. With these data, it performs the cooling time calculation, based on the flow according to machine design. Subsequently, calculate T_i and T_e according to the desired river temperature, or center and with this data the time it takes for the cooling to reach the desired temperature, depending on the case, which takes into account the thermophysical properties of the material, using the working tool (Wolfram Mathematica 8.0 software), it is compared with the desired temperature, if it is higher or lower, it is added, or subtract the desired value, until the necessary difference is reached, according to the required accuracy.

Table 1. Comparison between 90 mm diameter pipe and plate with their equivalent dimensions and properties

Thickness (mm)	5.4	4.3	3.5	2.7	2.2
Time to reach desired temperature in r_e (sec.) Piping	235	184	147	111	89
Time to reach desired temperature in r_e (sec.) Plate	215	163	128	96	75
Temperature in *ri* (°C)	62	55	50	47	44
Temperature in *re* (°C)	30	30	30	30	30
Production meters of pipe 8 h according to (ρ)	1,075	1,333	1,622	2,083	2,542
Production meters of pipe 8 h according to (PF)	978	1,247	1,562	2,078	2,602
Plate meter production 8 h according to (ρ)	1,011	1,269	1,559	2,021	2,480
Plate meter production 8 h according to (PF)	1,072	1,413	1,800	2,451	3,072
Pipe volume 1 m^3	0.00116	0.001158	0.00095	0.00074	0.00061
Plate volume 1 m^3	0.00152	0.001215	0.00099	0.00076	0.00062
Plate-pipe volume difference Plate-pipe volume difference 1 m^3	0.00037	0.000057	0.00004	0.00002	0.00001

Note: (ρ) Raw material density as predominance, (PF) Thermophysical properties as a function of the cooling process.

The result of this process is a cooling time, which is related to the thermo-physical properties of the raw material introduced, with which it is carried out, a new calculation of the maximum flow rate for the machine, which is not directly related to the design flow rate, and from these results, the other results are obtained, the higher efficiency of the equipment, is that the result. According to the thermo-physical properties, is as close as possible to the productive design of the machine, calculating from this result. The report includes the production and optimal consumption indexes, at the end it makes a report of all the indicators that are requested, giving the possibility to know the values of each of the equations and variables that participate in the process. A sample of this is shown in **Table 1**, which is only a sample of a requested report. The graphs with which the intervals and coefficients are calculated for the plate and the pipe are different, since the plate is dependent on the Biot number and the pipe is not, due to different geometries, as shown in **Graphs 1** and **2**, for a thickness of 4.3 mm. **Figure 3** shows the calculation procedure described.

3. Results and discussions

With the application of Wolfram Mathematica 8.0 as a working tool for the solution of heat transfer problems by the exact solution method, the following results, among others, can be obtained.

Develop very fast calculations in real time, of each of the parameters necessary to obtain the consumption and production index for each product.

The possibility of taking parameters, such as the same temperature difference at the extruder outlet and at the bath inlet, equal thicknesses, cooling distances, temperature at the inner and outer radius, as well as the thermo-physical properties of the material, and demonstrate how the cooling times, productions, consumption rates and volumes of the geometries under study vary.

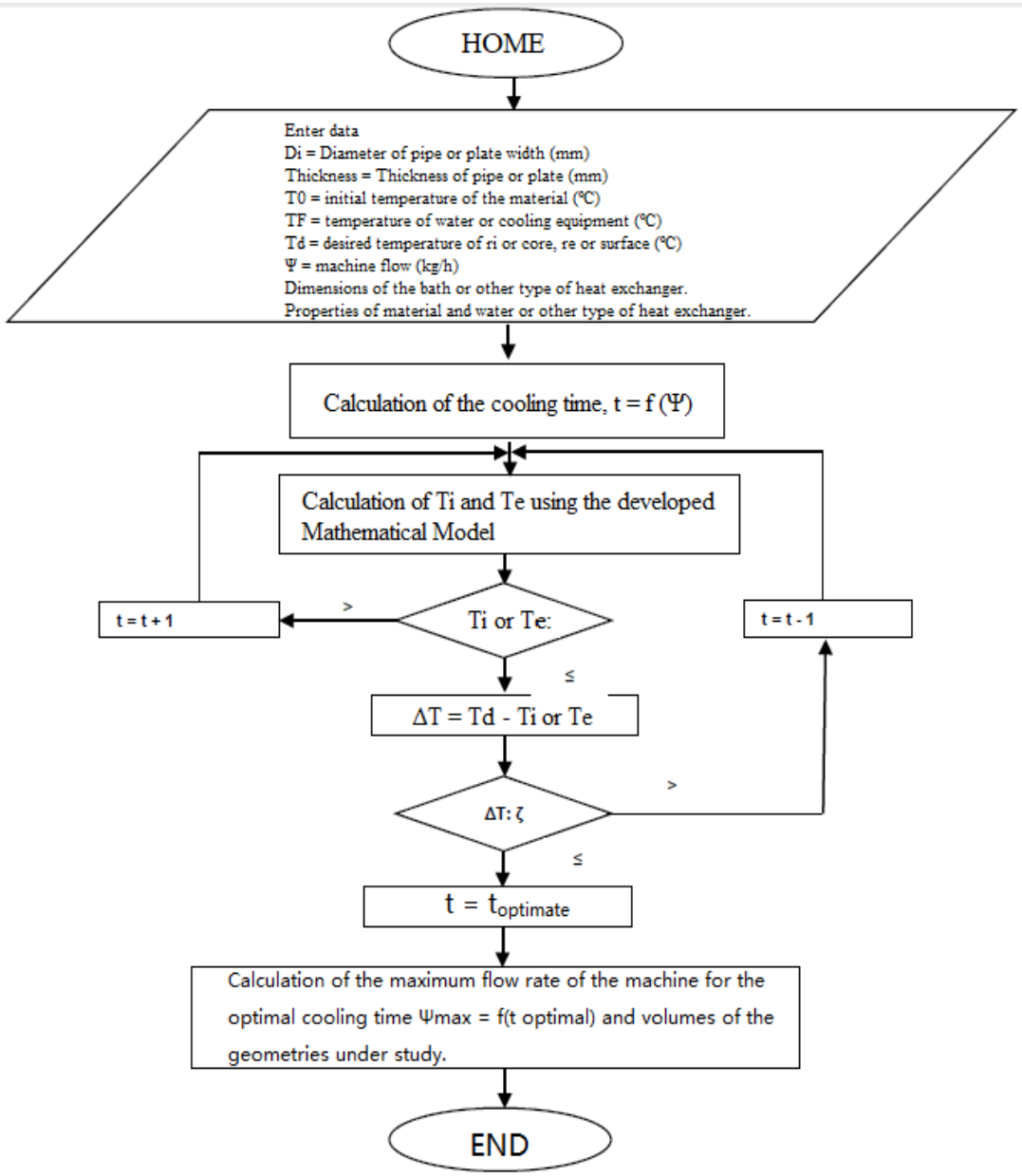

Figure 3. Flow chart of the described procedure.

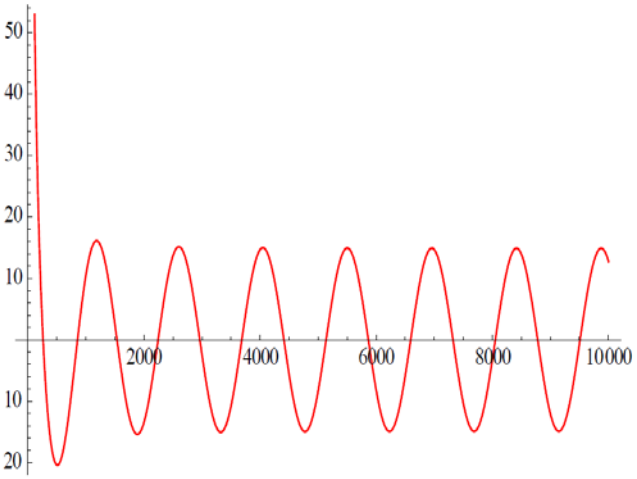

Graph 1. infinite solutions for infinite eigenvalues λ_n, for pipe-line.

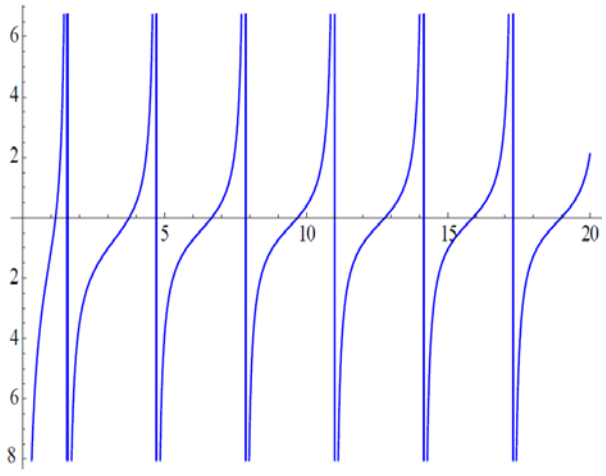

Graph 2. Infinite solutions for infinite eigenvalues λ_n, for plate.

Table 1 shows a report of parameters obtained with the application of the tool, to which others can be added. The level of precision in real time, which is wanted to be obtained as it is from (n = 1 to ∞ t will be fixed according to the need of the process to be executed, (productive or investigative), facility that exists for using a programming of this type.

Another example of the benefits of this application can be seen when comparing, based on its accuracy, how the volumes and cooling time decrease as the thickness decreases, tending to zero, demonstrating this condition, that truly, the thinner the thickness, the closer the values between both geometries, however, it shows the inappropriateness of using, for the solution to problems of pipes with thin thicknesses, the treatment as if it were a plate, since the rest of the indicators to be measured do not present the same situation.

With the tool, it was possible to define the two main parameters to be taken into account to achieve productive and energetic efficiency of this process. The density, with direct correspondence with the flow of the equipment and the density achieved with the thermo-physical properties of the material, depending on the cooling process, which provides one more parameter to be taken into account for any energy and production analysis.

4. Conclusions

With the use of this work tool (Wolfram Mathematica 8.0), it was demonstrated that in order to develop any analysis of the productive process and define an energetic improvement in the plastic pipe extrusion machines, it is necessary to take into account two essential elements. For the productive flow, as the main basis, the density of the raw material and from the energetic point of view, the conjugation of the thermo physical properties present in the same, since both act differently in the process.

Another example of the benefits of this application can be seen when comparing, based on its accuracy, how the volumes and cooling time decrease as the thickness decreases, tending to zero, demonstrating this condition, which is truly true, the thinner the thickness, the closer the values between both geometries are, however, it is shown that it is not convenient to use, for the solution to problems of pipes with thin thicknesses, the treatment as if it were a plate, since the rest of the indicators to be measured do not present the same situation.

It was also demonstrated that the volumes of the plate and the pipe are reduced and tend to zero as their thicknesses decrease, but referred to the production increases in the pipe with respect to the flow of the machine, and according to the characteristics of the raw material, the production is lower than that of the plate, with these characteristics the consumption indexes behave in the same way.

Conflict of interest

The authors declared no conflict of interest.

References

1. González de Brito F. Condición de Contorno de convección en salidos infinitos (Spanish) [Boundary condition of convection in infinite outflows]. 8th ed. In: Concepción Hernández M (editor). Pedro Fernández Díez, España: Ingeniería Térmica, Universidad de Cantabria; 2003.
2. Mackowski DW. Transient and one dimensional conduction. In: Conduction heat transfer notes for MECH 7210. Auburn: Mechanical Engineering Department, Auburn University; 2011. p. 80–82.
3. Abascal R. Ecuaciones diferenciales de orden superior. Parte 5. Funciones de Bessel (Spanish) [Higher order differential equations. Part 5. Bessel functions]. Argentina: Facultad Regional Avellaneda, Buenos Aires; 2006. p. 1–60.
4. Romero-Ramírez Y. High density polyethylene piping manufacture for water transfer applications in the Holplast facility, Holguin. Ciencia & Futuro 2014; 4(2): 12–42.
5. Suéscum J, Correa C, Rigail-Cedeño A. Mejora de la eficiencia de una extrusora de doble tornillo utilizada en la fabricación de tuberías de PVC (Spanish) [Improving the efficiency of a twin-screw extruder used in PVC pipe manufacturing]. Revista Tecnológica-ESPOL 2007; 20(1): 25–30.
6. Osswald TA, Aquite W, Ramírez D, *et al*. Retos en la Industria de procesamiento de plásticos y compuestos (Spanish) [Challenges in the plastics and composites processing industry]. Dyna 2012; 79(175): 20–28.
7. Vargas-Isaza CA, Posada-Correa JC, Jaramillo-Zapata LY, *et al*. Energy consumption in plastic

industry-review of studies developed. Revista CEA 2015; 1(1): 93–107.
8. Jiménez Ramos A, Borroto Nordelo A, Montesino Pérez M, *et al*. Improve of the energy efficiency in the processes of plastic pipe extrusion. Ingeniería energética 2015; 36(2): 220–229.
9. Holman JP. Transferencia de calor (Spanish) [Heat transfer]. 8th ed. São Paulo: MacGraw-Hill Companies, inc.; 2013. p. 117–130, 175–184.
10. López E, Hernández JB, Solorio G, *et al*. Mathematical model of heat transfer to predict distribution of hardness through the Jominy bar. Revista de Metalurgia 2013; 49(2): 111–121.
11. Robert K, Saibel R, Ángel D. Formulation of a mathematical model to optimize the time of production in a plant extrusoras of pipes. Universidad, Ciencia y Tecnología 2012; 16(62): 33–41.

Thermal Science and Engineering (2021) Volume 4 Issue 1
doi:10.24294/tse.v4i1.1509

ORIGINAL RESEARCH ARTICLE

Thermodynamic stability diagram of the copper/water/amylxanthate flotation system

Beatriz Ramírez-Serrano*, Alexis Otero-Calvis, Alfredo Coello-Velázquez

Departamento de Metalurgia y Química. Instituto Superior Minero Metalúrgico, Holguín, Cuba. E-mail: bramirez@ismm.edu.cu

ABSTRACT

The purpose of this work was to obtain the thermodynamic stability diagram that characterizes the copper/water/amylxanthate flotation system, as part of the theoretical foundation necessary for the analysis of the copper ion flotation process with the flotation collector reagent potassium amylxanthate. From the system of fundamental chemical reactions and with the help of the Medusa software, the Eh-pH diagram was obtained, in which the stability zones of the different chemical species are defined and it is established that in the pH range from 4 to 13, the xanthogenic species of copper(I) and (II) coexist, whose ratio decreases with the increase of pH.

Keywords: Eh-pH Diagram; Xanthate; Copper Amyloxanthate; Copper; Ionic Flotation

ARTICLE INFO

Received: 11 March 2021
Accepted: 26 March 2021
Available online: 3 April 2021

1. Introduction

O-alkyldithiocarbonate reagents, known as xanthates, are compounds of heteropolar molecular structure, with a non-polar carbon chain and a polar sulfhydryl (-SH) group[1,2]. They are used as collectors in the flotation of sulfide minerals[3,4], mainly ethylxanthate[5-7], but their high chemical reactivity with heavy metals[2,8] stimulates their use in the treatment of waste solutions.

The results achieved with the application of this technique depend primarily on the pH of the medium. For example, in ionic dissolved air flotation of copper(II), zinc and arsenic(V) ions from synthetic solutions of individual ions and mixtures, sodium ethylxanthate and diethylxanthate are used as collectors[9,10]. Copper removal in the pH range between 2.5 and 5.5 is not affected but requires a 10 % excess of collector reagent. These works show satisfactory results. However, for pH below 4.7, partial decomposition of ethylxanthate is verified[8,11-13], and the effect on process efficiency is not mentioned. The use of sodium diethylxanthate as a collector, in spite of exhibiting similar properties and showing good results in the collection of copper and zinc, is limited by the cost of obtaining it[14].

Lazaridis *et al.*[15] report the application of the same ethylxanthate flotation technique on copper, iron and nickel systems independently and in their mixtures. The results showed that nickel remains in solution for acidic conditions, while copper and iron species float together and gradually increase their recovery until reaching maximum values from pH 6. If the pH of the system is equal to 2, the recovery values are associated with the initial copper and iron species float together and gradually increase their recovery until reaching maximum values from

pH 6. If the pH of the system is equal to 2, the recovery values are associated with the initial copper concentration; if its magnitude is low, copper recovery is reduced to 50% and iron to 25%, otherwise, about 80% is removed. It is possible that the result is associated with the decomposition of ethylxanthate; its half-life at pH 2.5 is 120 s[16], which coincides with the results achieved during ionic flotation of copper from mine wastewater[17], according to the conditions established by Stalidis *et al.*[9] involving high acidity. Favorable results are obtained only when twice the stoichiometric amount of ethylxanthate is used.

The works[9,15] on the separation of copper ions with ethylxanthate by flotation show a contradiction regarding the pH value at which optimum recovery values are reached. Stalidis *et al.*[9] stated that this result is achieved under acidic conditions, where the process is efficient and independent of pH, while Lazaridis *et al.*[15] state that it is only possible to achieve similar results for pH above 6. This indicates that it is necessary to accurately determine the stable zone according to the pH value of copper ions captured by xanthomonas in the flotation process.

The thermodynamic stability diagrams, as a function of pH, are an essential tool in the theoretical analysis of the interactions of a given system. In the case of the copper/sulfur/water/ethylxanthate system in the construction of the Eh-Ph diagram[18,19], copper(I) ethylxanthate was considered to be the initial product of the oxidation of ethylxanthate with calcocite. However, it has been reported[20] that such a diagram does not adequately predict the observed flotation behavior, because the limiting value of flotation potential is lower than the expected value in the diagram.

According to Woods *et al.*[20], this discrepancy can be explained by the fact that under these conditions, the formation of chemisorption species requires a lower potential than that required for the formation of copper(I) ethylxanthate. Such species were included by these authors in the construction of new diagrams in the copper/water/ethylxanthate and chalcocite/water/ethylxanthate systems. The predictions made in these diagrams are in correspondence with the critical potential and the upper limit of pH value for the flotation of pyrrhotite, which is related to the upper limit of stability of copper(I) ethylxanthate, determined in both systems by the oxidation of the copper(I) complex to copper(II) oxide and dixanthate.

Although these diagrams are applicable to copper ore flotation, the copper(II) ethylxanthate phase is not considered. It is suggested that there is no evidence that it is a stable phase. However, the half-life of the xanthogenated copper(II) species is known to be 6 h[21], if obtained from amyloxanthate.

Although some works report that the decomposition of the ethylxanthate species in aqueous media occurs in several stages[8,11,22-24], this mechanism is not well known. Proof of this is that the pH ranges of the stability zones for the reported species do not coincide[25]. Evidence also shows that the length of the carbon chain of the collectors causes changes in this zone and in the kinetics of their decomposition[26].

With the elements provided it is not possible to predict the reproducibility of the reported diagrams for xanthates that differ in carbon chain length. The reported Eh-pH diagrams do not accurately describe the copper/water/amylxanthate system under study in the present investigation. Therefore, it is necessary to establish the diagram for this system, which should give a more accurate answer to the behavior of copper species during flotation treatment with potassium amyloxanthate of solutions carrying this species, with respect to the system reported by Hepel and Pomianowski[27] for ethylxanthate.

The definition of the stability zone, both of the amyloxanthate ion and of the complexes formed as a function of pH, as well as the reaction system defined to obtain the diagram is of vital importance.

2. Materials and methods

2.1 Experimental procedure

2.1.1 Definition of the system of chemical reactions for the construction of the Eh-pH diagram

The system of equilibrium chemical reactions and reduction potential equations used in the con-

struction of the thermodynamic stability diagram of the copper/water/amylxanthate system is shown in **Table 1**.

Table 1. Chemical reactions and equations of the reduction potential

NO.	System reactions $Cu/H_2O/C_5H_{11}OCS_2^-$	Equations of reduction potential and pH
1	$HAmX(ac) \rightleftharpoons AmX^-(ac) + H^+(ac)$	$pH = 1.72 + log\left(\frac{AmX^-}{HAmX}\right)$
2	$(Am)X_2(ac) + 2e^- \rightleftharpoons 2AmX^-(ac)$	$E = -0.077 - 0.059\, log(AmX^-)$
3	$1/2(AmX)_2(ac) + e^- + H^+(ac) \rightleftharpoons HAmX(ac)$	$E = 0.179 - 0{,}059pH$
4	$Cu^{+2}(ac) + H_2O \rightleftharpoons CuO(s) + 2H^+(ac)$	$pH = 3.83 - log(Cu^{2+})$
5	$Cu^{+2}(ac) + e^- \rightleftharpoons Cu^+(ac)$	$E = 0.168 - 0.059\, log\left(\frac{Cu^+}{Cu^{+2}}\right)$
6	$CuO(s) + 2H^+(ac) + 2e^- \rightleftharpoons Cu(s) + H_2O$	$E = 0.564 - 0.059pH$
7	$CuAmX(s) + e^- \rightleftharpoons Cu(s) + AmX(ac)$	$E = -0.538 - 0.059\, log(AmX^-)$
8	$CuAmX(s) + e^- + H^+(ac) \rightleftharpoons Cu(s) + HAmX(ac)$	$E = -0.189 - 0.059pH$
9	$1/_2Cu_2O(s) + H^+(ac) + e^- \rightleftharpoons Cu(s) + 1/_2H_2O$	$E = 0.46 - 0.059pH$
10	$1/_2Cu_2O(s) + AmX^-(ac) + H^+(ac) \rightleftharpoons CuAmX(s) + 1/_2H_2O$	$pH = 16.88 + log(AmX^-)$
11	$1/_2Cu_2O(s) + 1/_2H_2O \rightleftharpoons CuO(s) + H^+(ac) + e^-$	$E = 0.66 - 0.059pH$
12	$Cu_2(AmX)_2(ac) + e^- \rightleftharpoons CuAmX(s) + AmX^-(ac)$	$E = -0.027 - 0.059\, log(AmX^-)$
13	$(AmX)_2(ac) + Cu^{+2}(ac) + 2e^- \rightleftharpoons Cu(AmX)_2(ac)$	$E = 0.543 - \frac{0.059}{2} log\left(\frac{Cu(AmX)_2}{(Cu^{+2})(AmX)_2}\right)$
14	$Cu(AmX)_2(ac) + e^- + H^+(ac) \rightleftharpoons CuAmX(ac) + HAmX(ac)$	$E = 0.075 - 0.059\, log\left(\frac{HAmX}{Cu(AmX)_2}\right) - 0.059pH$
15	$CuO(s) + AmX^-(ac) + e^- + 2H^+(ac) \rightleftharpoons CuAmX(s) + H_2O$	$E = 1.66 - 0.059\, log(AmX^-) - 0.059pH$
16	$CuO(s) + 1/_2(AmX)_2(ac) + 2e^- + 2H^+(ac) \rightleftharpoons CuAmX(s) + H_2O$	$E = 0.795 + \frac{0.059}{2} log(AmX)_2 - 0.059pH$
17	$CuO(s) + (AmX)_2(ac) + 2H^+(ac) + 2e^- \rightleftharpoons Cu(AmX)_2(ac) + H_2O$	$E = 0.77 - \frac{0.059}{2} log\left(\frac{Cu(AmX)_2}{AmX}\right)_2 - 0.059pH$
18	$Cu(ac) + H_2O \rightleftharpoons CuO(s) + 2H^+(ac) + e^-$	$E = 0.88 - 0.118pH$

Amx-amyloxanthate($C_5H_{11}OCS_2$)$^-$ **(Amx)$_2$-amyldiaxanthate($C_5H_{11}OCS_2$)$_2$**

The construction of the diagram was carried out with the help of the Medusa software[28] of the Department of Inorganic Chemistry of the Royal Institute of Technology, Great Britain, which contains a database from log K to 298 K; the software allows the modification and creation of diagrams from supplied data.

The potential value $1.59 \cdot 10^{-2}$ eV[3] for the $(Amx)_2/Amx^-$(Am-amil; X-xantato) pair was used in the construction of the diagram. The equilibrium constant value for the copper(II) amyloxanthate complex formation reaction is $3.7 \cdot 10^9$[21]; for the copper(I) amyloxanthate complex formation reaction the experimental value 0.3467 was used[29].

3. Results and discussion

In the analysis of xanthogenic systems, the decomposition of ethylxanthate in aqueous media must be considered; for this purpose, six stages have been proposed[8,25,30].

Stage 1: Hydrolysis of xanthate ion and formation of xanthic acid

$$K^+(ac) + ROCS_2^-(ac) + H_2O \underset{k_2}{\overset{k_1}{\rightleftharpoons}} K^+(ac) + OH^-(ac) + ROCS_2H(ac) \quad (1)$$

Where R represents the carbon chain.

Stage 2: Decomposition of xanthic acid to alcohol and carbon disulfide

$$ROCS_2H(ac) \overset{k_3}{\rightleftharpoons} ROH(ac) + CS_2(ac) \quad (2)$$

Where k_1, k_2 and k_3 are the velocity constants.

Both reaction equations are verified in acid medium. Iwasaki and Cooke[11] reported that the ethylxanthate ion and ethylxanthic acid are in equilibrium in a pH range from 0.10 to 4.71, corresponding to the value of the dissociation constant of ethylxanthic acid, which is considered a moderately weak acid (pKa = 1.6)[31].

Stage 3: Hydrolytic decomposition of xanthate ion

$$6ROCS_2^-(ac) + 3H_2O \longrightarrow CO_3^{-2}(ac) + 3CS_2(ac) + 2CS_3^{-2}(ac) + 6ROH(ac) \quad (3)$$

This stage can occur in neutral and alkaline media, however, some authors consider that the reaction occurs only when pH > 13[1,5,12,25]. According to Pomianowsky and Leja[23], the decomposition of trithiocarbonate into carbon disulfide and sulfur, CS_2 and S^{2-}, can occur in parallel.

Stage 4: Oxidation to dixanthate

$$2ROCS_2^-(ac) \longrightarrow (ROCS_2)_2(ac) + 2e^- \quad (4)$$

Zohir *et al.*[32] propose that the above reaction equation is independent of the reduction potential, unlike the mechanism that takes place in the presence of dissolved oxygen in the aqueous medium:

4.a)

$$2ROCS_2^-(ac) + 1/_2O_2(ac) + H_2O \rightarrow (ROCS_2)_2(ac) + 2OH^-(ac) \quad (5)$$

The magnitude of the reaction corresponding to stage **4.a** is very small and reaches equilibrium in neutral medium after oxidation of 5%–10%; its extent depends on the pH of the medium. Its development is more significant with increasing hydrocarbon chain length[8]. Correspondingly, the value of the oxidation potential also increases; it is 0.04 eV and -0.159 eV for methyldixanthate and n-amyldixanthate respectively[33]. The above information indicates that the behavior of xanthates in aqueous media, according to the number of carbon atoms in the chain, may differ as a function of the pH conditions of the medium. Similarly, the values of the molar absorptivity coefficient are modified[34].

The oxidation reactions to dixanthate have been considered irreversible and dixanthate unreactive, but studies by Pomianowsky and Leja[23] showed that this species reacts under alkaline conditions and gives rise to the ethylxanthate ion and carbon disulfide[12] according to the following reaction equation.

$$2(EtX)_2(ac) + 2OH^-(ac) + 2K^+(ac) \longrightarrow EtX^-(ac) + EtOH(ac) + CS_2(ac) + 2K^+(ac) + O_2(g) \quad (6)$$

The development of the last two stages needs specific conditions to be verified[24].

Stage 5: Oxidation to monothiocarbonate

$$ROCS_2^-(ac) + 1/_2O_2(g) \rightleftharpoons ROCOS(ac) + S(s) \quad (7)$$

According to Harris and Filkenstein[24], the formation of monothiocarbonate requires the participation of sulfide where the reactants are previously adsorbed; the sulfide acts as a catalyst.

Stage 6: Oxidation to perxanthate

$$ROCS_2^-(ac) + H_2O_2(ac) \rightleftharpoons ROCS_2O(ac) + H_2O \quad (8)$$

In the case of perxanthate, its presence has been recorded under specific conditions of alkalinity and high degree of oxidation[12,14].

Although the steps have been generalized, there is a contradiction between the pH range of ethylxanthate decomposition in acidic media[11] and its application results in flotation at similar pH values[9,17]. Moreover, the effect caused by increasing the number of carbon atoms on the pH range in which such transformations manifest themselves has not been tested. Although it is well known that the stability of xanthate has been improved, and the decomposition kinetics has slowed down with the increase of carbon chain, these aspects have a significant impact during the interaction between xan-

thate species and metal ions present in a solution.

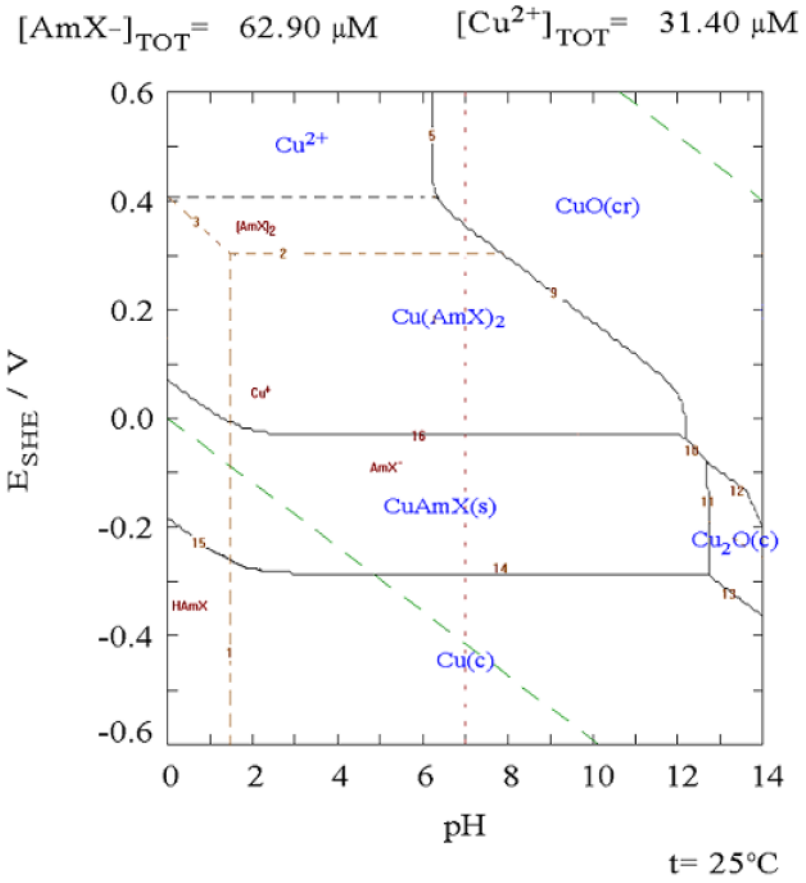

Figure 1. Thermodynamic stability diagram of the copper/water/amylxanthate system.

3.1 Potential-pH diagram of the copper/water/amyloxanthate system

Figure 1 shows the thermodynamic stability diagram for the copper/water/amylxanthate system.

It is observed that the stability zones of the xanthogenic copper species coexist practically up to pH equal to 13 units. As can be seen, the conditions of the potential of the medium play a decisive role in the predominance of one of the species during the flotation process. In a comparative analysis of this diagram and the one reported by Hepel and Pomianowski[27] for potassium ethylxanthate under the same conditions, the variation in the stability zones of the compounds with amyloxanthate, with respect to the one formed with ethylxanthate, was verified, mainly due to the reduction of the potential value at which they are stable.

As for the pH value, no significant changes are shown in the stability zones of the different species. Compared with short chain xanthates, The difference in stability of amyloxanthate is based on the speed of decomposition, and its kinetics is slow[26]. This characteristic favors the use of amyloxanthate with respect to ethylxanthate in processes where greater stability of its complexes is required for their separation by flotation.

4. Conclusions

The thermodynamic stability diagram for the copper/water/amylxanthate system is established. The analysis showed that the xanthogenic species of copper(I) and (II) coexist in the pH range of 4 to 13, and their ratio decreases with the increase of pH.

Conflict of interest

The authors declared no conflict of interest.

References

1. Somasundaran P, Moudgil BM. Reagents in minerals technology. Florida: CRC Press; 1988.
2. Roy KM. Xanthates. In: Ullmann's encyclopedia of industrial chemistry.
3. Crozier RD. Flotation: Theory, reagents and ore

testing. 1st ed. Oxford: Pergamon Press; 1992.
4. Fuerstenau DW. Advances in flotation technology. SME: Littleton; 1999. p. 3–21.
5. Dudenkov S, Shubov L, Glazunov L. Fundamentos de la teoría y la práctica de empleo de reactivos de flotación (Spanish) [Theoretical and practical basis for the use of flotation reagents]. Moscow: Mir Publishers; 1980.
6. Harris PJ. Reagents in mineral technology. New York: Marcel Dekker; 1988.
7. Abramov AA, Forssberg KSE. Chemistry and optimal conditions for copper minerals flotation: Theory and practice. Mineral Processing and Extractive Metallurgy Review 2005; 26: 77–143.
8. Rao SR. Xanthates and related compounds. 1st ed. New York: Marcel Dekker; 1971. p. 1–504.
9. Stalidis GA, Matis KA, Lazaridis NK. Selective separation of cu, zn, and as from solution by flotation techniques. Separation Science and Technology 1989; 24(1): 97–109.
10. Matis KA, Mavros P. Recovery of metals by ion flotation from dilute aqueous solutions. Separation and Purification Methods 1991; 20: 1–48.
11. Iwasaki I, Cooke SRB. The decomposition of xanthate in acid solution. Journal of the American Chemical Society 1958; 80: 285–288.
12. Tipman RN, Leja J. Reactivity of xanthate and dixanthogen in aqueous solution of different pH. Colloid and Polymer Science 1975; 253: 4–10.
13. Sun Z, Forsling W. The degradation kinetics of ethyl-xanthate as a function of pH in aqueous solution. Minerals Engineering 1997; 10(4): 389–400.
14. Leja J. Surface chemistry of froth flotation. New York: Plenum Press; 1982. p. 1228.
15. Lazaridis NK, Matis KA, Stalidis GA, *et al*. Dissolved-air flotation of metal ions. Separation Science and Technology 1992; 27(13): 1743–1758.
16. Kakovsky I. Physicochemical properties of some flotation reagent and their salts with ions of heave iron-ferrous metals. Proceedings of the Second International Congress of Surface Activity; London. 1957. p. 225–237.
17. Lazaridis NK, Peleka EN, Karapantsios ThD, *et al*. Copper removal from effluents by various separation techniques. Hydrometallurgy 2004; 74(1–2): 149–156.
18. Basilio C, Pritzker MD, Yoon RH. Thermodinamics, electrochemistry and flotation of de calcocite-potassium ethyl xanthate system. 114th AIME Annual Meeting; 1985 Feb 24–27; New York. 1985. p. 85–86.
19. Young CA. Nonstoichiometry of chalcocite in water-xanthate systems [MSc thesis]. Virginia Polytechnic Institute and State University; 1987. p. 296.
20. Woods R, Young CA, Yoon RH. Ethyl xanthate chemisorption isotherms and Eh-pH diagrams for the copper/water/xanthate and chalcocite/water/xanthate systems. International Journal of Mineral Processing 1990; 30: 17–33.
21. Joly HA, Majerus R, Westaway KC. The effect of diethylenetriamine on the formation of Cu^{2+}, Ni^{2+}, and Fe^{3+} amyl xanthate ion complexes. Minerals Engineering 2004; 17: 1023–1036.
22. Klauditz W. The ripening of viscose. Tech-Wise; 1939. p. 251–259.
23. Pomianowsky A, Leja J. Spectrophotometric study of xanthate and dixanthogen solutions. Canadian Journal Chemistry 1963; 41: 2219–2230
24. Harris PJ, Filkenstein NP. Interactions between sulphide minerals and xanthates, I. The formation of monothiocarbonate at galena and pyrite surfaces. International Journal of Mineral Processing 1975; 2(1): 77–100.
25. Obregón H. Xantatos en sistemas de flotación (Spanish) [Xanthates in flotation systems]. Reacciones Fenómenos y Mecanismos 1990; 5.
26. Donato P, Cases JM, Kongolo M, *et al*. Stability of the amylxanthate ion as a function of pH: Modelling and comparison with the ethylxanthate ion. International Journal of Mineral Processing 1989; 25: 1–16.
27. Hepel T, Pomianowski A. Diagrams of electrochemical equilibria of the system copper-potassium ethylxanthate-water at 25 ºC. International Journal of Mineral Processing 1977; 4: 245–361.
28. Puigdomenech I. Software equilibrio químico (Spanish) [Chemical equilibrium software]. Royal Institute of Technology 2004.
29. Ramírez Serrano B. Remoción por flotación iónica de iones cobre con (Spanish) [Removal by ionic flotation of copper ions with potassium amylxanthate] [PhD thesis]. Moa: Instituto Superior Minero Metalúrgico; 2011. p. 120.
30. Bulatovic SM. Handbook of flotation reagents. Chemistry, theory and practice: Flotation of sulfide ores. Amsterdam: Elsevier; 2007. p. 443.
31. AGPS. Sodium ethyl xanthate. 1995. p. 1–64.
32. Zohir N, Mustapha B, Abd-Elbaki D. Synthesis and structural characterization of xanthate (KEX) in sight of their utilization in the processe s of sulphides flotation. Journal of Minerals and Materials Characterization and Engineering 2009; 8(6): 469–477.
33. Jones MH, Woodcock JT. Dixanthogen determination in flotation liquors by solvent extraction and ultraviolet spectrometry. Analytical Chemistry 1986; 58: 588–591.
34. Jones MH, Woodcock JT. Ultraviolet spectrometry of flotation reagents with special reference to the determination of xanthate in flotation liquors. London: Chameleon Press; 1973. p. 110.

Thermal Science and Engineering (2021) Volume 4 Issue 1
doi:10.24294/tse.v4i1.1510

ORIGINAL RESEARCH ARTICLE

Thermodynamic study on lead leaching from sodium citrate

Lina Constanza Villa[1], Wilmer Saldarriaga Agudelo[2], Néstor Ricardo Rojas[3*]

[1] *Maestría en Ingeniería-Materiales y Procesos. Universidad Nacional de Colombia, Sede Medellín, Colombia.*

[2] *Doctorado en ciencias químicas - Universidad del Valle. Universidad Nacional de Colombia, Sede Medellín, Colombia.*

[3] *Doctorado en ciencia y tecnología de los materiales. Universidad Nacional de Colombia, Sede Medellín, Colombia. E-mail: nrrojasr@unal.edu.co*

ABSTRACT

Lead-acid batteries account for 60% of the world's electrical energy storage batteries. About 50% of global lead consumption comes from recycled and reused materials. Currently, pyrometallurgical methods account for more than 90% of lead recovery technology; however, these processes are criticized due to sulfur dioxide emissions from the decomposition of lead sulfate at elevated temperatures, in addition to particulate emissions. Lead recovery by recycling batteries by hydrometallurgical processes has been investigated as an alternative to pyrometallurgical processes. In the present work, a thermodynamic analysis of lead leaching with sodium citrate was performed. The thermodynamic analysis was based on the study of three stability diagrams constructed with Medusa® software. Leaching tests were carried out to get to know the system, corroborate the thermodynamic analysis performed, and study the behavior of the system. The results obtained show that it is possible to extract 100% lead with a leaching agent concentration of 0.25 M, a 1:1 solid-liquid ratio, and 25 ℃.

Keywords: Sodium Citrate; Lead Hydrometallurgy; Recycling of Materials; Thermodynamics

ARTICLE INFO

Received: 12 March 2021
Accepted: 10 April 2021
Available online: 16 April 2021

1. Introduction

Lead-acid batteries account for about 60% of batteries sold worldwide. About 50% of lead consumption worldwide is derived from recycled and reused materials. One of the advantages of lead recovery from industrial waste is lower energy consumption, as it uses only 35% to 40% of the energy that would be used to produce lead from mineral ores[1].

The most widely used method in the lead recycling industry uses pyrometallurgical processes, which represent more than 90% of the lead recovery technology. Although these methods are fast, they are also potentially polluting, mainly due to the emission of sulfur dioxide when decomposing lead sulfate and the emission of particulate matter[2]. It directly influences the deterioration of the ozone layer and is critical in the generation of acid rain, causing problems for the environment and human health[1]. Due to the above, the idea of developing a technical alternative to mitigate these environmental impacts arises.

In recent decades, in order to reduce secondary contamination from vapors and dust caused by the pyrometallurgical lead recovery process, lead recovery methods such as hydrometallurgical processes have been proposed[3]. However, these latter processes should be further investigated because they present primary problems such as inefficient desulfurization in an aqueous solution and low solubility of lead compounds

in organic solvents[2].

The design of a hydrometallurgical process for lead must take into account the appropriate conditions for desulfurization, leaching and precipitation of lead and/or possible lead compounds, which is essential for the efficiency of the process. Research on the subject has found several advantages compared to traditional processes, such as no emission of sulfur dioxide gas and lead particulate matter, as well as lower energy consumption and recovery of ultrafine lead[4].

In this paper, a thermodynamic analysis of the leaching agent sodium citrate ($Na_3C_6H_5O_7$-$2H_2O$)[5,6] was developed for the extraction of lead obtained from recycled car batteries. The work was carried out through the use of mechanical techniques for the processing of materials, in conjunction with chemical processes implemented in hydrometallurgy. These results, it is expected to contribute to knowledge for the use of the metal recycling industry in our country.

2. Materials and methods

Automotive batteries were collected, based on a commercial analysis, and were selected from the brands that are most commonly in the market. The sulfuric acid contained in the battery was neutralized with sodium carbonate. Subsequently, the internal cells of the battery were extracted to dry them at room temperature. A total of 50 g were taken from each of the electrodes, 100 g in total as an initial sample. The sample was mechanically treated through a Braun Direct Driven Pulverizer UD32, with a speed of 400 rpm. It allowed a homogeneous size reduction. However, to achieve the desired particle size, the material was macerated and then quartered, obtaining a particle size passing mesh N°200 (75 microns) with a sieve of the ASTM-E-11 series. A Varian Spectra AA 220FS atomic absorption spectrometer was used to determine the lead content in the different stages of the investigation. For the acid digestion of the initial sample, prepare a 100 mL solution (aqua regia) to maintain a 1:3 ratio of nitric acid to hydrochloric acid (25 mL HNO_3 and 75 mL HCL). In the solution, 0.121 g of the initial sample already prepared and sieved was dissolved. The solution was stirred at a speed of 300 rpm at a temperature of 350 °C until the solution volume reduces 50 mL. The next step was the cooling of the solution only with agitation and then filtering under vacuum and gauging in a 100 mL flask with the addition of deionized water. The morphological and chemical characterization of the working material was carried out with Phenom Pro X equipment of the Phenom-World brand, which integrates an energy dispersive spectroscopy (EDS) that allows identifying the elements and the chemical composition of the sample. To determine the predominant phases in the sample and the chemical composition of the solid lead-acid battery material, it use the D_8 Advance X-ray diffraction equipment. The thermodynamic analysis was carried out using Medusa® software. According to the characterization performed on the material, the following conditions were set in the program[5], 0.04 M of lead (Pb^{2+}), 0.01 M of sulfate ion, 1 M concentration for the leaching agent, and room temperature (25 °C). The choice of sodium citrate as a leaching agent is based on its low cost and low environmental impact.

The leaching agent complexes lead sulfate ($PbSO_4$) and lead oxide (PbO), in which lead is found as Pb^{2+}. The other existing species such as lead dioxide (PbO_2) and metallic lead Pb^0 do not complex with the leaching agent, so it is necessary to first add a reducing agent which was hydrazine (N_2H_4)[7], which reduces the Pb^{4+} of PbO_2 to Pb^{2+} and finally an oxidizing agent, hydrogen peroxide (H_2O_2), which oxidizes Pb^0 to an oxidation state of Pb^{2+}, in order to form complexes with sodium citrate.

Finally, leaching tests were carried out to learn about the system, corroborate the thermodynamic analysis performed. The working conditions established were as follows: solid-liquid ratio 1:1, 10:1 and 30:1; concentration of the leaching agent: 0.25 M, 0.5 M and 1 M; pH = 7; solution volume 0.1 L; temperature 25 °C; agitation 300 rpm; leaching time 3 hours, reducing agent-oxidizing agent N_2H_4-H_2O_2.

3. Analysis of results

Based on the acid digestion performed and the result of the atomic absorption spectrophotometry, it was found that the lead content in the analyzed battery is 85.6%, therefore, the metal concentration in 1 g of working sample is 0.04 *M Pb* (see calculations

in **Annex 1**).

Scanning electron microscopy (SEM) analysis showed that the particle size of the working material is less than 75 μm, as observed in **Figure 1**, and that this material is composed of sulfates and lead oxides, based on the elements found by EDS in the sample and observed in **Figure 2**.

In the X-ray diffractogram (**Figure 3**) it was observed that the predominant phase is lead sulfate ($PbSO_4$) with a concentration of approximately 50.9%, followed by lead dioxide (PbO_2) with a concentration of approximately 36.4%. Metallic lead (Pb) is found at a concentration of 6.1%, and finally lead oxide (PbO) was determined at a concentration of 2.4%.

To perform the thermodynamic analysis, three diagrams were constructed: pourbaix diagrams for the Pb citrate-S-H_2O system, species fraction of the Pb-SO_4-sodium citrate system, and solubility of lead and sulfate ion in the presence of sodium citrate, which is shown below.

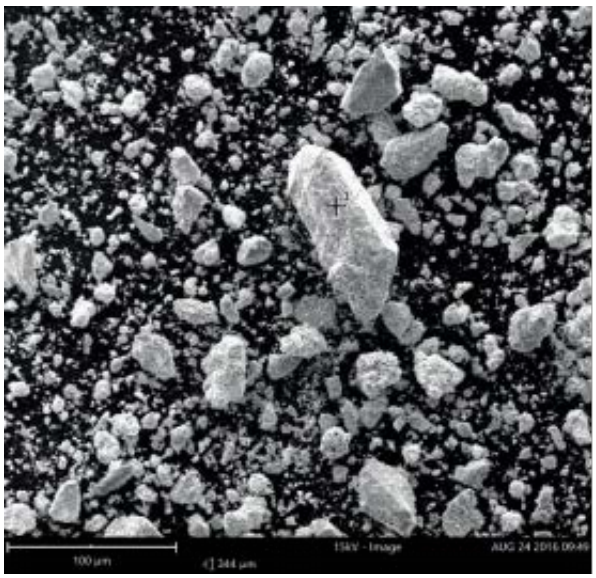

Figure 1. SEM image of the working sample.

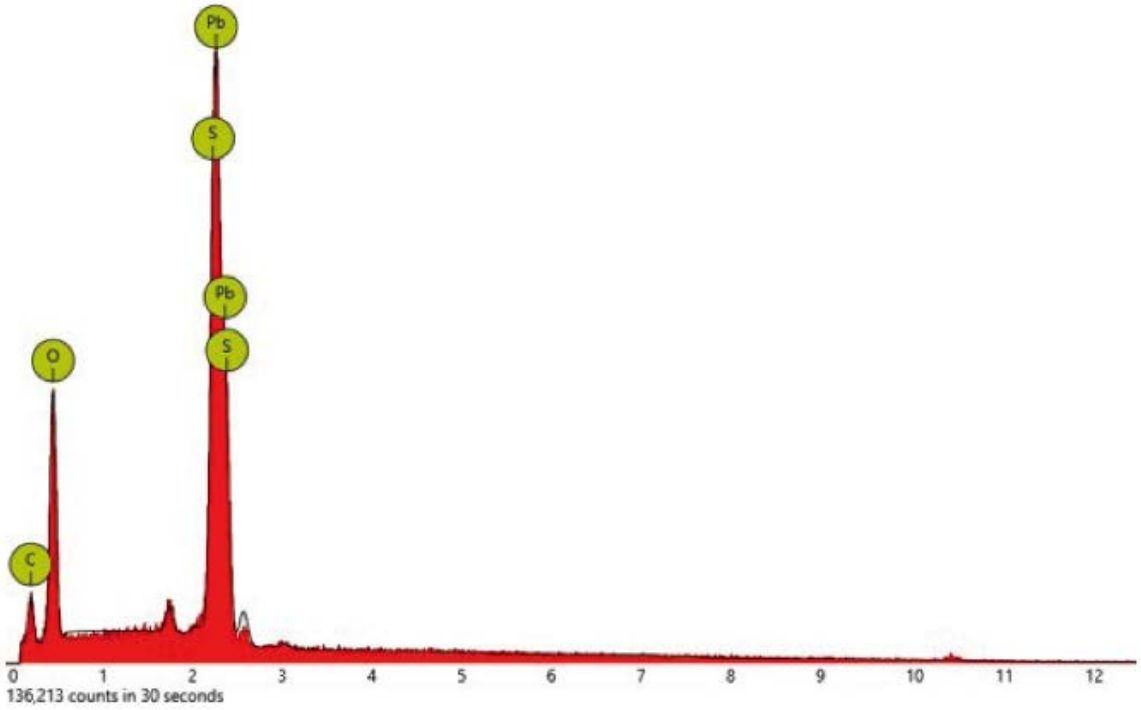

Figure 2. EDS micrographic analysis of the working sample.

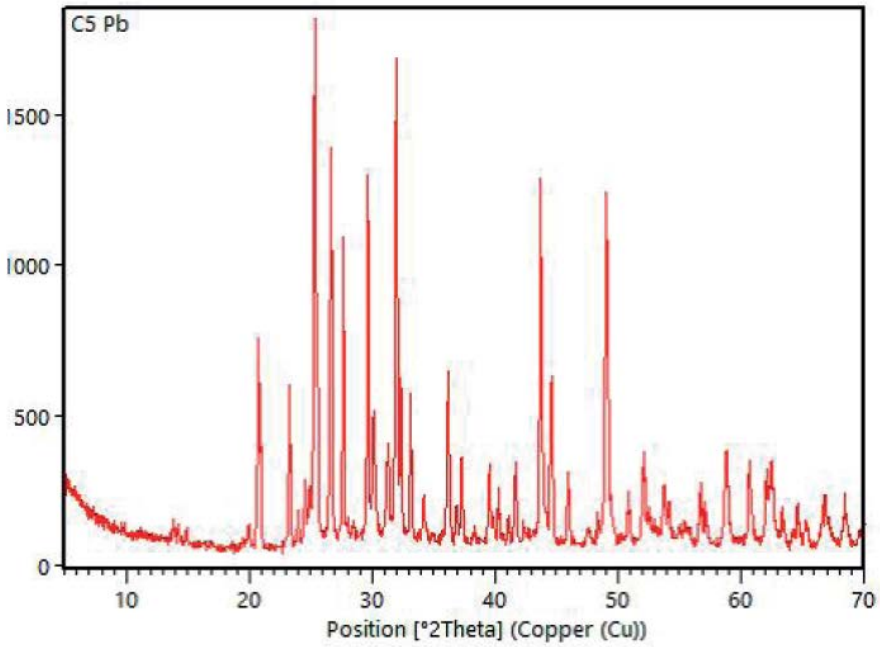

Figure 3. X-ray diffractogram of the sample.

Figure 4 shows the Pourbaix diagram of the Pb-Citrate-S-H_2O system at 25 °C, in which it is observed that within the range of water stability and pH between 5 and 8.5 lead forms two kinds of soluble complexes with citrate $Pb(cit)^-$ and $pb(cit)_2^{4-}$. At pH values lower than 5, precipitation is determined first of a Pb-citrate complex, and then of sulfate $PbSO_4$. At pH higher than 8.5, precipitation of hydroxide $Pb(OH)_2$ is established. For the whole pH working range, PBS sulfide can be obtained from both soluble and insoluble species with the variation of the electric potential.

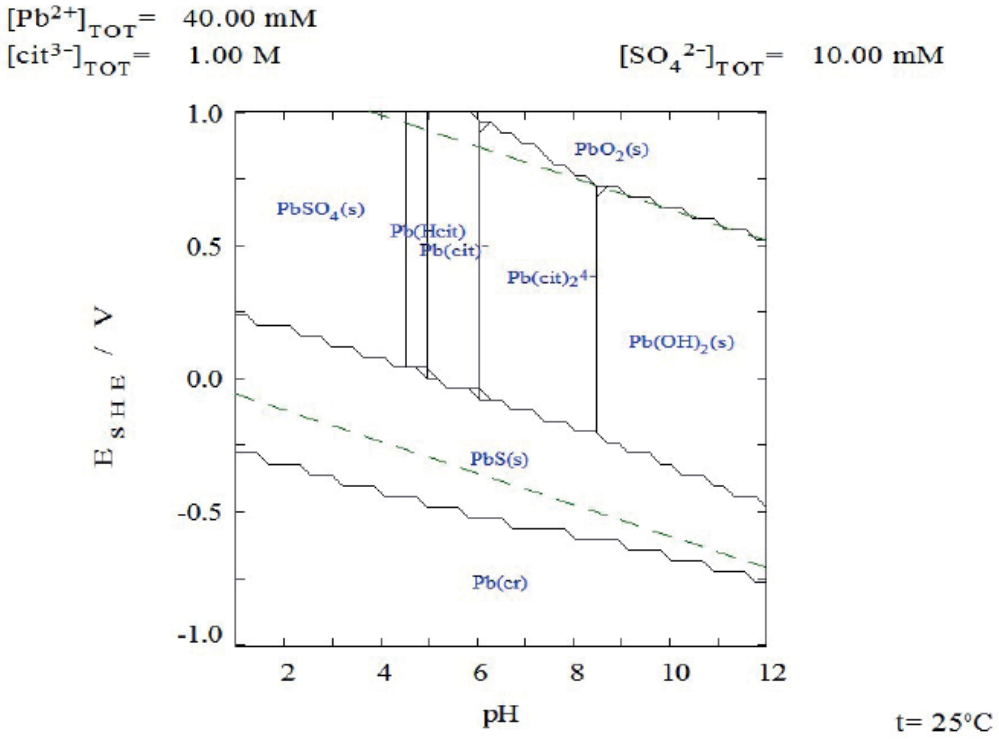

Figure 4. Pourbaix diagram for the Pb-citrate-S-H_2O system in the presence of sodium citrate. Medusa® Software.

Figure 5 shows the species fraction diagram; and concerning the two complexes also found in the Pourbaix diagram, a relative presence for $Pb(cit)_2^{4-}$ of 60% at pH 7.5 is determined, while for the $Pb(cit)^-$ species its presence is only 30% at pH 5.5. The other species that appear in the solution could be obtained by adding hydrazine as a reducing agent and oxidizing with hydrogen peroxide. However, their presence in the system would be less than 30%. The solubility diagram in **Figure 6** shows that Pb is soluble in citrate from acid pH up to pH 8, where its presence decreases. While the sulfate ion is soluble at basic pH up to pH 5, pH from which its solubility decreases.

Based on the above diagrams for a leaching pH range between 5 and 8, it is theoretically possible to leach lead with sodium citrate in the presence of sulfur and obtain $Pb(cit)^-$ and $pb(cit)_2^{4-}$ at a temperature of 25 °C.

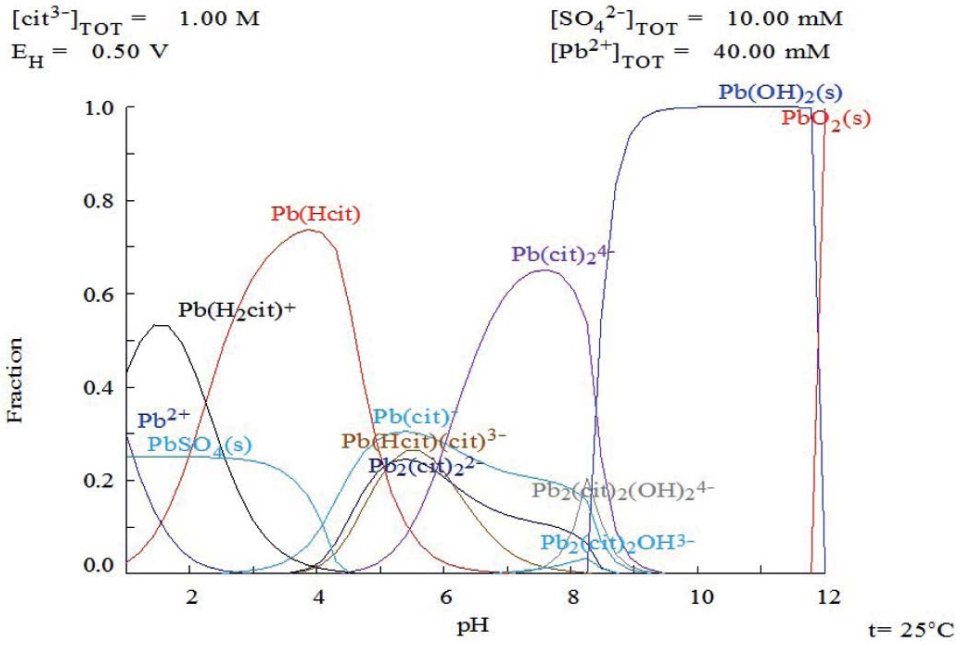

Figure 5. Species fraction plot of the Pb^{2+} system in the presence of sodium citrate. Medusa® software.

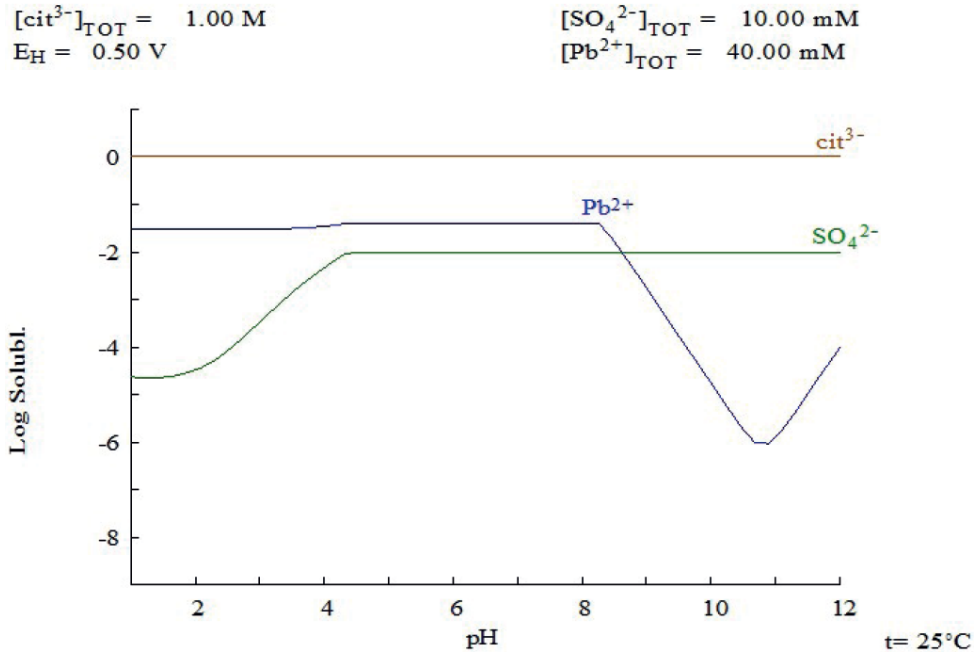

Figure 6. Pb^{2+} solubility diagram in sodium citrate. Medusa® software.

The following three graphs show the results of the sodium citrate leaching kinetic tests. **Figure 7** shows that for a low suspension with a 1:1 solid-liquid ratio and a low concentration of leaching agent (0.25 M), 100% metal extractions are obtained in 138 minutes of leaching. When the concentration of leaching agent increases, the extraction decreases to 80%, which is still an industrially attractive value. The above results indicate that the ionic activity is higher at low concentrations compared to the characteristics of a solution with high concentrations. If the consumption of sodium citrate dominates the hydrolytic reaction, the complex reaction can be weakened or slowed down. It would lead to an inhibitory effect on the behavior of the leaching agent[6,8].

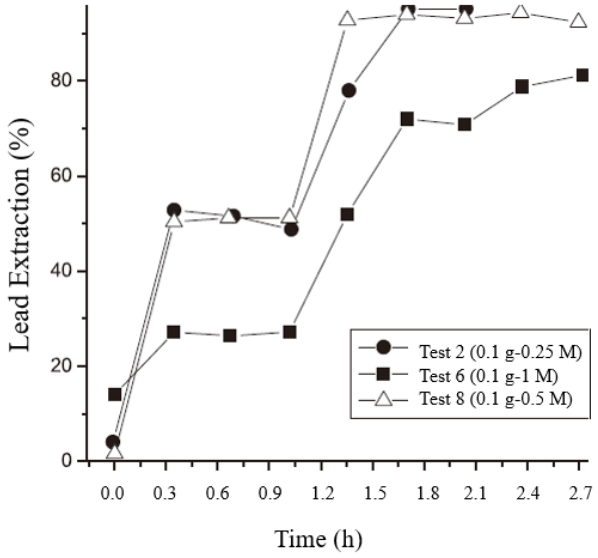

Figure 7. Lead extraction kinetics for a constant mass of 0.1 g in 0.1 L and citrate concentration 0.25, 0.5 and 1 M.

Figure 8 shows a decrease in metal extraction and a lower influence of the leaching agent concentration in the hydrometallurgical process; the highest extraction (90%) was obtained for a 10:1 solid-liquid ratio at 0.25 and 0.5 M citrate; while for a 1 M citrate concentration, 85% was obtained. It is determined that for these solid concentrations the concentration of the leaching agent is not very relevant. Finally, **Figure 9** shows the lowest metal extraction and no influence of the leaching agent concentration. All leachates with the highest 3:1 solid-liquid ratio were between 20 and 25% metal extraction, with less favorable conditions industrially. Low metal extractions at high suspended solids concentrations may again be due to an inhibitory effect on the behavior of the leaching agent; the controlling mechanism of the reaction may also play a role, it is possible that at low concentrations of leaching agent the process is controlled by mass transfer, however, at high concentrations, the mechanism is different[9].

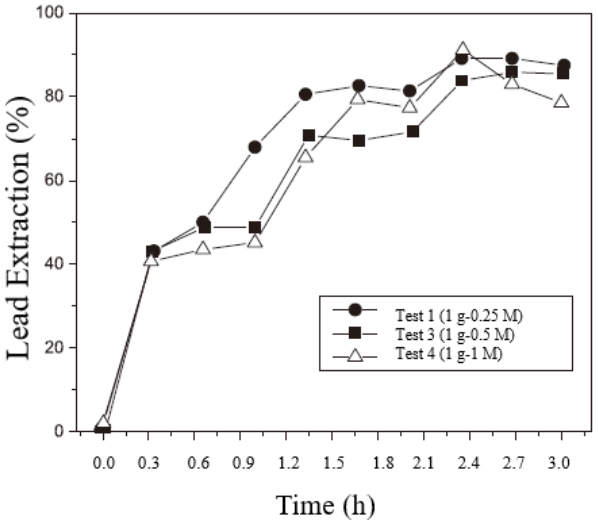

Figure 8. Lead extraction kinetics for a constant mass of 1 g in 0.1 L and citrate concentration 0.25, 0.5 and 1 M.

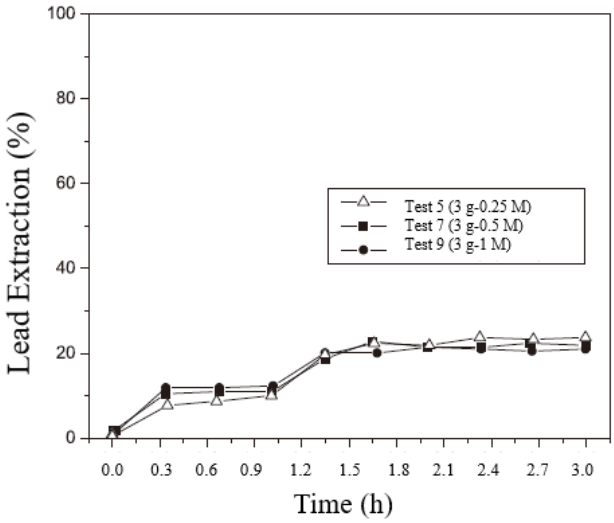

Figure 9. Lead extraction kinetics for a constant mass of 3 g in 0.1 L and citrate concentration 0.25, 0.5 and 1 M.

4. Conclusions

The stability diagrams analyzed show that it is thermodynamically possible to leach lead with sodium citrate to obtain $Pb(cit)^-$ and $Pb(cit)_2^{4-}$, at pH between 5 and 8 and temperature of 25 °C. Kinetic studies indicate recoveries of 100 and 90% for citrate concentrations of 0.25 and 0.5 M respectively, at 25 °C and a 1:1 solid-liquid ratio. A

hydrometallurgical process is technically possible as a real alternative for lead recycling from spent lead-acid batteries, because with this process, there are no sulfur dioxide or particulate emissions to the environment.

Conflict of interest

The authors declared no conflict of interest.

References

1. Smaniotto A, Antunes A, Filho I, *et al*. Qualitative lead extraction from recycled lead-acid batteries slag. Journal of Hazardous Materials 2009; 172(2–3): 1677–1680. doi: 10.1016/j.Jhazmat.2009.07.026.
2. Sonmez M, Kumar R. Leaching of waste battery paste components. Part 1: Lead citrate synthesis from PbO and PbO_2. Hydrometallurgy 2009; 95(1–2): 53–60. doi: 10.1016/j.Hydromet.2008.04.012.
3. Pan J, Zhang C, Sun Y, *et al*. A new process of lead recovery from waste lead-acid batteries by electrolysis of alkaline lead oxide solution. Electrochem Commun 2012; 19: 70–72. doi: 10.1016/j.elecom.2012.03.028.
4. Zhu X, Li L, Sun X, *et al*. Preparation of basic lead oxide from spent lead acid battery paste via chemical conversion. Hydrometallurgy 2012; 117–118: 24–31. doi: 10.1016/j.hydromet.2012.01.006.
5. Puigdomenech I. MEDUSA, HYDRA and INPUT-SED-PREDOM. Stockholm, Sweden: Royal Institute of Technology. 2004. Available from: https://sites.google.com/site/chemdiagr.
6. He D, Yang C, Wu Y, *et al*. $PbSO_4$ leaching in citric acid/sodium citrate solution and subsequent yielding lead citrate via controlled crystallization. Minerals 2017; 7: 93–103. doi: 10.3390/min7060093.
7. Zarate-Gutierrez R, Lapidus G. Anglesite ($PbSO_4$) leaching in citrate solutions. Hydrometallurgy 2014; 144–145: 124–128. doi: 10.1016/j.hydromet.2014.02.003.
8. Ajibola O, Jimoh BO. Agitation leaching recovery of lead and zinc from complex sulphide ore deposit using HF, HCL and H_2SO_4. Advances in Applied Science Research 2014; 5(3): 68–72. Available from: https://www.primescholars.com/articles/agitation-leaching-recovery-of-lead-and-zinc-from-complex-sulphideore-deposit-using-hf-hcl-and-h2so4.pdf.
9. Seidel A, Zimmels Y. Mechanism and kinetics of aluminum and iron leaching from coal fly ash by sulfuric acid. Chemical Engineering Science 1998; 5(22): 3835–3852. doi: 10.1016/S0009-2509(98)00201-2.

Appendix 1. Determination of lead concentration in the working sample.

Acid digestion of the initial sample: The result of the digestion performed to determine the lead content in the sample was 85.6 ppm for 0.1 g of head sample in 0.1 L of solution:

$$85.6 \text{ ppm} \times \frac{10 \text{ ml solution}}{1 \text{ ml sample}} = 856 \text{ ppm total digestion 0.1 L}$$

$$856 \text{ mg/L} \times 0.1 \text{ L} = 85.6 \text{ mg Pb}$$

$$\text{Quality} = 0.1 \text{ g} = 100 \text{ mg}$$

$$\%\text{Pb} = \frac{\text{mg digestion}}{\text{mg sample}} \times 100\% = \frac{85.6 \text{ mg Pb}}{100 \text{ mg sample}} \times 100\% = 85.6\% \text{ Pb}$$

The result of the atomic absorption spectrophotometry shows that the lead (Pb) content of the analyzed battery is 85.6%.

According to this result, the molar concentration of lead was determined:

$$1\ M \text{ Pb} = 207.2 \text{ g/L Pb}$$

$$856 \text{ mg Pb} \times \frac{1 \text{ g Pb}}{1000 \text{ mg Pb}} = 0.856 \text{ g Pb}$$

$$0.856 \text{ g Pb} \times \frac{1 \text{ mol Pb}}{207.2\ g \text{ Pb}} = 4.13 \times 10^{-3} \text{ mol Pb}$$

$$\text{Molar amount in 1 g sample} = \frac{4.13 \times 10^{-3} \text{ mol Pb}}{0.1 \text{ L}} = 0.04\ M \text{ Pb}$$

Thermal Science and Engineering (2021) Volume 4 Issue 1
doi:10.24294/tse.v4i1.1511

ORIGINAL RESEARCH ARTICLE

Determination of overall heat transfer coefficients comparing LMTD and ε-NTU methods

Andres Adrian Sánchez Escalona[1*], Ever Góngora Leyva[2]

[1] *Moa Nickel S.A.–"Pedro Sotto Alba", Moa, Holguín, Cuba. E-mail: aescalon@moanickel.com.cu*

[2] *Instituto Superior Minero Metalúrgico, Moa, Holguín, Cuba.*

ABSTRACT

Thermal energy transfer processes are important problems to be solved in the field of engineering. In this field, heat exchangers are one of the most used equipment in the industry. The present investigation was carried out in an operating hydrogen sulfide cooler system, with the objective of determining the overall heat transfer coefficients by two methods, applying the passive experimentation procedure. With the Logarithmic Mean Temperature Difference (LMTD) method, values ranging from 11.1 to 73.3 W/(m^2·K) were obtained, compared to 11.0 to 58.9 W/(m^2·K) when applying the Effectiveness-Number of Transfer Units (ε-NTU) method. Although the results obtained were similar, for the thermal evaluation of the chiller system studied, it was recommended to employ the LMTD approach, used by most researchers.

Keywords: Heat Exchanger; Hydrogen Sulfide; Overall Heat Transfer Coefficient; LMTD; ε-NTU

ARTICLE INFO

Received: 25 March 2021
Accepted: 29 April 2021
Available online: 18 May 2021

1. Introduction

Heat exchangers are present in most complex thermal systems and are the most widely used device for non-combustion heat transfer in industrial processes. They are used in chemical processing plants, steam generation, heating and air conditioning, food preparation, refrigeration, among other applications. Monitoring of their optimum operating parameters ensures process economy[1-3].

There are several criteria for evaluating the performance of heat exchangers. Of these, the behavior of the overall heat transfer coefficient over time is considered a reliable parameter to determine how quickly the conditions favoring heat exchange deteriorate[4,5]. Moreover, its prior calculation is necessary to determine the fouling factor and impact of depositions on the efficiency loss of the installation[6,7].

For the determination of global heat transfer coefficients from experimental data, the Logarithmic Mean Temperature Difference (LMTD) method is commonly used[2,7,8]. The calculation is straightforward, although for multipass heat exchangers (countercurrent-parallel) the LMTD correction factor must be considered, which leads to an extensive expression involving several parameters. Of the references consulted, only Gudmundsson[5,9] has used the Effectiveness-Number of Transfer Units (ε-NTU) method to experimentally determine the overall heat transfer coefficients, whose calculation is supported by published NTU ratios for different heat exchanger configurations[5,9].

Although it is known that the LMTD and ε-NTU methods share common parameters and concepts that arrive at a similar solution with respect to the thermal capacity of the equipment, few researchers have performed a detailed comparison of both procedures. The classical literature is limited to state that the LMTD approach is useful when the inlet and outlet temperatures of the fluids are known or can be easily determined, because otherwise the calculation involves an iterative trial-and-error process. In these cases, the analysis is more easily performed using the ε-NTU method, based on the performance or effectiveness of the heat exchanger during the transfer of a given amount of thermal energy[10-12].

Jeter[13] presented the theoretical foundations of three conventional methods for analyzing cross-flow heat exchangers for pedagogical purposes. According to the author, the Mean Temperature Difference (MTD) approach is practically obsolete. The LMTD method is preferred for sizing heat exchangers, while the ε-NTU is selected for performance analysis and simulation works[13]. Another study was conducted by Ramana and Sudheerpremkumar[14] with the purpose of calculating the effectiveness in a double tube heat exchanger and comparing the results of the LMTD and ε-NTU methods with the graphically determined values. Although they conclude that the results obtained are equivalent, the LMTD method provided better approximation for the countercurrent arrangement of the fluids, the opposite occurring for the parallel arrangement of the streams. The evaluation was performed for a single data set, without modifying any of the independent variables[14]. Although the methodology for the analysis of two-fluid heat exchangers has been established, the literature consulted does not refer to the study of jacketed shell and tube heat exchangers, where three fluids interact. When the specialists of the production plants need to perform a thermal evaluation of this type of heat exchangers, they do not know which method to use to obtain accurate results.

Considering the above, the objective of this research is to determine the overall heat transfer coefficients in a system of hydrogen sulfide coolers in operation, establishing a comparison between the LMTD and ε-NTU methods. The heat exchangers under study have industrial use in high purity hydrogen sulfide production plants and in sulfur recovery units from the conversion of the above mentioned chemical reagent (Claus process).

2. Materials and methods

2.1 Methodology

The evaluation of the hydrogen sulfide cooling process in jacketed shell and tube exchangers was performed by analyzing the overall heat transfer coefficients, determined from experimental data. The LMTD and ε-NTU methods were used for the calculation.

In heat exchangers with three fluids and two main heat exchange paths, two global heat transfer coefficients are determined[15,16]. One characterizes the internal heat exchange, between the fluid flowing through the tubes and the fluid flowing through the shell; while the other corresponds to the external exchange, between the fluid flowing through the shell and the fluid flowing through the jacket.

For simplification of the calculations, the following assumptions were made[10,17]:

- Heat exchangers operate under steady state conditions.
- The overall heat transfer coefficients, as well as the specific heat of each fluid, remain constant throughout the heat exchanger.
- Heat transfer to the environment is neglected.
- Potential and kinetic energy changes are negligible.
- Heat transfer by longitudinal conduction in the fluids, and in the wall of the tubes and shell, is negligible.
- There are no phase changes.
- During the same operating shift, the hydrogen sulfide flow is constant.
- Measurements of the flow rate of water circulating on the tube side and jacket side were made on common branches, so half

the flow rate is assumed for each exchanger, assuming that the pressure drops in the equipment are similar.

2.2 Description of the installation and experimental technique

The system under study consists of four jacketed shell and tube heat exchangers. Each pair (two units in series) was designed to transfer 138 kW of heat over an area of 49.2 m^2. In each unit, the hydrogen sulfide travels on the shell side, in a single pass, while the water circulates on the tube side, with four passes, and also through the shell jacket. See **Figure 1**. The heat exchangers operate for eight hours in gas cooling mode, and then are taken out of operation to supply steam (tube side and jacket) for four to six hours to remove the sulfur embedded in the gas.

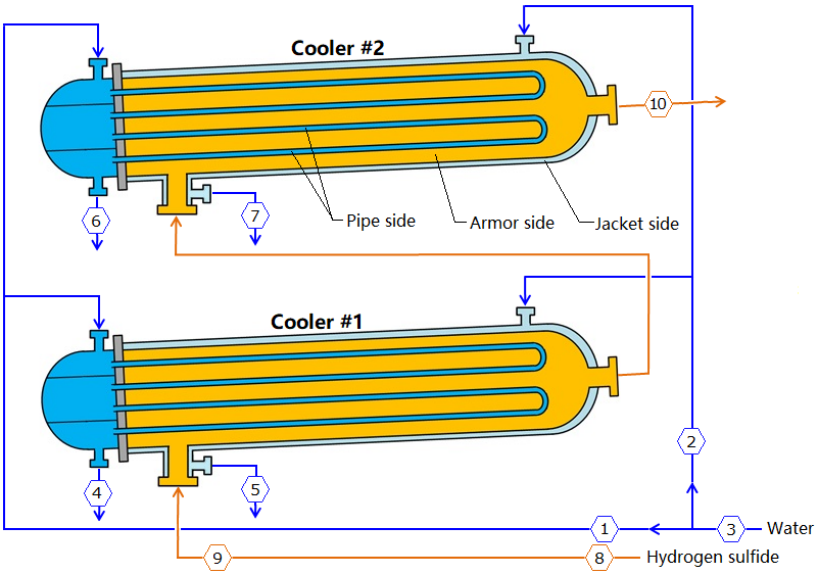

Figure 1. Schematic of a pair of hydrogen sulfide coolers and measurement points.

Due to the uninterrupted production regime in which the object of study is found, a passive experiment was applied (non-experimental research design, of the longitudinal, trend type). This procedure consists in the observation and recording of the input and output variables of the process in the normal working regime of the investigated object, as well as in the observation of the natural arbitrary variations of all technological variables without the active intervention of the researcher in the course of the technological process and without the introduction of preconceived disturbances. Under these premises, the measurements of the fundamental parameters involved in the heat exchange process were performed without manipulation of the variables, analyzing the heat transfer mechanisms as they manifest themselves in their context[18].

The parameters recorded (measurement points as shown in **Figure 1**) are listed below:

- Water flow fed from pipe side.
- Water flow fed from jacket side.
- Water temperature at the inlet of the chiller bank.
- Water temperature through the pipes at the outlet of cooler #1.
- Water temperature through the jacket at the outlet of cooler #1.
- Water temperature through the pipes at the outlet of cooler #2.
- Water temperature through the jacket at the outlet of cooler #2.
- Flow of hydrogen sulfide fed to the coolers.
- Hydrogen sulfide temperature at cooler #1 inlet.
- Hydrogen sulfide temperature at cooler #2 outlet.

The corresponding instruments and their technical characteristics are as follows:

- Temperatures: Ashcroft industrial bimetallic thermowells and thermometers, accurate to 0.1 K.
- Water flow: Proline Prosonic Flow 93T ultrasonic flow meter, accurate to $6.3 \cdot 10^{-6}$ m^3/s.
- Hydrogen sulfide flow: Process signal is sent to a Siemens S7-400 PLC and through Citect SCADA 7.10 the variable is stored and displayed on the control panel computer, accurate to 10^{-4} kg/s.

In the experiment, three observations were carried out on alternate days, during eight hours after the same pair of heat exchangers were put into operation in cooling mode. During each cycle, 20 measurements of the technological variables were taken in each heat exchanger, obtaining a data set with 120 records. In order to reduce random and accidental observation errors (parallax, physical phenomenon and reflection), three replicates were carried out.

The gas temperature at the outlet of cooler #1 was determined by energy balance, as shown in equation (1)[15]. Similarly, the gas temperature at the outlet of cooler #2 was checked using the same equation.

$$T_{b2} = T_{b1} - \left[\frac{\dot{m}_a \cdot Cp_a \cdot (T_{a2} - T_{a1}) + \dot{m}_c \cdot Cp_c \cdot (T_{c2} - T_{c1})}{\dot{m}_b \cdot Cp_b} \right] \quad (1)$$

Where: T [K] is the temperature; $\dot{m}$ [kg/s] is the mass flow rate; and Cp [J/(kg·K)] is the specific heat at constant pressure. The subscripts a , b and c identify the fluids on the tube, shell and jacket side respectively; while 1 and 2 refer to the inlet and outlet conditions of each stream.

2.3 Determination of the overall coefficients using the LMTD method

The determination of the overall heat transfer coefficients, using the LMTD method, is performed by equation (2). The heat transfer area is known by catalog, while the amount of heat transferred during the process, the logarithmic mean temperature difference and its correction factor are calculated from the experimental data: mass flows of each stream, as well as the inlet and outlet temperatures of the fluids[3,7,14].

$$U_{(DTML)} = \frac{Q}{A \cdot \Delta T_{ml} \cdot F} \quad (2)$$

Where: U [W/(m^2·K)] is the overall heat transfer coefficient; Q [W] represents the heat transferred; A [m^2] is the transfer area; ΔT_{ml} [K] is the logarithmic mean temperature difference; and F is its correction factor.

For the internal heat exchange (shell-tubes), the logarithmic mean temperature difference (ΔT_{mli}) is determined by equation (3), based on a multipass equipment. The heat transferred (Q_i) is absorbed by the water circulating on the side of the tubes, and equation (4) is used in its calculation, since no phase changes occur[10].

$$\Delta T_{ml\ i} = \frac{(T_{b2} - T_{a1}) - (T_{b1} - T_{a2})}{\ln\left[(T_{b2} - T_{a1}) / (T_{b1} - T_{a2})\right]} \quad (3)$$

$$Q_i = \dot{m}_a \cdot Cp_a \cdot (T_{a2} - T_{a1}) \quad (4)$$

On the other hand, for external heat exchange (shell-jacket), the logarithmic mean temperature difference (ΔT_{mle}) is calculated by equation (5), established for a heat exchanger with countercurrent flows. In this case, the heat transferred (Q_e) is absorbed by the water on the jacket side, and is determined according to equation (6)[10].

$$\Delta T_{ml\ e} = \frac{(T_{b1} - T_{c2}) - (T_{b2} - T_{c1})}{\ln\left[(T_{b1} - T_{c2}) / (T_{b2} - T_{c1})\right]} \quad (5)$$

$$Q_e = \dot{m}_c \cdot Cp_c \cdot (T_{c2} - T_{c1}) \quad (6)$$

The logarithmic mean temperature difference correction factor is equal to unity (F = 1) for countercurrent or parallel flows. However, in multipass shell-and-tube heat exchangers, it is determined by equations (7) and (8), for any number of shell passages and even number of tube passages, when $R \neq 1$[11,19].

$$F = \left\{\sqrt{R^2+1}\cdot ln\left(\frac{1-S}{1-R\cdot S}\right)\right\}\cdot\left\{(R-1)\cdot ln\left[\frac{2-S\left(R+1-\sqrt{R^2+1}\right)}{2-S\left(R+1+\sqrt{R^2+1}\right)}\right]\right\}^{-1} \quad (7)$$

$$S = \left\{\left[\left(\frac{1-R\cdot P}{1-P}\right)^{1/N}\right]-1\right\}\cdot\left\{\left[\left(\frac{1-R\cdot P}{1-P}\right)^{1/N}\right]-R\right\}^{-1} \quad (8)$$

Where: the parameter *S* is used to simplify the equation for calculating the correction factor; *R* is the ratio between the temperature differences, calculated by equation (9); *P* is the effectiveness of the temperatures, according to equation (10); and *N* is the number of passes through the shell.

$$R = (T_{b1} - T_{b2}) / (T_{a2} - T_{a1}) \quad (9)$$

$$P = (T_{a2} - T_{a1}) / (T_{b1} - T_{a1}) \quad (10)$$

2.4 Determination of the overall coefficients using the ε-NTU method

The determination of the overall heat transfer coefficients, employing the ε-NTU method, is performed by equation (11). The heat transfer area is known, while the minimum thermal capacitance and the ratio of thermal capacitances are calculated from experimental data. The number of transfer units is determined as a function of the exchanger type, thermal effectiveness and the ratio of thermal capacitances[9].

$$U_{(\varepsilon-NUT)} = \frac{C_{min}\cdot NUT}{A} \quad (11)$$

Where: C_{min} [J/(s·K)] is the minimum thermal capacitance; and *NUT* is the number of transfer units. The thermal capacitance of each current is determined through equation (12).

$$C = \dot{m}\cdot Cp \quad (12)$$

In the case of internal heat transfer (shell-tube), the number of transfer units (NUT_i) is calculated based on a multipass heat exchanger, according to equation (13)[10].

$$NUT_i = \frac{1}{\sqrt{1+Cr_i^2}}\cdot ln\left[\frac{2-\varepsilon_i\left(1+Cr_i-\sqrt{1+Cr_i^2}\right)}{2-\varepsilon_i\left(1+Cr_i+\sqrt{1+Cr_i^2}\right)}\right] \quad (13)$$

However, for external heat transfer (shell-shell), when determining the number of transfer units (NUT_e), a countercurrent heat exchanger is considered and equation (14) is used[10].

$$NUT_e = \frac{1}{1-Cr_e}\cdot ln\left(\frac{1-\varepsilon_e\cdot Cr_e}{1-\varepsilon_e}\right) \quad (14)$$

Where: *e* [%] is the thermal efficiency; and *Cr* is the ratio of the thermal capacitances. The subscript *i* refers to the internal heat exchange; while *e* represents the external one.

Thermal efficiency is defined as the ratio between the actual heat transfer magnitude and the maximum possible heat transfer[10-12]. Therefore, for internal heat exchange, it is determined by equation (15), and for external heat exchange by equation (16).

$$\varepsilon_i = Q_i / [C_{mín\ i}\cdot(T_{b1} - T_{a1})] \quad (15)$$

$$\varepsilon_e = Q_e / [C_{mín\ e}\cdot(T_{b1} - T_{c1})] \quad (16)$$

The ratio of the thermal capacitances is calculated by equation (17)[10,11].

$$Cr = C_{mín} / C_{máx} \quad (17)$$

Where: C_{max} [J/(s·K)] is the maximum thermal capacitance.

When the ε-NTU method is used to determine the overall heat transfer coefficients based on experimental data, the inlet and outlet temperatures of both fluids must be known or able to be estimated, unlike when the method is used to calculate the heat transferred and the outlet temperatures in the exchanger (*Rating* problem).

3. Results and discussion

3.1 Application of the LMTD method

Figure 2 shows the behavior of the overall heat transfer coefficients determined by the LMTD method. The calculations were performed for three

hydrogen sulfide flux values.

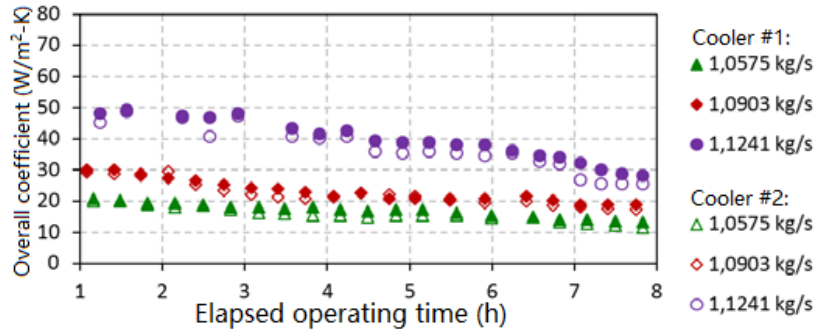

a) Shell-tube exchange

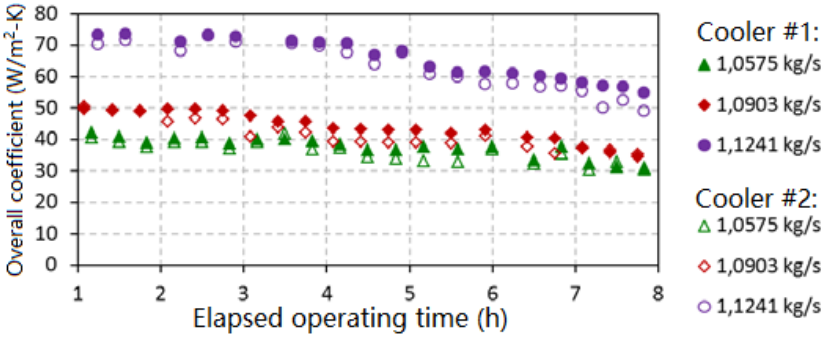

b) Heart-jacket exchange

Figure 2. Behavior of the overall heat transfer coefficient (LMTD method).

During the eight-hour cooling cycle, a decreasing trend in the overall heat transfer coefficient was observed, mainly due to an increase in sulfur incrustations inside the heat exchangers. Over time, the accumulation of sulfur particles that separate from the gas grows on the walls of the tubes and the shell, forming "insulation" layers on the heat transfer surfaces that act to the detriment of heat exchange and cause a decrease in the overall coefficient between 7.5 and 20.8 W/(m^2·K). Other causes of changes in the overall coefficient are variations in flow and in the thermo-physical properties of the fluids, but their incidence is minor compared to the influence of fouling. It was determined that the changes in pressure and temperature of the fluids, by affecting their thermo-physical properties, cause maximum variations in the global heat transfer coefficient equivalent to 1.1 W/(m^2·K) for the tube-shell heat exchange and 3.6 W/(m^2·K) for the heart-jacket exchange.

The overall heat transfer coefficient values improve with increasing hydrogen sulfide mass flow rate, since increasing the gas velocity on the shell side increases the individual convective transfer coefficient and decreases the thermal resistance of the scale. Although the highest heat transfer takes place in cooler #1, the behavior of the overall coefficient is similar in cooler #2.

3.2 Application of the ε-NTU method

Figure 3 shows the behavior of the overall heat transfer coefficients determined by the ε-NTU method. By applying this procedure (for the same experimental data), values comparable to those obtained using the LMTD method were obtained. The decrease in the overall heat transfer coefficients at the end of the duty cycles ranged from 6.9 to 16.7 W/(m^2·K).

To increase the overall heat transfer coefficients and, consequently, improve the heat exchange process in hydrogen sulfide coolers, it is recommended to: shorten the planned time for the cooling cycle; disassemble the tube bundle of each heat exchanger, perform cleaning and reassemble; or replace the tube bundles in operation with new

units. These actions will help minimize the impact of fouling on the thermal efficiency loss of the facility. It is also suggested to increase the flow of water fed to each cooler above 1.167 kg/s, on the tube side, to reach the turbulent regime (*Re* > 4,000).

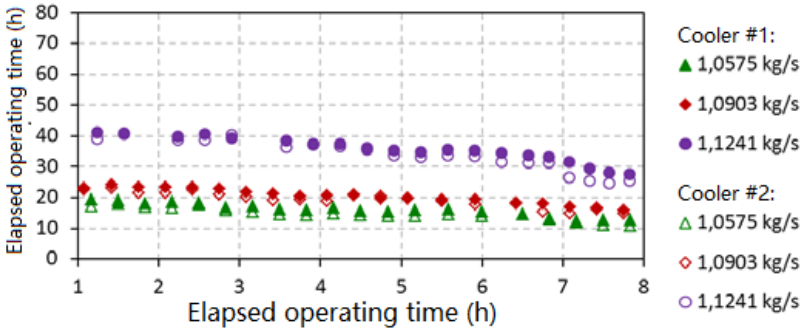

a) Shell-tube exchange

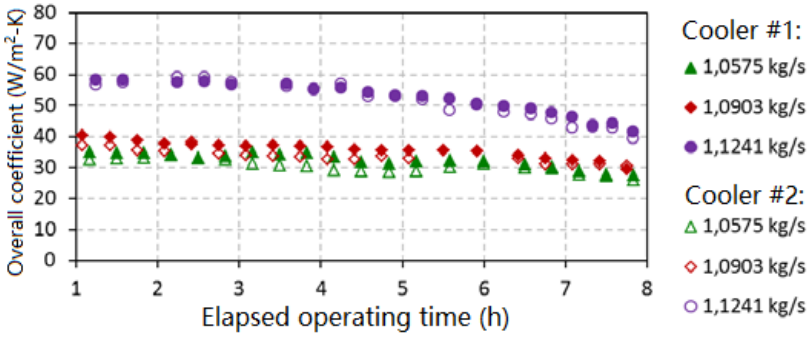

b) Heart-jacket exchange

Figure 3. Behavior of the overall heat transfer coefficient (ε-NUT method).

Table 1. Comparison of values obtained by LMTD and ε-NTU methods

Exchange route	Gas flow [kg/s]	$U_{(DTML)}$–$U_{(\varepsilon\text{-NUT})}$ [W/m²·K]		
		Minimum	Average	Maximum
Internal exchange (shell-tubes)	1.0575	0.1	0.9	2.7
	1.0903	0.4	2.8	7.8
	1.1241	0.2	3.4	8.8
External interchange (heart-jacket)	1.0575	2.2	5.4	11.0
	1.0903	3.4	8.0	13.6
	1.1241	7.1	12.2	15.9

Both methods reveal decreasing trend of the overall heat transfer coefficient with the time course, as well as higher values of this parameter with increasing hydrogen sulfide mass flow rate. However, the values of the overall coefficients calculated using the LMTD method are higher than those determined using the ε-NTU method. **Table 1** shows the variations calculated during the quantitative comparison of the two procedures.

Most of the authors who have evaluated the influence of fouling on the efficiency loss of heat exchangers, based on the determination of global coefficients, used the LMTD method[1,2,6,8,12]. Using the global heat transfer coefficients calculated by the ε-NTU method, lower than those determined by the LMTD, leads to the estimation of conservative values of thermal resistance of the fouling, which leads to the oversizing of the installation. In the case of the external heat exchange pathway, the determination of the global coefficients dispenses with the LMTD correction factor, since it is considered as an exchanger with countercurrent flows (F = 1). This makes the calculation based on the LMTD method, according to equations (2) and

(5), more direct and precise when compared to equations (11) and (14), based on the ε-NTU method. The propagation of measurement errors is accentuated with the latter solution. The ε-NTU method is mainly used in heat exchangers with cross-flow, since for this configuration, no analytical expression was ascertained that allows accurately program and determines the LMTD correction factor. An essential requirement for obtaining reliable results using the ε-NTU method is to properly select the function that best characterizes the heat exchanger under analysis. Several authors have established ranges of preliminary values of the overall coefficient in tubular heat exchangers for heat transfer between gases and water, but no study consulted refers to the heat exchange between hydrogen sulfide and water. **Table 2** compares the results obtained with those published by other researchers. These values are used during the evaluation of heat exchangers to make a quick estimate of the required transfer area by clearing in equation (2), so assuming a more accurate value of the overall heat transfer coefficient will improve the accuracy of the calculations.

Table 2. Comparison of the results obtained with other references

Reference	Heat exchanging fluids	U [W/(m^2·K)]
Ludwig (1993)[20]	Gases–water	17.0–284.0
Kern (1999)[17]	Gases–water	11.0–284.0
Kakaç and Liu (2002)[10]	Gases–water	10.0–250.0
Serth (2007)[11]	Air, nitrogen, etc.–water or brine	57.0–454.0
Present research	Hydrogen sulfide–water (LMTD method)	11.1–73.3
	Hydrogen sulfide–water (ε-NTU method)	11.0–58.9

4. Conclusions

Both the LMTD and ε-NTU methods can be used to determine the overall heat transfer coefficients from experimental data. However, the LMTD method is the one used by most researchers and is recommended to perform the thermal evaluation of the chiller system under study.

Using the LMTD method, global heat transfer coefficients values ranging from 11.1 to 73.3 W/(m^2·K) were obtained, while applying the ε-NTU method, the results ranged from 11.0 to 58.9 W/(m^2·K). The coefficients determined for the heat exchange between hydrogen sulfide and water allow delimiting the range of preliminary values published by other authors for gases and water, in tubular exchangers.

Conflict of interest

The authors declared no conflict of interest.

References

1. Gerami A, Darvishi P. Modeling of the deposit formation on shell and tube heat exchanger of Hasheminejad Gas Refinery Plant. Indian Journal of Science & Reserarch 2014; 5(1): 382–388.
2. Lebele-Alawa BT, Ohia IO. Influence of fouling on heat exchanger effectiveness in a polyethylene plant. Energy and Power 2014; 4(2): 29–34.
3. Igwe JE, Agu CS. Comparative analysis of different fluids in shell pass and two tube heat exchanger. American Journal of Engineering Research 2016; 5(8): 81–87.
4. Friebel T, Haber R, Schmitz U. Lifetime estimation of heat exchangers with consideration of on-line cleaning. In: Fikar M, Kvasnica M (editors). 18th International Conference on Process Control; 2011 Jun 14-17; Tatranská Lomnica, Slovakia. Bratislava: Institute of Information Engineering, Automation and Mathematics, FCFT STU in Bratislava; 2011. p. 434–439.
5. Gudmundsson O. Detection of fouling in heat exchangers using model comparison [PhD thesis]. Reykjavik: University of Iceland; 2015.
6. Torres-Tamayo E, Retirado-Mediaceja Y, Góngora-Leyva E. Experimental heat transfer coefficients for the liquor cooling in plate heat exchanger. Mechanical Engineering 2014; 17(1): 68–77.
7. Torres-Tamayo E, Díaz EJ, Cedeño MP, *et al*. Overall heat transfer coefficients, pressure drop and power demand in plate heat exchangers during the ammonia liquor cooling process. International Journal of Mechanics 2016; 10: 342–348.
8. Jaglarz GA, Taler D. Experimental study of fouling in plate heat exchangers in district heating systems. Journal of Power Technologies 2015; 95(5): 42–46.
9. Gudmunsson O, Palsson OP, Palsson H, *et al*. Comparison of fouling detection between a physical method and a black box model. In: Malayeri MR, Watkinson AP, Müller-Steinhagen H (editors). Proceedings of 9th International Conference on Heat Exchanger Fouling and Cleaning; 2011 Jun 5-10; Crete Island, Greece. Navasota: Heat Transfer Research, Inc.; 2011. p. 391–398.

10. Kakaç S, Lui H, Pramuanjaroenkij A. Heat exchangers: Selection, rating and thermal design. 2nd ed. New York: CRC Press; 2002. p. 520.
11. Serth WR. Process heat transfer principles and applications. Oxford, UK: Elseiver Ltd.; 2007. p. 755.
12. Ardsomang T, Hines JW, Upadhyaya BR. Heat exchanger fouling and estimation of remaining useful life. In: Annual Conference of the Prognostics and Health Management Society; 2013 Oct 14-17; New Orleans. Knoxville: Prognostics and Health Management Society; 2013. p. 1–9.
13. Jeter SM. Effectiveness and LMTD correction factor of the cross flow exchanger: A simplified and unified treatment. In: Brocato J (editor). ASEE Southeast Section Conference; 2013; Cookeville. Washington DC: American Society for Engineering Education; 2013. p. 1–10.
14. Ramana PV, Sudheerpremkumar B. Development of a practical model to find out effectiveness of heat exchanger and its comparison with standard values. International Journal of Innovative Research and Creative Technology 2015; 1(5): 468–472.
15. Ghiwala TM, Matawala VK. Sizing of triple concentric pipe heat exchanger. International Journal of Engineering Development and Research 2014; 2(2): 1683–1692.
16. Saurabh D, Tamkhade PK, Lele MM. Design development and heat transfer analysis of a triple concentric tube heat exchanger. International Journal of Current Engineering and Technology 2016; 5(Sep.): 246–251.
17. Kern DQ. Procesos de Transferencia de Calor (Spanish) [Heat Transfer Processes]. 31st reprint. Mexico D.F.: Compañía Editorial Continental S.A. de C.V.; 1999. p. 980.
18. Hernández-Sampieri R, Fernández-Collado C, Baptista-Lucio MP. Metodología de la investigación (Spanish) [Research methodology]. 5th ed. Mexico D.F.: Mcgraw-Hill; 2010. p. 613.
19. Obregon-Quinones LG, Arrieta-Viana LF, Valencia-Ochoa GE. Thermal design and rating of a shell and tube heat exchanger using a Matlab® GUI. Indian Journal of Science and Technology 2017; 10(25): 1–9.
20. Ludwig EE. Applied process design for chemical and petrochemical plants: Volume 3. 2nd ed. Houston, Texas: Gulf Publishing Company; 1993. p. 500.

Thermal Science and Engineering (2021) Volume 4 Issue 1
doi:10.24294/tse.v4i1.1512

ORIGINAL RESEARCH ARTICLE

Experiment and characterization of dynamic thermal storage characteristics of porous media thermal storage system

Ke Yan, Leming Cheng, Weiguo Zhang, Zhengzhan Shi, Kunzan Qiu*

College of Energy Engineering, Zhejiang University, Hangzhou 310027, Zhejiang Province, China. E-mail: qiukz@zju.edu.cn

ABSTRACT

The aim is to understand the thermal storage characteristics of porous media thermal storage materials under thermal dynamic conditions, and obtain the dynamic thermal storage characteristics parameters of thermal storage materials. In the 120 kW thermal dynamic thermal storage system of porous media, we studied the dynamic thermal storage characteristics of honeycomb porous ceramic thermal storage materials with different pore diameters (2.9, 4, 5.5 mm) and lengths (100–400 mm) under different hot flue gas conditions include thermal storage rate, thermal storage efficiency and storage. The results show that the relationship between the heat storage rate and time is parabolic, and the heat storage efficiency gradually decreases with the heat storage time. At the same time, the regenerative rate and unit regenerative resistance loss increase with the increase of specific surface area or the decrease of pore diameter of regenerator, and the regenerative efficiency increases with the increase of regenerator length. According to the experimental research and analysis, the dynamic heat storage characteristics of porous regenerator can be characterized by heat storage rate, heat storage efficiency and unit heat storage resistance loss.

Keywords: Porous Media; Thermodynamics; Dynamic; Heat Storage; Heat Storage Rate; Heat Storage Efficiency; Heat Storage Resistance

ARTICLE INFO

Received: 26 March 2021
Accepted: 13 May 2021
Available online: 22 May 2021

1. Introduction

High-temperature air combustion technology can recover waste heat from flue gas and preheat combustion air efficiently, which has the dual advantages of greatly saving energy and reducing emission of NO and other pollutants in flue gas[1-4]. Porous media, including honeycomb ceramic regenerator, is widely used in air combustion technology under high temperature because of its excellent thermophysical properties, chemical properties, economic properties, mechanical properties and thermal shock resistance. Its internal heat exchange performance and resistance characteristics determine the overall performance of waste heat recovery system and affect the design of heat storage system[5-6].

Gas-solid heat transfer characteristics in regenerator are important thermal properties of regenerator. Yuan *et al.*[7-9] and Srikanth *et al.*[10-14] analyzed and summarized the gas-solid heat transfer characteristics inside the regenerator, and pointed out that the heat flow rate, heat transfer area and structure of high-temperature air flow are all important parameters that affect the heat storage performance. The experimental conclusion shows that the average convective heat transfer coefficient of porous honeycomb regenerator increases with the increase of high-temperature gas flow rate and the decrease of pore size. Some re-

searchers also use temperature efficiency (the ratio of actual flue gas heat release to theoretical maximum heat release)[15-17] and heat recovery rate (the ratio of actual flue gas heat absorbed by heat storage system to theoretical maximum flue gas heat absorbed)[18-19] to characterize heat storage. The study shows that both of the efficiencies increase with the increase of the length of the regenerator. Other researchers[20-23] defined the ratio of heat stored by the regenerator to resistance loss as the thermal performance index, which represents the heat stored by the regenerator under the condition of unit resistance loss.

In the above experimental study, the gas-solid convective heat transfer coefficient and heat storage efficiency in the regenerator are taken as the parameters to measure the heat storage performance, and the average heat storage of the regenerator in a period of time is studied. Whether these parameters can fully represent the thermal storage characteristics in the design and operation of large thermal storage system, and how the related parameters change dynamically with time, all these problems need further study.

In this paper, the dynamic thermal storage test of porous media honeycomb ceramics with different structures is carried out in the thermal storage test system of 120 kW power, and the dynamic thermal storage characteristics of the regenerator are studied. The thermal storage rate, thermal storage efficiency and specific thermal storage resistance loss are defined as the thermal storage characteristic parameters, which can provide guidance for the industrial design and operation of the porous media thermal storage system.

2. Experiment and method

As shown in **Figure 1**, the porous medium dynamic heat storage test system mainly consists of a combustion engine, a high-temperature flue gas mixing chamber, a porous medium heat storage test chamber, an induced draft fan, a water cooling system and a test system.

The high-temperature flue gas of porous medium dynamic thermal storage system is provided by diesel combustion engine, and the designed thermal power is 120 kW. In order to stabilize the flow rate of high-temperature flue gas entering the porous medium thermal storage test device, a high-temperature flue gas mixing chamber is set in front of the thermal storage test device, which is made of Castable. Three K-type thermocouples are arranged in the mixing chamber along the central axis to measure the temperature distribution in the furnace. In order to observe the combustion flame conveniently, two Shi Ying glass observation windows are set in the middle of the side of the mixing chamber.

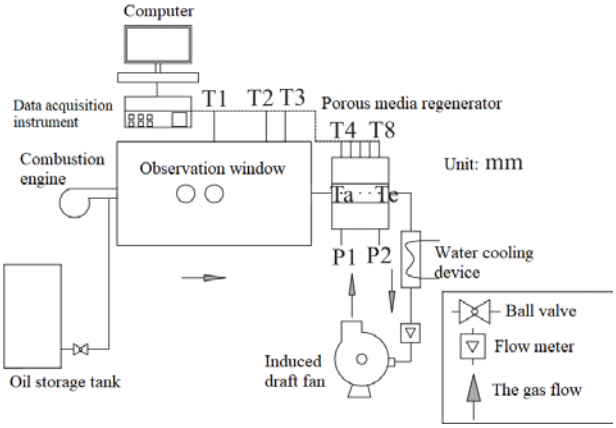

Figure 1. Schematic diagram of dynamic thermal storage test system for porous media.

The heat storage material is placed in the porous medium heat storage test room, and its front view and side view are shown in **Figure 2**.

Porous medium regenerator is made of Castable, and thick silicic acid insulation cotton is laid outside to reduce heat dissipation. The regenerative chamber is 600 mm in length and 200 mm × 200 mm in cross section, and each cross section can discharge 4 pieces of porous medium honeycomb ceramic regenerative bodies of 100 mm × 100 mm × 100 mm (see **Figure 2**).

A total of 10 K-type thermocouples are arranged in the regenerator, in which Ta-Te thermocouples extend into the regenerator wall to measure the temperature of the regenerator wall. T4-T8 thermocouples extend into the center of the section of the regenerative chamber, and measure the temperature at the center of the regenerator, with each thermocouple spaced 100 mm apart.

During the test, eight heat accumulators at the

inlet and outlet of the heat accumulator chamber were kept unchanged, which were used as rectifying heat accumulators to study the heat storage characteristics of the middle heat accumulator. Adjust the axial length of the regenerator by changing the number of discharge blocks of the regenerator.

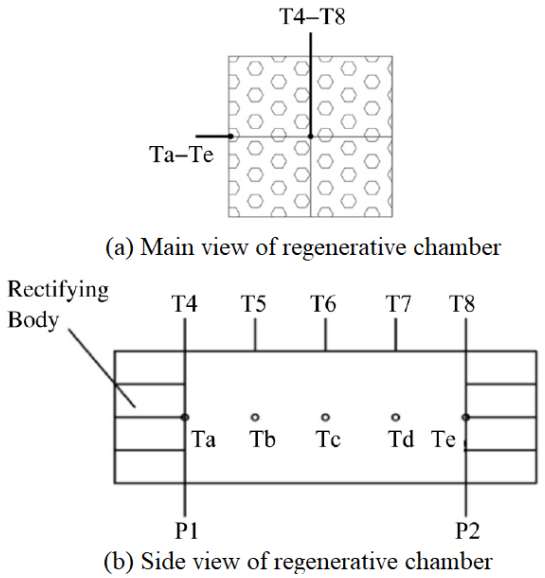

Figure 2. Main drawing of regenerative chamber.

Pressure measuring points are set at the inlet and outlet of the regenerator, and the resistance loss in the regenerator is measured by connecting a differential pressure transmitter with a hose. All thermocouple signals and pressure signals in the test are connected with the computer through the data acquisition instrument, and the data are automatically collected every 5 s and displayed and stored in real time. Flue gas flow is measured by vortex flowmeter. Before each test, the regenerator is at room temperature.

The combustion of medium and diesel oil burners produces high-temperature flue gas, which enters the heat storage test device after being stabilized in the mixing chamber, and heats and stores heat in the porous medium honeycomb ceramic heat storage device. The experimental power of the burner is 60 kW, 72 kW and 84 kW respectively, and the corresponding flue gas mass flow rates are 89 kg/h, 107 kg/h and 125 kg/h, respectively. Three kinds of porous honeycomb ceramic regenerators with the same material and different geometric structures were used in the test, all of which have hexagonal pass, with structural parameters as shown in **Table 1** and test conditions as shown in **Table 2**.

Table 1. Structural parameters of honeycomb ceramic regenerator

Accumulator number	No.1	No.2	No.3
Pass	Hexagonal	Hexagonal	Hexagonal
Material	mullite	mullite	mullite
Wall thickness/mm	1.4	0.9	0.8
Aperture/mm	5.5	4	2.9
Specific surface area/$m^2 \cdot m^{-3}$	462	666	847
Void ratio (ε)	0.63	0.66	0.61
Density/$kg \cdot m^{-3}$	1,169.2	1,074.4	1,232.4

Table 2. Test conditions

Flue gas flow/$kg \cdot h^{-1}$	Heat accumulator	Heat accumulator length/mm
89	No.1	400
	No.2	400
	No.3	400
107	No.1	400
	No.2	400
	No.3	400
125	No.1	400
	No.2	400
	No.3	400
107	No.1	300
107	No.1	200
107	No.1	100

3. Experimental results and discussion

3.1 Dynamic temperature distribution of porous regenerator

Figure 3 shows the dynamic distribution of the average temperature of the regenerator in the process of heat storage under different working conditions. Is the weighted average temperature of each temperature point in the temperature regenerator.

As can be seen from **Figure 3**, with the progress of the heat storage process, the internal temperature of the regenerator rises and gradually stabilizes. When the mass flow rate of flue gas is

constant, the temperature difference of regenerator with different structures is not significant. When the flue gas flow rate is 125 kg/h, the regenerator temperature reaches 600 K in about 600 s, and when the flue gas flow rate is 107 kg/h, the regenerator temperature reaches about 800 s at 600 K and 89 kg/h, it reaches this temperature around 1200 s. The larger the flue gas flow rate, the shorter the time it takes for the regenerator to reach the same temperature, which is consistent with the research results of Srikanth and Assunta *et al.*[10,24]. The reason is that the larger the gas heat flow rate, the larger the flow velocity in the flue gas hole, the more intense the convective heat transfer between gas and solid, the better the heat transfer effect, and the shorter the time for solid to approach the temperature of gas flow.

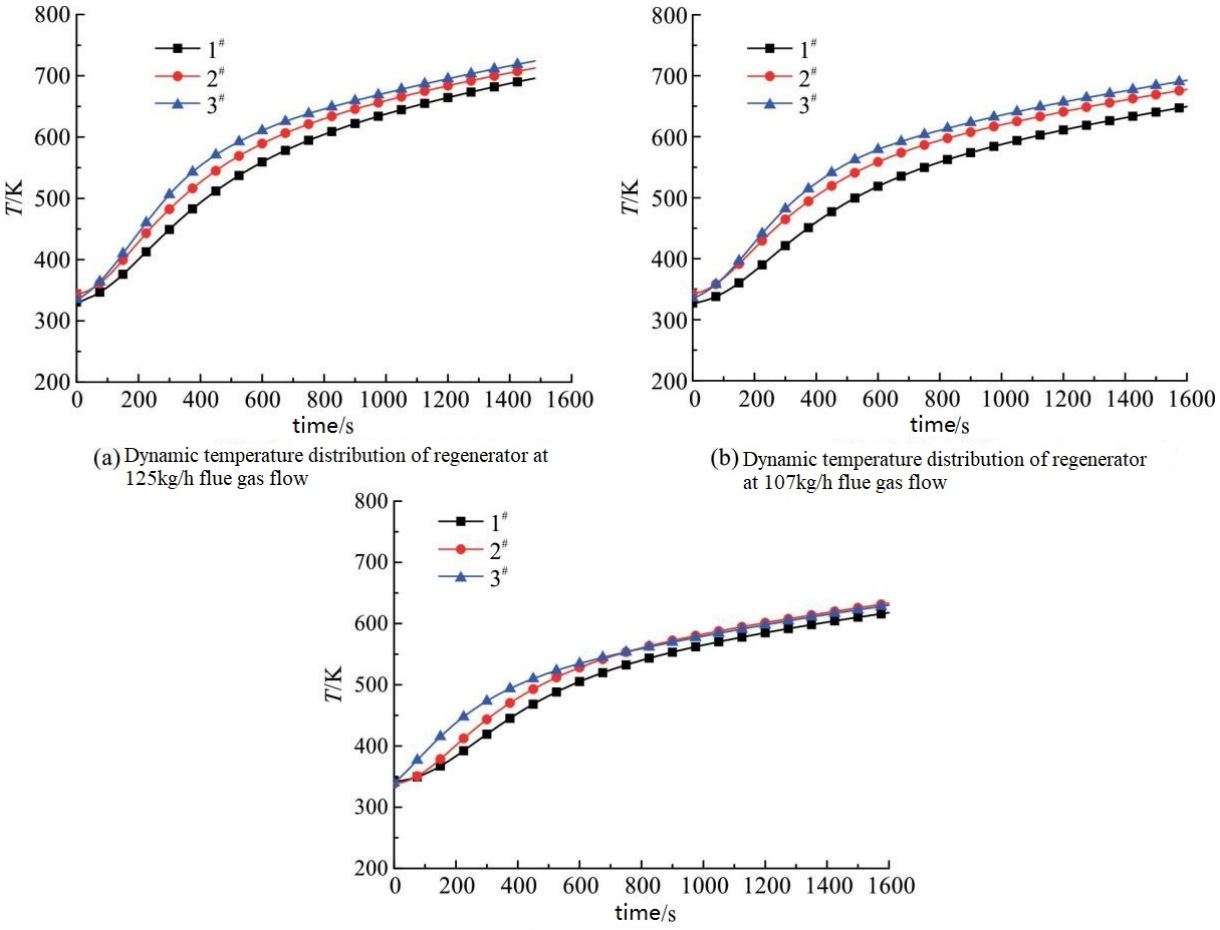

(a) Dynamic temperature distribution of regenerator at 125kg/h flue gas flow

(b) Dynamic temperature distribution of regenerator at 107kg/h flue gas flow

(c) Dynamic temperature distribution of regenerator at 89kg/h flue gas flow

Figure 3. Dynamic temperature distribution of heat accumulator under different working conditions.

3.2 Dynamic flow characteristics of flue gas in porous regenerator

In the process of heating the regenerator with high temperature flue gas, the velocity of flue gas flowing through the regenerator changes dynamically due to the dynamic change of the regenerator temperature. The velocity in the high temperature flue gas hole can be calculated by formula (1).

$$v = \frac{q_v}{A_\Sigma} \tag{1}$$

Where: q_v is the gas flow rate, measured by the flowmeter in real time, m^3/s; A is the cross-sectional area of the regenerator, which is 0.04 m^2 in this paper; ε is the porosity of the regenerator.

Figure 4 shows the relationship between the velocity of flue gas in the hole and time under different working conditions. In the initial stage of heat storage, the increase of the temperature inside the regenerator causes the volume expansion of flue gas flowing through it, which in turn increases the flow velocity in the hole, and then the temperature

of the regenerator gradually stabilizes and the flow velocity in the hole gradually fluctuates at a certain value. With the increase of high temperature flue gas mass flow rate, the velocity in flue gas hole increases; With the decrease of the void ratio of the regenerator, the flow area of the regenerator per unit section decreases, and the flow velocity in the hole increases when the flue gas flow rate is constant.

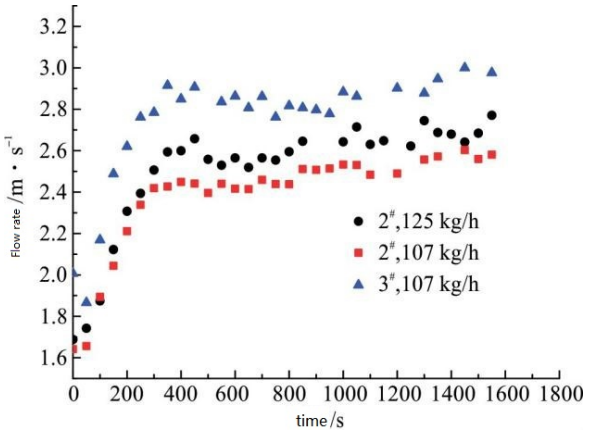

Figure 4. Variation of flow velocity in flue gas hole at inlet with time.

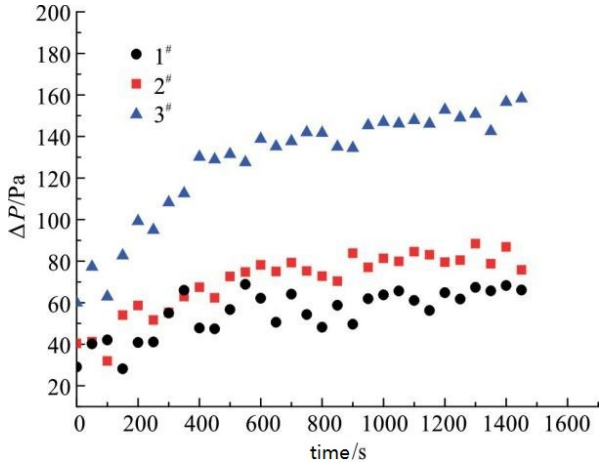

Figure 5. Variation of pressure drop of regenerator with time under 125 kg/h flue gas flow rate.

Figure 5 shows the resistance loss of regenerator with different structures under the flue gas flow rate of 125 kg/h. It can be seen from the figure that the flow rate in the hole and the temperature of the regenerator rapidly increase (see **Figure 3** and **Figure 4**) during the start time of heat storage. It results in an increase in resistance loss, and then the temperature of the regenerator and the flow rate in the hole gradually stabilize, and the resistance loss also gradually stabilizes. Resistance loss under the same flue gas flow rate: No.3 regenerator > No.2 regenerator > No.1 regenerator. The smaller the diameter of the regenerator is, the greater the velocity in the hole and the greater the resistance loss along the path. The increase of specific surface area of regenerator means that the contact area between airflow and regenerator increases, which leads to the increase of friction between airflow and regenerator and the increase of resistance loss. Therefore, the resistance loss of regenerator increases with the decrease of pore size and the increase of specific surface area. This conclusion is consistent with the research results of Yuan and others[25-30].

3.3 Characterization parameters of thermal storage characteristics of porous thermal storage materials

3.3.1 Heat storage rate

In **Figure 3**, there is little difference in dynamic temperature distribution curves of regenerators with different structures. In order to more clearly study and compare the temperature change speed of porous regenerators with different structures in the process of heat storage, the “heat storage rate” is used here to characterize, which is defined as the heat storage capacity per unit mass of regenerators in a certain period of time. According to the definition of “heat storage rate”, it can be used to express the degree of heat storage of porous heat storage materials:

$$Q_v = \frac{\int_{T_1}^{T_2} C_p dT}{\Delta t} \tag{2}$$

Where: T_1 and T_2 are the average temperatures before and after each acquisition by the data collector; Setting value of C_p.

Figure 6 shows the relationship between heat storage rate and time under different working conditions under the above definition of heat storage rate.

It can be seen from **Figure 6** that the change trend of heat storage rate under different working conditions is similar, and the peak time is around 200 s. The area before the peak is called the heat storage front section, and the area after the peak is called the heat storage rear section. If the radiant

heat transfer between flue gas and regenerator is not considered, the heat storage rate depends on the intensity of gas-solid convection heat transfer. In the front stage of heat storage, the temperature difference between gas and solid in the regenerator is large, and at this time, the flow velocity in the hole is rapidly increasing (see **Figure 4**), the convection heat transfer intensity of the gas-solid is intense, and the heat storage rate is almost linearly increasing. In the later stage of heat storage, the temperature difference between gas and solid gradually decreases, the flow velocity in the hole gradually stabilizes, and the heat storage rate gradually decreases, and there is little difference between the heat storage rates of different regenerators in the later stage of heat storage.

It can be seen from **Figure 6** that for the same regenerator, the greater the flue gas heat flow, the greater the heat storage rate. Under the same flue gas heat flow rate, the regenerative rate of No.3 regenerator is higher than that of No.1 and No.2. The wall thickness and porosity of the three kinds of regenerators are similar, and the third regenerator has the smallest aperture and the largest specific surface area. Yuan[7] and others pointed out that the smaller the pore size, the better the thermal performance of the regenerator. Meng[9], Wen[11] and others pointed out that the larger the specific surface area, the larger the gas-solid heat transfer area, and the more heat transfer under the same conditions, the better the thermal performance of the regenerator.

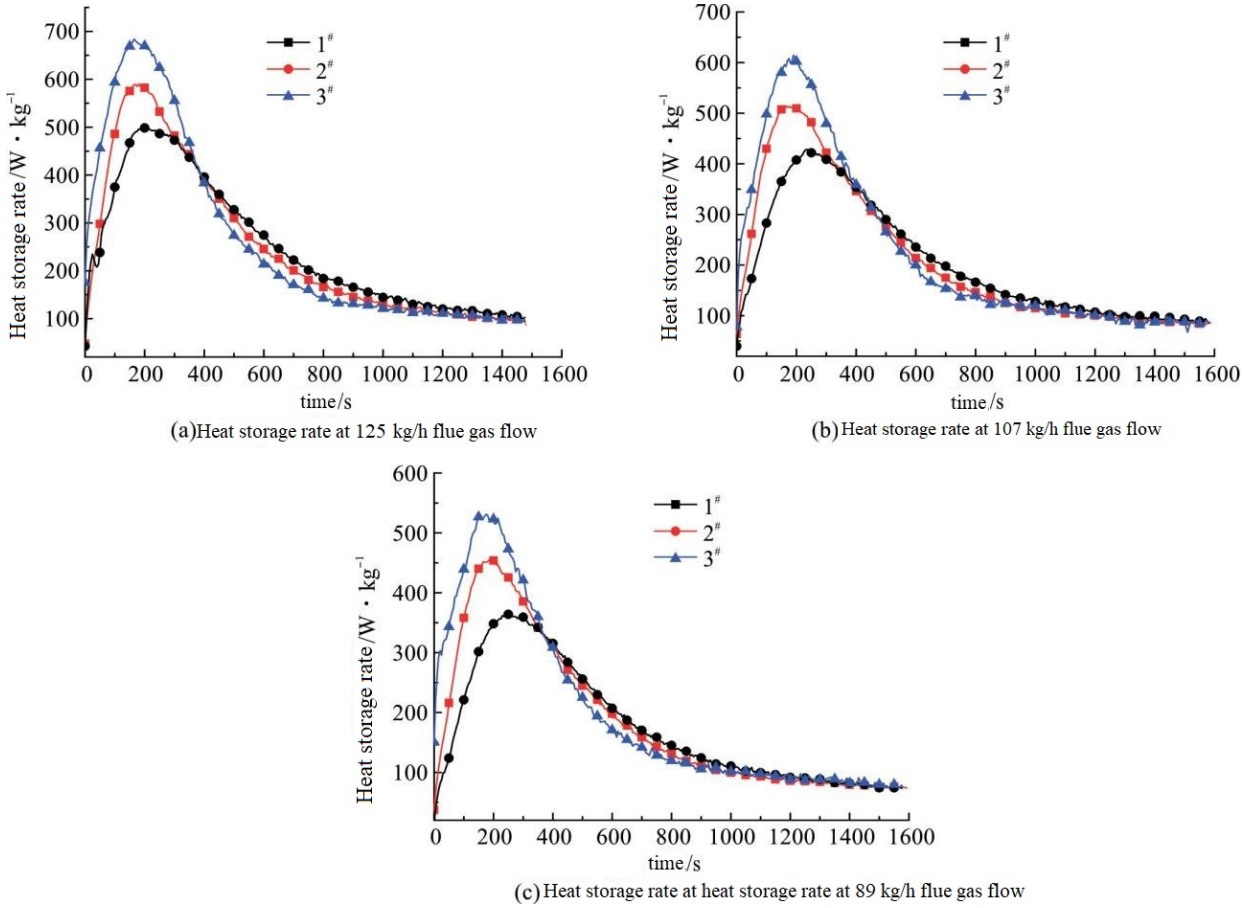

Figure 6. Heat storage rate of heat accumulator under different working conditions.

The two views seem unrelated, but in fact they are mutual verification. Because the specific surface area of the regenerator is determined by the pore size and wall thickness. When the wall thickness of the regenerator is similar, the smaller the pore diameter, the larger the specific surface area. **Figure 6** verifies the viewpoint of the above researchers. Therefore, when other conditions are the same or close in this case, the smaller the pore size of the regenerator, the larger the specific surface area, the larger the gas-solid heat exchange area, the faster the heat storage, and the better the heat storage ef-

fect.

The gas-solid convective heat transfer coefficient of the regenerator proposed by previous scholars can reflect the gas-solid heat transfer inside the regenerator, while the heat storage rate proposed in this paper reflects the direct result of gas-solid heat transfer, that is, the speed of heat storage. Compared with the gas-solid convective heat transfer coefficient, the heat storage rate is more intuitive to characterize the heat storage characteristics, and it is more efficient to select the regenerator suitable for the heat storage system than the size of the heat storage rate. Therefore, the heat storage rate proposed in this paper has more reference value than the gas-solid convective heat transfer coefficient proposed by previous scholars.

3.3.2 Heat storage efficiency

The speed of heat storage of porous media regenerator is characterized by heat storage rate. Except that, in the process of dynamic heat storage, the ability of regenerator to store the total heat carried by high-temperature flue gas is also an important feature of heat storage material, which reflects the ability of regenerator to utilize the heat passing through it, that is, the degree of utilization of flue gas waste heat. “Heat storage efficiency” can be defined to characterize:

$$\eta = \frac{T_{in} - T_{out}}{T_{in} - T_0} \tag{3}$$

Where, T_{in} is the high temperature flue gas temperature at the entrance of the regenerative body; T_{out} for storage Flue gas temperature at hot body outlet; T_0 is the initial temperature of the heat accumulator Degrees.

Heat storage efficiency means the ratio of the actual heat release of high-temperature flue gas to the theoretical maximum heat release, which is basically the same as the definitions of temperature efficiency and heat recovery rate mentioned earlier, and both reflect the utilization degree of heat carried by the regenerator on flue gas. The higher the heat storage efficiency, the more fully the heat carried by flue gas is utilized. Hong *et al.*[17] pointed out that the length of the regenerator is the main factor affecting the temperature efficiency, but the void ratio has little effect on it, so this paper focuses on the study of the heat storage efficiency of different length regenerators.

Figure 7 shows the dynamic heat storage efficiency of No.1 regenerator at different lengths when the flue gas flow rate is 107 kg/h. With the increase of heat storage time, the temperature difference between inlet and outlet of flue gas becomes smaller and smaller, and the heat storage efficiency also decreases gradually. Therefore, at the beginning of heat storage, the heat storage efficiency is the highest, at this time, the flue gas waste heat of the regenerator is fully utilized, and the heat storage efficiency has dropped below 0.3 when the heat storage reaches 1,000 s. At any moment, the longer the length of the regenerator, the greater the heat storage efficiency. Because this dynamic regenerative efficiency can be used to reflect the utilization degree of flue gas waste heat by the regenerator at a certain moment.

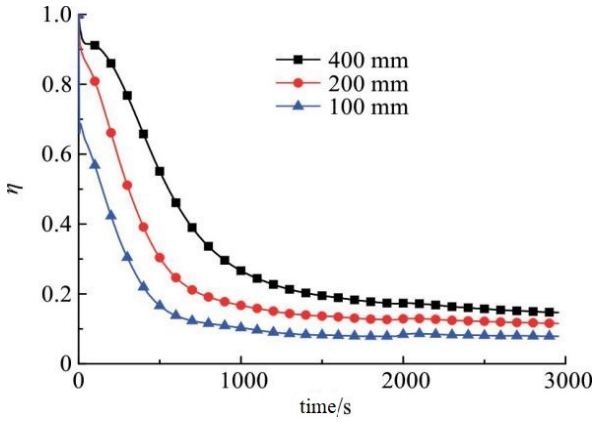

Figure 7. Dynamic heat storage efficiency of No.1 regenerator under 107 kg/h flue.

3.3.3 Unit heat storage resistance loss

According to the experimental results, it is found that when the diameter or specific surface area of the regenerator changes, the influence on the regenerative rate and the resistance loss of the regenerator is the same, that is, the resistance loss will also increase with the increase of the regenerative rate. Therefore, the resistance that the regenerator needs to overcome to store the unit heat is also an important index of the design and operation of the regenerator system, which reflects the loss of the unit heat stored by the regenerator.

Based on the experimental research and analysis, the characteristic parameter "resistance loss per unit heat storage" is defined as the resistance loss that the regenerator needs to overcome to store the unit heat, which is a dimensionless number and can be calculated by formula (4):

$$I' = \frac{\Delta P \bullet q_v}{Q_v \bullet m} \tag{4}$$

Where: ΔP is the pressure drop of the regenerator; q_v is flue gas flow; Q_v is the heat storage rate; m is the total mass of the regenerator.

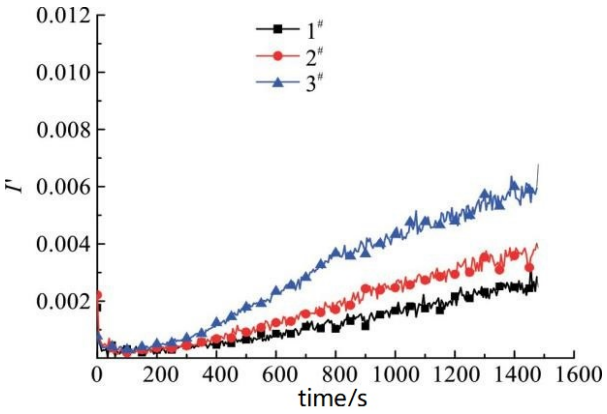

Figure 8. Unit heat storage resistance loss at 125 kg/h flue.

Figure 8 shows the change with time of the unit regenerative resistance loss of three kinds of regenerators calculated by formula (4). As can be seen from the figure, when the flue gas flow rate is 125 kg/h, with the heat storage time, the unit heat storage resistance loss gradually increases linearly. Because the heat storage rate gradually decreases (see **Figure 6**) and the resistance loss gradually increases (see **Figure 5**). With the decrease of pore size or the increase of specific surface area, the resistance loss of unit heat storage increases, because when the pore size decreases, the resistance loss increases more than that of heat storage. The magnitude of the rate increase. Compared with the thermal performance index put forward by Lu[20], the resistance loss per unit heat storage can more intuitively reflect the resistance loss that different regenerators need to overcome to store unit heat. In the industrial heat storage system, not only the aforementioned parameters such as heat storage rate and heat storage efficiency should be considered, but also the unit heat storage resistance loss, because the resistance characteristics will also affect the design of the heat storage system.

4. Conclusion

(1) The heat storage rate is defined. The relationship between heat storage rate and time is parabola, and its size is mainly related to the structure of the regenerator and the heat flow. The greater the heat flow, the faster the heat storage; the smaller the pore size of the regenerator or the larger the specific surface area, the greater the heat storage rate.

(2) The heat storage efficiency and the heat storage efficiency at the beginning of heat storage are defined.

The rate is the highest and then decreases gradually with the heat storage. The longer the length of the regenerator, the higher the heat storage efficiency, which indicates that the regenerator makes full use of the waste heat of flue gas.

The unit regenerative resistance loss is defined, which increases with the decrease of regenerator aperture or the increase of specific surface area.

Therefore, the regenerator with small pore size or large specific surface area can realize rapid heat storage, but at the same time, the resistance loss of the regenerator will also increase. Increasing the regenerator properly can improve the heat storage efficiency.

Conflict of interest

The authors declared no conflict of interest.

References

1. Cheng L, Cen K, Zhou S, *et al*. Duokong jiezhi ranshao lilun yu jishu (Chinese) [Combustion theory of porous media and technology]. Beijing: Chemical Industry Press; 2013. p. 199.
2. Blasiak W, Yang W, Rafidi N. Physical properties of a LPG flame with high-temperature air on a regenerative burner. Combustion and Flame 2004; 136(4): 567–569.
3. Nishimura M, Suzuki T, Nakanishi R, *et al*. Low-NO_x combustion under high preheated air temperature condition in an industrial furnace. Energy Conversion and Management 1997; 38 (10–13): 1353–1363.
4. Hanamura K, Echigo R, Zhdanok SA. Superadiabatic combustion in a porous-medium. International Journal of Heat and Mass Transfer 1993; 36(13):

3201–3209.
5. Mitra HK. Tinkering-to-grip with problems, industrial. Transactions of the Indian Ceramic Society 1982; 41(5): 115–124.
6. Jia C, Xie Z, Sun J, *et al*. Fengwo taoci xureti de yanjiu xianzhuang (Chinese) [Research on honeycomb ceramic heat accumulator Research on the Status quo]. Refractory Materials 2009; 43(1): 64–68.
7. Yuan W. Experimental study on heat transfer and resistance characteristics of honeycomb heat accumulator [MSc thesis]. Hangzhou: Zhejiang University; 2013.
8. Zhang Z, Liu Y, Gao Z, *et al*. Simulation study of flow and heat transfer in ceramic regenerator. Internal Combustion Engine & Powerplant 2010; (2): 18–22.
9. Meng X. Research of Ceramics heat regenerator's heat transfer [MSc thesis]. Wuhan: Wuhan University of Technology; 2012.
10. Srikanth O, Khivsara SD, Aswathi R, *et al*. Numerical and experimental evaluation of ceramic honeycombs for thermal energy storage. Transactions-Indian Ceramic Society 2017; 76(2): 1–6.
11. Wen T, Tian J, Lu TJ, *et al*. Forced convection in metallic honeycomb structures. International Journal of Heat and Mass Transfer 2006; 49(19–20): 3313–3324.
12. Luo Z, Wang C, Xiao G, *et al*. Simulation and experimental study on honeycomb-ceramic thermal energy storage for solar thermal systems. Applied Thermal Engineering 2014; 73(1): 622–628.
13. Duprat F, Lopez GL. Comparison of performance of heat regenerators: Relation between heat transfer efficiency and pressure drop. International Journal of Energy Research 2001; 25(4): 319–329.
14. Rafidi N, Blasiak W. Thermal performance analysis on a two composite material honeycomb heat regenerators used for HiTAC burners. Applied Thermal Engineering 2005; 25(17–18): 2966–2982.
15. Noh DS, Hong SK, Ryou HS, *et al*. An experimental and numerical study on thermal performance of a regenerator system with ceramic honeycomb. KSME International Journal 2001; 15(3): 357–365.
16. Kang K, Hong S, Noh D, *et al*. Heat transfer characteristics of a ceramic honeycomb regenerator for an oxy-fuel combustion furnace. Applied Thermal Engineering 2014; 70(1): 494–500.
17. Hong SK, Noh DS, Lee EK. Improvement in thermal efficiency of regenerator system by using oxy-fuel combustion. Applied Thermal Engineering 2015; 87: 648–654.
18. You Y, Huang H, Shao G, *et al*. A three-dimensional numerical model of unsteady flow and heat transfer in ceramic honeycomb regenerator. Applied Thermal Engineering 2016; 108: 1243–1250.
19. Wang J, Qi H, Li Y, *et al*. Experimental study on heat transfer performance of honeycomb heat regenerator. Journal of Engineering Thermophysics 2003; 24(5): 897–899.
20. Lu TJ. Heat transfer efficiency of metal honeycombs. International Journal of Heat and Mass Transfer 1999; 42(11): 2031–2040.
21. Liu H, Yu QN, Zhang ZC, *et al*. Two-equation method for heat transfer efficiency in metal honeycombs: An analytical solution. International Journal of Heat and Mass Transfer 2016; 97: 201–210.
22. Liu S, Zhang Y, Liu P. New analytical model for heat transfer efficiency of metallic honeycomb structures. International Journal of Heat and Mass Transfer 2008; 51(25–26): 6254–6258.
23. Gu S, Lu TJ, Evans AG. On the design of two-dimensional cellular metals for combined heat dissipation and structural load capacity. International Journal of Heat and Mass Transfer 2001; 44(11): 2163–2175.
24. Assunta A, Buonomo B, Manca O, *et al*. Thermal energy storages analysis for high temperature in air solar systems. Applied Thermal Engineering 2014; 71(1): 130–141.
25. Cadavid Y, Amell A, Cadavid F. Heat transfer model in recuperative compact heat exchanger type honeycomb: Experimental and numerical analysis. Applied Thermal Engineering 2013; 57(1–2): 50–56.
26. Yuan F, Wang H, Zhou P, *et al*. Heat transfer performances of honeycomb regenerators with square or hexagon cell opening. Applied Thermal Engineering 2017; 125: 790–798.
27. Zheng Z, Qiu X, Qi F, *et al*. Experimental study of heat transfer and resistance characteristics on honeycomb ceramic regenerator. Petro-Chemical Equipment 2013; 42(1): 9–13.
28. Miao J, Cheng L, Zhang J, *et al*. Experimental study on pressure drop profiles of one-way flow and reciprocal flow in honeycomb regenerator system. Energy Engineering 2013(1): 12–16.
29. Gao Y, Yong H, Xu Z, *et al*. Thermal state experiment research on the heat transfer and resistance characters of honeycomb ceramic regenerator. Energy for Metallurgical Industry 2008; 27(5): 25–27.
30. Liu YQ, Chen XC, Liu RX. Numerical simulation of heat transfer and gas flow characteristics in honeycomb ceramics. Advanced Materials Research 2011; 156–157: 984–987.

Thermal Science and Engineering (2021) Volume 4 Issue 1
doi:10.24294/tse.v4i1.1513

ORIGINAL RESEARCH ARTICLE

Influence of Na_2CO_3 on combustion performance of civil clean coke

Bingning Wang[1,3], Shoujun Liu[2,3*], Song Yang[2,3], Xudong Yan[1,3], Liangyu Chen[1,3], Jin Li[1,3]

[1] *Taiyuan Green Coke Energy Co., Ltd., Taiyuan 030006, China.*

[2] *School of Chemical Engineering, Taiyuan University of Technology, Taiyuan 030024, China. E-mail: 13303460889@163.com*

[3] *Shanxi Engineering Research Center of Civil Clean Fuel, Taiyuan 030024, China.*

ABSTRACT

Civil clean coke is a low-pollutanted civil clean fuel made of coal and multi-functional composite additives by high-temperature carbonization, which is of positive significance to solve the problem of air pollution caused by civil bulk combustion. However, problems such as high ignition temperature and poor combustion performance exist in the use of civil clean coke in the early stage. In this paper, Lvliang fat coal is taken as the research object. Coke samples are prepared by adding different additives and high-temperature carbonization. The influence of Na_2CO_3 on the combustion performance of civil clean coke is analyzed by TG-DTG, BET, thermodynamics kinetics and other methods. The results show that the civil clean coke prepared by high temperature dry distillation with 1.0% Na_2CO_3 added, the ignition temperature by impregnation method is 53 K lower than that of coke without additives; after adding Na_2CO_3, the TG and DTG curves of coke shifted significantly to the left, the average combustion rate increased from 0.38 mg/min to 0.75 mg/min, and the comprehensive combustion index increased from 2.01×10^{-10} $mg^2/(min^2 \cdot K^3)$ to 11.14×10^{-10} $mg^2/(min^2 \cdot K^3)$; after adding Na_2CO_3, the specific surface area of coke is significantly increased and the pore structure is more developed, which promotes the oxygen transfer in the combustion process and significantly reduces the apparent activation energy of the combustion system. The apparent activation energy in the low temperature zone is reduced from 454.28 kJ/mol to 306.85 kJ/mol, and the apparent activation energy in the high temperature zone is reduced from 557.36 kJ/mol to 95.36 kJ/mol. The combustion performance of civil clean coke is improved.

Keywords: Na_2CO_3; Civil Clean Coke; Ignition Temperature; TG-DTG; Combustion Characteristics; Apparent Activation Energy; Pollution Control

ARTICLE INFO

Received: 2 April 2021
Accepted: 20 May 2021
Available online: 4 June 2021

1. Introduction

According to statistics, China's annual coal consumption is about 4 billion tons, of which about 20% is used for domestic stoves. Domestic burning of coal has the characteristics of low combustion efficiency and high pollutant emission, which is one of the main reasons for smog[1,2]. How to solve the problem of raw coal combustion pollution and actively promote the prevention and control of air pollution is imminent. Replacing bulk coal with a clean energy supply (such as electricity, gas, etc.) is one of the important ways to control bulk coal. However, China is geographically complex. In the vast rural areas, rural-urban fringe, and other remote areas, the progress of changing coal to gas and coal to electricity projects has not been completed or the gas supply is tight, and the cost of government subsidies is large. Therefore, using coal-based clean fuel instead of bulk coal has become one of the preferred ways[3,4].

At present, the carbon-based clean fuels with feasible technology, low cost, and widely recognized by users mainly include civil briquette, civil blue carbon, and civil clean coke[5]. Among them, civil clean coke is the product of high-temperature carbonization of coal, which has the characteristics of smoke-free, low dust, low sulfur oxide, and nitrogen oxide emissions, and is an effective measure to solve the pollution of bulk coal[6,7]. Since 2015, more than 700,000 tons of civil clean coke have been promoted in Taiyuan, Yuncheng, Jinzhong and Dalian, and good environmental benefits have been achieved. However, in the process of promotion, it is found that civil clean coke has problems such as high ignition temperature and ignition delay. How to improve the combustion performance of civil clean coke is of great significance to the practical application and promotion of civil clean coke.

So far, most of the combustion performance-related studies have been carried out on the improvement of the combustion performance of coal and semi-coke. Additives that can improve the combustion performance of coal can be roughly divided into alkali metals, alkaline earth metals, transition metals, rare earth metals, waste additives, etc.[8-10]. Zou *et al*.[11] studied the effects of four iron-containing substances such as hematite, converter dust, converter mud, and blast furnace dust on the combustion performance of pulverized coal, and found that hematite, converter dust, and converter mud can significantly improve the combustion performance of pulverized coal, while blast furnace dust has an inhibitory effect on the combustion of pulverized coal. Gong *et al*.[12] studied the catalytic effect of rare earth metal oxide CeO_2 and transition metal oxide Fe_2O_3 on coal combustion, and found that the higher the degree of coalification, the smaller the particle size of coal, and the more obvious the catalytic combustion supporting effect of the two additives. Liu *et al*.[13] studied the effects of

MnO_2, $CaCO_3$, and other substances on the combustion performance of lean coal and found that MnO_2 can significantly promote the combustion of lean coal. Chen *et al*.[14] studied the effect of calcium-based additives on the combustion performance of inferior coal with high ash content The addition of $CaCl_2$ can improve the combustion efficiency of pulverized coal. Gong *et al*.[15] added Fe_2O_3 and CeO_2 to the semi-coke, respectively, and the combustion performance of the semi-coke was significantly improved. Zhou *et al*.[16] studied the effects of Cao, Fe_2O_3, and MnO_2 on the combustion performance of anthracite and semi-coke. The results showed that the improvement of combustion performance was related to the properties of additives, the properties of the fuel itself, and combustion conditions. So far, the research on the combustion performance of civil clean coke has not been reported.

Based on this, in this paper, the civil clean coke is prepared by high-temperature dry distillation after adding additives to coal. The effects of different additives, addition amount, and addition method on the combustion performance of civil clean coke are investigated. The mechanism of Na_2CO_3 improving the combustion performance of civil clean coke is discussed through TG-DTG, BET and thermal analysis kinetics, in order to provide theoretical guidance for the improvement of the combustion characteristics of civil clean coke.

2. Experimental method

The coal used in the experiment is Lvliang fat coal. Samples were prepared according to the national standard method and were grinded to less than 3 mm for standby. See **Table 1** for element and industrial analysis of experimental coal. $FeCl_3$, CuO, KOH, Na_2CO_3, and $CaCO_3$ used in the experiment are analytical pure reagents, and the manufacturer is Sinopharm Chemical Reagent Co., Ltd.

The coal samples were mixed by the mechanical mixing method and impregnation method. Mechanical mixing method: accurately weigh certain amounts of additives and mix them with 100 g of air-drying based pulverized coal below 3 mm, and then mix them evenly for standby.

Impregnation method: mix 100 g of air-drying-based pulverized coal below 3 mm with 10 mL of impregnation solution containing certain amounts of additives. After standing for 12 h, dry it

in a 378 K drying oven for 2 h. The impregnated coal sample is placed in the dryer for use.

Table 1. The ultimate analysis and proximate analysis of testing coal

Sample name	Elemental analysis w_{ad}/%					Industrial analysis w_{ad}/%				$Q_{net,ad}$/(MJ·kg^{-1})
	C	H	O	N	S	M	A	V	FC	
Lvliang fat coal	79.25	4.60	4.91	1.38	0.89	0.60	8.37	29.13	61.90	31.35

Add 10 mL of distilled water to the above-mixed coal sample and stir it evenly. Tamp the coal sample through a mold to obtain a cylindrical coal cake (with a bulk density of 1.1 g/cm^3). The coal cake is carbonized in a tubular furnace at high temperatures to obtain civil clean coke.

Temperature rise procedure of tubular furnace: the constant temperature for 10 minutes after rising from room temperature to 1,073 K at a temperature rise rate of 10 K/min, and constant temperature for 60 minutes after rising from 1,073 K to 1,323 K at a temperature rise rate of 5 K/min. Put the prepared coal cake into the high-temperature tubular furnace at 1,073 K, take out the sample after the program is completed, and prepare the sample to obtain the coke analysis sample with a particle size of less than 0.2 mm.

TG and DTG curves were obtained by using Setsys Evolution type high-temperature thermogravimetric analyzer produced by Setaram company. The sample mass is 7 mg, the temperature rise range is room temperature to 1,273 K, the temperature rise rate is 15 k/min, the carrier gas is air, and the carrier gas flow rate is 100 mL/min. In addition, the ignition temperature of coke was measured by Hebi Shenhua ignition point instrument[17].

The pore structure characteristics of coke samples were tested by ASAP2020 type adsorption instrument produced by Micromeritics in the United States. The mass fractions of C, H, O, N and S of coke samples were determined by Elemental Vario MICRO cube element analyzer.

3. Experimental results and discussion

3.1 Effect of different additives on ignition temperature of civil clean coke

In the experimental coal, $FeCl_3$, CuO, KOH, Na_2CO_3 and $CaCO_3$ (mass ratio of additives to coal samples) were added by the impregnation method, respectively; then the civil clean coke was obtained by high-temperature carbonization. The experimental coal without additives was also obtained by high-temperature carbonization. The ignition temperature of different civil clean coke is investigated, and the results are shown in **Figure 1**.

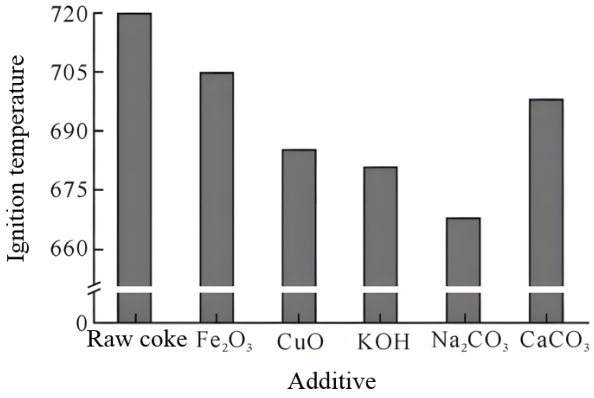

Figure 1. The ignition temperatures of civil clean coke with different additives.

It can be seen from **Figure 1** that after adding different additives, the ignition temperature of civil clean coke decreases to varying degrees; the ignition temperature of the original coke is 720 K. After adding $FeCl_3$, CuO, KOH, Na_2CO_3 and $CaCO_3$, the ignition temperature decreases by 15, 35, 40, 53 and 22 K, respectively, among which the effect of alkali metal Na_2CO_3 and KOH on the ignition temperature of civil clean coke is more significant. In order to further explore the combustion supporting effect of alkali metals in civil clean coke, Na_2CO_3, the additive with the largest drop in ignition temperature, is taken as the research object for specific analysis.

3.2 Conditions for Na_2CO_3 to improve combustion performance of clean coke

3.2.1 Effect of Na_2CO_3 addition method on ignition temperature of coke

The additional methods of additives include the mechanical mixing method and the impregnation method. Civil clean coke is prepared by adding 1.0% Na_2CO_3 in two methods respectively. **Figure**

2 shows the effect of the Na_2CO_3 addition method on the ignition temperature of civil clean coke. It can be seen from **Figure 2** that the ignition temperature of the coke sample obtained by the mechanical mixing method is 688 K, which is 21 K higher than that obtained by the impregnation method. This is because Na_2CO_3 is loaded on the surface of coal samples through mechanical mixing, and the impregnation method can make Na_2CO_3 contact with coal particles more closely, and promote the change of carbon skeleton in the process of high-temperature carbonization of coal, which makes the ignition temperature of coke obtained by impregnation method significantly lower than that of mechanical mixing method.

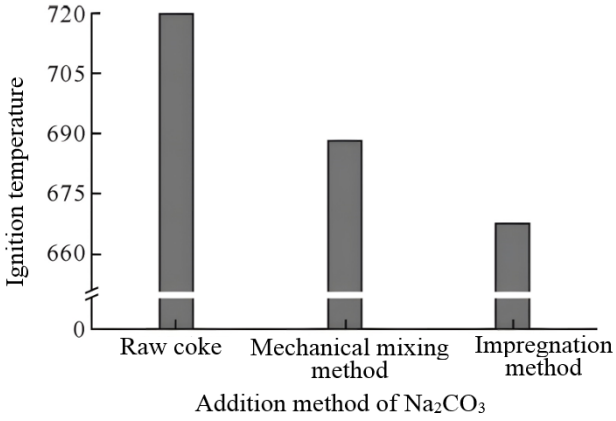

Figure 2. The effect of Na_2CO_3 Adding methods on the ignition temperature of civil clean coke.

3.2.2 Effect of Na_2CO_3 addition amount on ignition temperature of civil coke

Civil clean coke was prepared by adding 0.5%, 1.0%, 1.5%, 2.0% and 2.5% Na_2CO_3 by impregnation method. **Figure 3** shows the effect of Na_2CO_3 addition amount on the ignition temperature of civil clean coke.

It can be seen from **Figure 3** that the ignition temperature of civil clean coke decreases to varying degrees after adding Na_2CO_3 in the impregnation method; with the increase of Na_2CO_3 addition, the ignition temperature of civil clean coke decreases first and then increases; when the addition amount is 1.0%, the ignition temperature drops most significantly; when excessive Na_2CO_3 is added, part of Na covers part of the carbon surface, blocking part of the pores, and the oxygen transfer resistance increases, which hinders the combustion of coke and makes the ignition temperature rise[18].

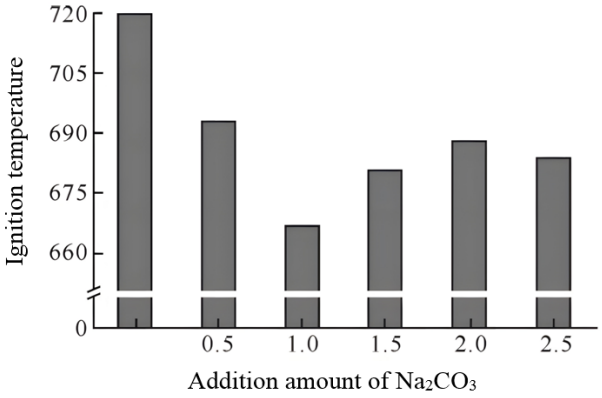

Figure 3. The effect of Na_2CO_3 addition amount on the ignition temperature of civil clean coke.

3.2.3 Effect of adding 1.0% Na_2CO_3 on coking characteristics of coal samples

When determining the volatile matter, the solid matter remaining in the crucible is called coke slag. Judging the characteristics of coke slag on the original coal sample and the coal sample obtained by adding 1.0% Na_2CO_3 by the impregnation method, the upper and lower surfaces of coke slag have silver-white metallic luster and obvious expansion, but the height is lower than 15 mm, which belongs to the seventh category of coke slag characteristics. It shows that the addition of Na_2CO_3 has no obvious effect on the coking characteristics of coal samples.

3.3 Influence of Na_2CO_3 on combustion performance of civil clean coke

3.3.1 Thermogravimetric curve analysis

Figures 4(a) and **4(b)** show the weight loss curve (TG) and weight loss differential curve (DTG) of the experimental coal when the coke and the original coke are burned by impregnation with 1.0% Na_2CO_3.

It can be seen from **Figure 4(a)** that the curves of the two coke samples basically coincide in the temperature range of 300 ~ 763 K, and the weight loss phenomenon is not obvious, because the experimental samples are obtained by high-temperature distillation, and the water and volatile content are low. Compared with the original coke, the curve of coke added with Na_2CO_3 moves to the left obviously in the temperature range of 763 ~ 1,074 K, indicating that Na promotes the combus-

tion of fixed carbon; after adding Na_2CO_3, the final temperature of coke combustion is advanced, and the percentage of combustion loss is reduced by 3.16%. This is because Na_2CO_3 promotes combustion, which makes the heat release rapidly in a shorter time, resulting in a small increase in the amount of carbon residue. At the same time, adding Na_2CO_3 increases the ash content of coke samples.

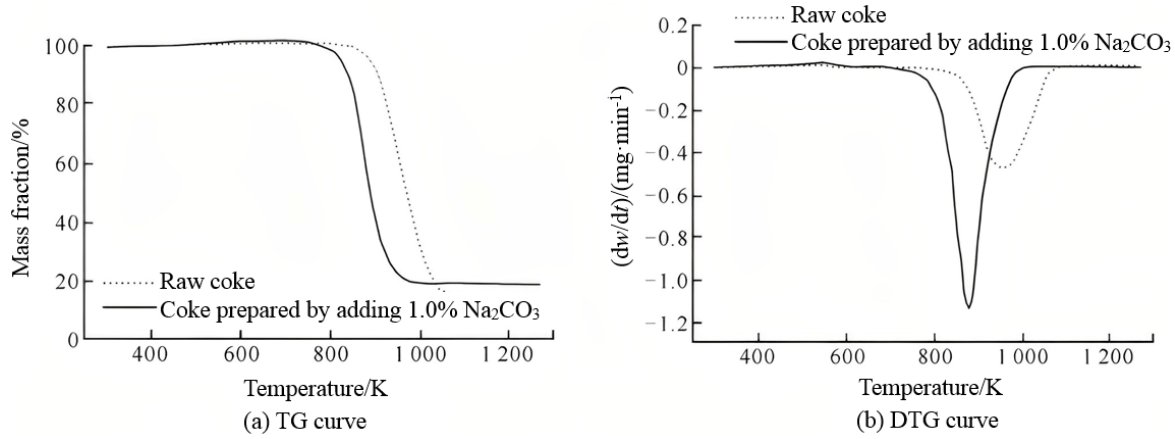

Figure 4. The TG-DTG curves of the raw coke and coke added with Na_2CO_3.

Table 2. The combustion indexes of the raw coke and coke added with Na_2CO_3

Sample name	Initial combustion temperature T_i/k	Burnout temperature T_h/k	Average combustion rate $\bar{v}$ /(mg·min^{-1})	Maximum burning rate v_{max}/(mg·min^{-1})	Comprehensive combustion index S/(× 10^{-10}·mg^{-2}·min^{-2}·K^{-3})
Raw coke	918	1,074	0.38	0.48	2.01
Coke prepared by adding 1.0% Na_2CO_3	873	998	0.75	1.13	11.14

It can be seen from **Figure 4(b)** that the DTG curve of coke made by adding Na_2CO_3 is similar to the original coke, and the ignition mode has not changed, but the curve moves to the left, the peak width narrows, and the maximum combustion rate increases significantly, indicating that adding Na_2CO_3 can significantly improve the combustion performance of coke without changing the ignition mode.

3.3.2 Comprehensive combustion index analysis

In this paper, the comprehensive combustion index s is used to describe the combustion of the sample[19].

$$S=\frac{(dw/dt)_{max}(dw/dt)_{mean}}{T_i^2 T_h} \quad (1)$$

Where: $(dw/dt)_{max}$ is the maximum combustion rate, mg/min; $(dw/dt)_{mean}$ is the average combustion rate, mg/min; T_i is the initial combustion temperature, K; T_h is the burnout temperature, K. Here T_i is determined by TG-DTG method[20].

Table 2 shows the combustion indexes of raw coke and Na_2CO_3 added coke obtained from TG curve. It can be seen from **Table 2** that after adding 1.0% Na_2CO_3, the coke combustion is advanced, the initial combustion temperature and burnout temperature are reduced, the combustion time is short, and the combustion is more concentrated; the average combustion rate, the maximum combustion rate and the comprehensive combustion index increased. It can be seen that the addition of Na_2CO_3 has a significant impact on the combustion characteristics of coke, which is mainly due to the increase of combustion rate and the decrease of initial combustion temperature and burnout temperature.

3.4 Improvement mechanism of Na_2CO_3 on combustion performance of civil clean coke

3.4.1 Pore structure analysis

Figure 5 shows the N_2 adsorption and desorption isotherm curve of raw coke and coke samples prepared by adding 1.0% Na_2CO_3. It can be seen from **Figure 5** that the adsorption capacity of coke prepared by adding Na_2CO_3 at the maximum rela-

tive pressure is 60 cm^3/g, which is much larger than 15 cm^3/g of the original coke; the N_2 isothermal adsorption and desorption curves of the two samples belong to the type IV isothermal curve in the classification of IUPAC isotherms. The coke made by adding Na_2CO_3 has H_3 hysteresis ring in the range of relative pressure p/p_0 = 0.5 ~ 1.0, and the original coke has H3 hysteresis ring in the range of p/p_0 = 0.7 ~ 1.0. It is considered that both of them have slit holes formed by the accumulation of sheet particles, and the pore size distribution of coke made by adding Na_2CO_3 is more extensive; the curve of both rises in the high-pressure section (p/p_0 = 0.9 ~ 1.0), and the increase of adsorption capacity indicates the existence of macropores with particle accumulation[20].

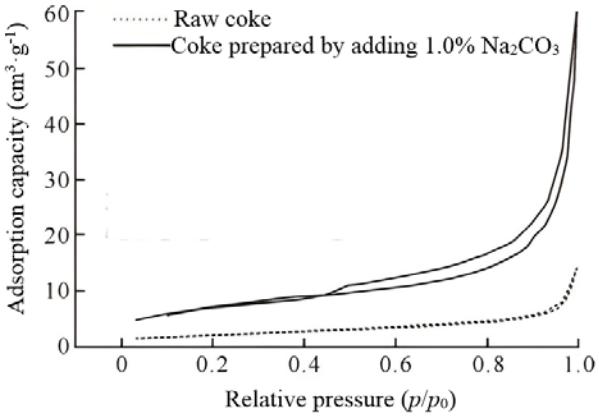

Figure 5. The N_2 adsorption-desorption isotherm of the raw coke and coke added 1.0% Na_2CO_3.

Table 3 shows the pore structure parameters of raw coke and coke samples prepared by adding 1.0% Na_2CO_3.

Table 3. The pore structure parameters of the raw coke and coke added 1% Na_2CO_3

Sample name	Specific surface area/($m^2 \cdot g^{-1}$)	Pore volume/($cm^3 \cdot g^{-1}$)	Aperture /nm
Raw coke	8.94	0.017	8.66
Coke prepared by adding 1.0% Na_2CO_3	21.30	0.079	11.03

It can be seen from **Table 3** that after adding Na_2CO_3, the pore volume and pore diameter of coke are significantly changed. Compared with the original coke, the specific surface area is 21.30 m^2/g, which is increased by 1.4 times; the pore volume is 0.079 cm^3/g, which is increased by 3.6 times; the pore size is 11.03 nm, which increases by 2.4 nm. It further shows that the pore structure of the coke sample made of Na_2CO_3 is richer than that of the original coke, which provides sufficient gas-solid contact surface and gas diffusion channel for the combustion of coke, promotes oxygen transfer, accelerates the reaction rate of coke, and improves the combustion performance.

3.4.2 Thermokinetic analysis

Generally, the gas-solid reaction conforms to the following kinetic equation[21,22]:

$$\frac{d\alpha}{dt}=Kf(\alpha)=Ae^{-E/(RT)}f(\alpha) \quad (2)$$

Where, α is the reaction conversion, t is the reaction time, K is the reaction rate constant, $f(\alpha)$ is a function related to solid unburned reactants and reaction rate, A is the frequency factor, E is the activation energy of the reaction, R is the gas constant of 8.314 J/(mol·K), and T is the reaction temperature.

Through thermogravimetric curve, reaction conversion α is

$$\alpha=\frac{(m_0-m_t)}{(m_0-m_w)} \quad (3)$$

Heating rate β is

$$\beta=\frac{dT}{dt} \quad (4)$$

Arrange formula (2) ~ (4) and arrange the Coats-Redfern integral to obtain the approximate solution[23]:

When n = 1

$$\ln\left[\frac{-\ln(1-\alpha)}{T^2}\right]=\ln\left[\frac{AR}{\beta E}\left(1-\frac{2RT}{E}\right)\right]-\frac{E}{RT} \quad (5)$$

When n ≠ 1

$$\ln\left[\frac{1-(1-\alpha)^{1-n}}{T^2(1-n)}\right]=\ln\left[\frac{AR}{\beta E}\left(1-\frac{2RT}{E}\right)\right]-\frac{E}{RT} \quad (6)$$

Take points $\left(ln\left[\frac{AR}{\beta E}\left(1-\frac{2RT}{E}\right)\right],\frac{1}{T}\right)$ from the TG curve and regress the curve with the least square method to obtain the linear equation: $y = ax + b$.

According to the characteristics of thermogravimetric curve, the low temperature zone and high temperature zone are treated, respectively, with the maximum combustion rate point as the boundary. The fitting equation and correlation coefficient of reaction order n are 0, 1/2, 2/3, 1 and 2, respectively (**Table 4**). The activation energy E of the reaction is obtained from the fitting line, and the frequency factor A is obtained from the intercept. The calculated kinetic parameters of the coke sample are shown in **Table 5**.

It can be seen from **Table 5** that in the low temperature zone, the apparent activation energy of coke before and after Na_2CO_3 addition is 454.28 kJ/mol and 306.85 kJ/mol, respectively. The addition of Na_2CO_3 reduces the apparent activation energy in the low temperature zone, and Na_2CO_3 can improve the reaction rate in the low temperature zone to a certain extent; in the high temperature zone, the apparent activation energy of coke before and after adding Na_2CO_3 is 557.36 kJ/mol and 95.36 kJ/mol, respectively. The apparent activation energy of coke prepared by adding Na_2CO_3 is much lower than that of original coke. The reaction rate in the high temperature combustion zone is significantly increased and the combustion time is short, which is consistent with the previous analysis. It can be seen that the addition of Na_2CO_3 reduces the apparent activation energy of the system in the whole combustion reaction process, improves the reaction rate, and makes the TG and DTG curves significantly move towards the direction of low temperature.

Table 4. The fitting equations and related coefficients with different reaction orders

Sample name	Reaction order	Low temperature zone		High temperature zone	
		Fitting equation	Correlation coefficient R^2	Fitting equation	Correlation coefficient R2
Raw coke	0	y = –40 045x + 36.441	0.9775	y = –5 714.3x–0.1375	0.9149
	1/2	y = –42 621x + 39.586	0.9830	y = –8 401.6x + 3.2123	0.9395
	2/3	y = –43 628x + 40.814	0.9849	y = –10 546x + 5.6792	0.9552
	1	y = –45 892x + 43.568	0.9882	y = –18 175x + 14.178	0.9822
	2	y = –54 640x + 54.187	0.9910	y = –67 039x + 67.41	0.9981
Coke prepared by adding 1.0% Na_2CO_3	0	y = –31 170x + 18.291	0.9067	y = –2 911.8x–11.137	0.8045
	1/2	y = –32 464x + 19.781	0.9199	y = –8 444.1x–5.2798	0.9825
	2/3	y = –32 916x + 20.301	0.9241	y = –11 470x–2.1343	0.9975
	1	y = –33 851x + 21.378	0.9322	y = –20 146x + 6.7932	0.9863
	2	y = –36 908x + 24.892	0.9530	y = –66 694x + 54.207	0.8928

Table 5. The kinetic parameters

Sample name	Temperate zone	Reaction order	Correlation coefficient R^2	Frequency factor A/s^{-1}	Activation energy E/(kJ·mol^{-1})
Raw coke	Low-temperature zone	2	0.9910	3.53×10^{16}	454.28
	High-temperature zone	2	0.9981	7.93×10^{4}	557.36
Coke prepared by adding 1.0% Na_2CO_3	Low-temperature zone	2	0.9530	2.38×10^{16}	306.85
	High-temperature zone	2/3	0.9975	1.35×10^{4}	95.36

4. Conclusion

(1) Adding 1.0% Na_2CO_3 by impregnation method can significantly improve the combustion characteristics of coke, significantly shift the TG and DTG curves to the left, and significantly increase the comprehensive combustion index.

(2) The coke with 1.0% Na_2CO_3 has a richer pore structure than the original coke, providing sufficient gas-solid contact surface and gas diffusion channel for coke combustion, and promoting oxygen transfer.

(3) After adding 1.0% Na_2CO_3, the apparent activation energy of the whole combustion system decreases, the apparent activation energy in the

low-temperature zone decreases from 454.28 kJ/mol to 306.85 kJ/mol, and the apparent activation energy in the high-temperature zone decreases from 557.36 kJ/mol to 95.36 kJ/mol. The reaction rate increases, which significantly improves the combustion performance of coke.

Acknowledgement

This work is supported by Air Heavy Pollution Cause and Control Project (DQGG-0511); Key Laboratory of Coal Science and Technology, Taiyuan University of Technology (mkx201805); Independent Innovation Project of Shanxi Transition Comprehensive Reform Demonstration Zone (2016CXJJ021); National Natural Science Foundation of China (21878210).

Conflict of interest

The authors declare that they have no conflict of interest.

References

1. Zhang J. How can the countryside scatter coal be cleaner? China Environment News, 2016 Mar 8. Available from: http://49.5.6.212/html/2016-03/08/content_40905.htm.
2. Lin Y, Zhang W, Lin Y, *et al*. Control strategy of cascading failures considering the health degree of coal-fired units and load transfer. Power System Protection and Control 2019; 47(17): 101–108.
3. Ministry of Environmental Protection. Technical guidelines for comprehensive management of civil coal combustion pollution (trail): No.66. 2016. p. 3–5.
4. Su J, Sun J, Liu Y, *et al*. Research on AVC system optimization of power plant based on human-simulated intelligent control. Power System Protection and Control 2018; 46(2): 157–162.
5. Chen P, Du W, Yang S, *et al*. Research progress on coal-based clean fuels replacing civil scattered burning coal. Modern Chemical Industry 2017; 37(6): 48–52.
6. Zhao D, Gao Z, Liu W. Low-carbon energy-saving power generation dispatching optimized by carbon capture thermal power and cascade hydropower. Power System Protection and Control 2019; 47(15): 148–155.
7. Zheng W. Environment-friendly coke production for domestic use by utilizing surplus coke making capacity. Fuel & Chemical Process 2016; 47(3): 1–3.
8. He X, Chen C, Wang C, *et al*. Research on the influence of combustion additive to coal combustion property. Fuel & Chemical Process 2014; 45(3): 8–10.
9. Yang Y, Deng N, Zhang S, *et al*. Research situation of combustion-supporting additives during coal combustion. Journal of Chongqing University of Science and Technology (Natural Science Edition) 2009; 11(3): 70–72.
10. Yang K, Xu D, Xie H, *et al*. Combined heat and power dispatching model based on gas-steam combined cycle unit. Power System Protection and Control 2019; 47(8): 137–144.
11. Zou C, Zhao J. Investigation of iron-containing powder on coal combustion behavior. Journal of the Energy Institute 2017; 90: 797–805.
12. Gong X, Guo Z, Wang Z. Reactivity of pulverized coals during combustion catalyzed by CeO_2 and Fe_2O_3. Combustion & Flame 2010; 157(2): 351–356.
13. Liu R, Zhao B, Huang X, *et al*. Optimization of coal combustion promoter for blast furnace injection. Coal Processing & Comprehensive utilization 2009; 27(4): 42–45.
14. Chen Y, Li H. Effect of additive on combustion characteristic and ash melting of inferior coal. Coal Conversion 2015; 38(1): 69–74.
15. Gong Z, Wu W, Zhao Z, *et al*. Combination of catalytic combustion and catalytic denitration on semi coke with Fe_2O_3 and CeO_2. Catalysis Today 2018; 318: 59–65.
16. Zou C, Zhao J, Li X, *et al*. Effects of catalysts on combustion reactivity of anthracite and coal char with low combustibility at low/high heating rate. Journal of Thermal Analysis and Calorimetry 2016; 126(3): 1469–1480.
17. Determination of Ignition Temperature of Coal. Chinese patent. GB/T 18511–2001. Beijing: Standards Press of China. 2017. p. 1–12.
18. Li M, Jiao X. Effect of metallic compounds on inferior anthracite combustion characteristics. Coal Conversion 2008; 31(4): 94–96.
19. Wei L, Qi D, Li R, *et al*. Effects of alkali metal on combustion of pulverized coal and kinetic analysis. Journal of China Coal Society 2010; 35(10): 1707–1711.
20. Nie Q, Sun S, Li Z, *et al*. Thermogravimetric analysis on the combustion characteristics of brown coal blend. Journal of Combustion Science and Technology 2001; 7(1): 72–76.
21. Zhang S, Tang S, Zhang J, *et al*. Pore structure characteristics of China sapropelic coal and their development influence factors. Journal of Natural Gas Science & Engineering 2018; 53: 370–384.
22. Hu R, Shi Q. Thermal analysis kinetics. Beijing: Science Press; 2001. p. 47–49.
23. Jiang X, Yang H, Liu H, *et al*. Analysis of the effect of coal powder Granularity of combustion characteristics by thermogravimetry. Proceedings of the CSEE 2002; 22(12): 142–145.

EnPress Publisher, LLC

Add: 9650 Telstar Avenue, Unit A, Suit 121, El Monte, CA 91731

Tel: +1 (949) 299 0192

Email: contact@enpress-publisher.com

Web: https://enpress-publisher.com